Design and development of novel selective LXR/PPAR dual agonists for Alzheimer's Disease.

by

Ian Steinke

A dissertation submitted to the Graduate Faculty of
Auburn University
in partial fulfillment of the
requirements for the Degree of
Doctor of Philosophy Pharmaceutical Sciences

Auburn, Alabama
August 3, 2024

Approved by

Dr. Rajesh Amin, Chair, Professor of Drug Discovery and Development
Dr. Forrest Smith, Co-chair, Professor and Director of Drug Discovery and Development
Dr. Randall Clark, Gilliland Professor of Drug Discovery and Development
Dr. Jack DeRuiter, Alumni Professor of Drug Discovery and Development
Dr. Robert Arnold, Professor and Director of Drug Discovery and Development
Dr. Satyanarayana Pondugula, Professor of Veterinary Anatomy

Abstract

Alzheimer's disease (AD) is a progressive neurodegenerative disorder characterized by the accumulation of insoluble protein aggregates, i.e., amyloid beta and Tau. Genetic predispositions in amyloid beta (Aβ) and Tau protein processing correlate strongly with disease prevalence. However, pathological hallmarks of AD can exist independently of each other. Additionally, patients with a genetic predisposition may never develop AD, indicating that epigenetic influences and lifestyle choices significantly impact disease initiation and progression.

Mutations in Apolipoprotein E (APOE) constitute the single most significant genetic risk factor for developing AD—the most commonly occurring mutations for APOE result in three different phenotypes: APOE2, APOE3, and APOE4. APOE2 and APOE3 are frequently referred to as neutral alleles, with the former being protective in certain studies. It is the APOE4 allele that poses the most significant risk for AD development, as cholesterol transport is most dramatically altered in these patients, resulting in an increased rate of blood-brain barrier (BBB) degradation and neurovascular dysfunction.

APOE transports lipids in the form of protein complexes that vary in size, density, and function, i.e., HDL, LDL, VLDL, etc. APOE is most abundantly expressed within the brain by astrocytes, a non-neuronal cell type responsible for many regulatory functions, including maintenance of the BBB, formation of myelin, regulation of nutrients, and removal of harmful metabolites, e.g., Aβ and Tau. Current therapeutic applications that modulate APOE target patients with atherosclerotic plaques and promote the removal of lipids from the peripheral tissues, transporting them back to the liver for subsequent elimination. In so doing, HDL ("healthy" cholesterol) is increased, and LDL ("bad" cholesterol) is lowered in a process known as reverse cholesterol transport (RCT).

In the paradigm of RCT-mediated therapeutic benefit, Peroxisome-proliferator-activated receptors (PPARs) and liver-X receptors (LXRs) are enticing targets, as they can directly modulate APOE regulation to improve associated deficits in patients with AD. PPAR/LXRs transcriptionally regulate various genes related to energy regulation, lipid metabolism, and cholesterol clearance through RCT mechanisms. While PPAR and LXR-specific agonists have shown promise in different transgenic animal models with atherosclerosis and AD, they perform poorly in human clinical trials and have failed to achieve FDA approval due to systemic toxicities such as steatosis, neutropenia, edema, and cardiotoxicity. Complicating this issue is the difficulty of attaining therapeutic specificity amongst PPAR/LXR isoform variability and function to prevent undesirable off-target activity in healthy tissue types.

Therefore, our computational design for novel PPAR/LXR compounds has centered around profiling selective ligand interactions across all isoforms of these receptors to gather surface activity relationships and mechanical details that identify novel ligands with improved therapeutic efficacy.

Acknowledgments

I want to thank my coadvisors Dr. Rajesh Amin and Dr. Forrest Smith for providing guidance and support to thrive in medicinal chemistry and pharmacology over the last five years. I chose this route because I was determined to learn how these fields work together to accomplish successful drug discovery and development. I am grateful for the resources and guidance provided to me, which has allowed me the freedom and knowledge to pursue all aspects of pharmaceutical science as I continue to develop as an independent researcher.

I would also like to thank my committee members, Dr. Randall Clark, Dr. Jack Deruiter, Dr. Robert Arnold, and Dr. Satyanarayana Pondugula, for supporting my ongoing research efforts and helping me stay focused on the primary goal of my dissertation. Additionally, I would like to thank my outside reader, Dr. Kristine Griffett, for providing me with valuable insights for my ongoing research efforts.

Next, I would like to thank the Department of Drug Discovery and Development for their assistance and the opportunity to be a graduate teaching assistant over the last five years. Learning and teaching are my two greatest passions (aside from my family, of course), and having the opportunity to be in an academic environment where my ideas can be developed and shared has been a fulfilling experience.

I want to thank the American Foundation for Pharmaceutical Education (AFPE) for finding my research project deserving of the Pre-Doctoral Fellowship in Pharmaceutical Science and stipend support as I completed my dissertation work. I would also like to thank the National Institute of Health, as their support for our lab's research is a great honor.

I would like to thank my family for supporting me over the last nine years as I selfishly pursued my passion for learning. Knowing they are proud of what I have accomplished brings me

the greatest joy of all. I hope to pass on as much as I have learned to my children Brennen, Jane, and soon-to-be Giddian so that their dreams and aspirations can also be achieved.

Most importantly, I would like to thank my beautiful wife, Taylor, who inspired me to buckle down when I wanted to give up and provided me with a loving home when all seemed hopeless.

Table of Contents

List of Tables

List of Figures

List of Abbreviations

AD	Alzheimer's Disease
Aβ	Amyloid Beta
NFTs	Tau Neurofibrillary Tangles
APP	Amyloid Precursor Protein
PSEN	Presenilin
APOE	Apolipoprotein E
CNS	Central Nervous System
HDL	High-Density Lipoprotein
APOC2	Apolipoprotein-C2
LDLR	Low-Density Lipoprotein Receptor
LRP	Low-Density Lipoprotein Receptor-Related Protein
SNPs	Single Nucleotide Polymorphisms
BBB	Blood-Brain-Barrier
PPARs	Peroxisome Proliferator-Activated Receptors
NF-kB	Nuclear Factor Kappa-Light-Chain-Enhancer of Activated B Cells
BDNF	Brain-Derived Neurotrophic Factors
TZD	Thiazolidinedione
LXRs	Liver X Receptors
RAR	Retinoic Acid Receptor
DBD	DNA Binding Domain
TRs	Thyroid Hormone Receptors
VDR	Vitamin D Receptors
ABCA1	ATP-binding Cassette Transporter
CETP	Cholesteryl Ester Transfer Protein
FAS	Fatty Acid Synthase
CYP	Cytochromes P450
LPL	Lipoprotein Lipase
SREBP	Sterol Regulatory Element Binding Protein
ChREBP	Carbohydrate Regulatory Element Binding Protein
HMG-CoA	β-Hydroxy β-methylglutaryl Coenzyme A
24,25EC	24(S), 25-epoxy Cholesterol
RCT	Reverse Cholesterol Transport
LDL	Low-Density Lipoprotein
KO	Knockout
24S-HC	24(S)-hydroxycholesterol
CYP46A1	Cholesterol 24-hydroxylase
CSF	Cerebral Spinal Fluid
27-HC	27-hydroxycholesterol
CADD	Computer-aided Drug Design
SBDD	Structure-based Drug Design
LBDD	Ligand-based Drug Design
NMR	Nuclear Magnetic Resonance
Cryo-EM	Cryogenic Electron Microscopy

SAR	Structure-Activity Relationship
PDB	Protein Data Bank
AF-2	Activated Function 2
LBD	Ligand Binding Domain
AF-1	N-terminal Activation Domain
vdW	Van der Waals
$Pd(OAc)_2$	Palladium (ii) Acetate
THF	Tetrahydrafuran
TBAB	Tetrabutylammonium Bromide
$SOCl_2$	Thionyl Chloride
MeOH	Methanol
NaOH	Sodium Hydroxide
DCM	Dichloromethane
DCE	1,2-dichloroethane
$NaBH_4$	Sodium Borohydride
GFP	Green Fluorescent Protein
PPRE	PPAR-response element
DRE	PPARδ-response element
AP2	Adipocyte Protein 2
LogP	Logarithm of the partition coefficient
LogD	Logarithm of the distribution coefficient
ADME	Absorption, Distribution, Metabolism, and Excretion
PBS	Phosphate-buffered Saline
PAMPA	Parallel Artificial Membrane Permeability Assay
GI	Gastrointestinal
Papp	Apparent Permeability Rate
MDR1	Multidrug Resistance Protein 1
RXRs	Retinoid X Receptors
OD	Optical Density
DMSO	Dimethyl Sulfoxide
Cs_2CO_3	Cesium Carbonate
DMF	Dimethyl Formamide
$Pd(PPh_3)_4$	Tetrakis(triphenylphosphine)palladium (0)
NBS	N-Bromosuccinimide
AIBN	Azobisisobutyronitrile
DIBAL-H	Diisobutylaluminum Hydride
K_3PO_4	Tripotassium Phosphate
RBF	Round Bottom Flask

Chapter 1: Introduction

1.1 General Overview of Alzheimer's Disease (AD)

Alzheimer's disease (AD) is a neurodegenerative condition that progressively damages the nerve cells in the brain, affecting around thirty million people worldwide. In the United States, more than five million Americans are currently living with AD, and experts predict that this number will reach sixteen million by 2050 [1]. Despite considerable research efforts into preventing, treating, or curing the disease, effective strategies remain elusive.

In 1911, Alois Alzheimer published his conclusions concerning two inpatients admitted for senile dementia. The patients presented with cognitive symptoms resembling senile dementia but differed markedly by the premature age of onset and rate of disease progression, prompting Alzheimer's postulation on the emergence of a novel neurodegenerative disease [2]. Postmortem neuro-histological examination showed an unexpected and dramatic degeneration of cortical nerve cells, displayed by the clotting of fibrils and expansive plaques throughout the brain [3]. Interestingly, although both patients showed extensive plaques, Alzheimer only detected the presence of clotting fibrils in one of the patients. Alzheimer's groundbreaking findings quickly garnered support, leading to the subsequent naming and classification of the neurodegenerative disease we now commonly refer to as AD [4, 5].

Alzheimer's identification of "excessive diffuse patches" and "coiled fibrils" would ultimately become the pathological hallmarks that characterize AD, i.e., extracellular amyloid-beta (Aβ) plaques/fibrils and intracellular Tau neurofibrillary tangles (NFTs) [6, 7]. Accompanied by criteria-based cognitive assessments, Aβ and NFTs are still used as the primary diagnostic

determinants for AD. Ambiguously, many patients do not display concurrent pathogenic development of both biomarkers, thus highlighting the separate but interconnected roles of Aβ and NFTs in AD progression [8]. Subsequent research efforts have centered on identifying the underlying mechanisms that show causative links with AD initiation and progression.

AD is a complex and enigmatic neurological condition with several well-supported hypotheses regarding its cause. These hypotheses range from genetic factors, such as mutations in amyloid precursor protein (APP), presenilin (PSEN), and apolipoprotein E (APOE), to environmental influences, such as lifestyle choices and xenobiotic exposure [9-13]. Central to genetic predisposition and lifestyle choices is the area of research focusing on the epigenetic influences associated with AD, which explores post-translational modifications that impact gene expression and its consequences on disease progression [14, 15]. Epigenetic changes, like DNA methylation and histone modifications, can protect or predispose an individual to AD by altering gene expression patterns involved with neuronal function, inflammation, and Aβ processing. The interplay between genetic and epigenetic factors underscores the complexity of AD yet offers promising avenues for potential therapeutic intervention.

1.2 APOE Involvement in AD Progression

APOE is a class of apolipoprotein, which mediates clearance, biosynthesis, and uptake by hepatocytes and peripheral tissues, ensuring triglyceride delivery and energy storage. It crucially maintains lipid homeostasis, participates in reverse cholesterol transport (RCT), and regulates lipid transport in the central nervous system (CNS), impacting neuron survival. Additionally, APOE contributes to innate and adaptive immune responses through non-specific binding to lipophilic inflammatory components with high affinity, including Aβ, lipopolysaccharides, lipoteichoic acids, and beta-glucans, which leads to the clearance of pathogenic agents and contributes to the first-line innate immunity response [16].

APOE is primarily a component of high-density lipoprotein particles (HDL). It mediates the binding to nascent chylomicrons, an interaction that leads to the transfer of both apolipoprotein-C2 (APOC2) and APOE between the two lipoproteins. This allows the utilization of esterified fatty acids and the maturation of nascent chylomicrons, as APOC2 is a coenzyme for lipase activity. After lipid stores are distributed, APOC2 is transferred back to HDL, with APOE remaining in the chylomicron remnants to facilitate macrophage recognition and clearance [17].

APOE consists of a single polypeptide chain with distinct N-terminal and C-terminal domains connected by a flexible hinge region that allows conformational flexibility to adapt to various ligands and lipid particles [18]. The N-terminal domain harbors a receptor-binding region facilitating interactions with cell surface receptors like the low-density lipoprotein receptor (LDLR) and LDL receptor-related protein (LRP). In contrast, the C-terminal domain, characterized by amphipathic alpha-helices, mediates lipid binding and is associated with lipoprotein particle compositional stability [19, 20]. As a result, the structural dynamics of APOE

respond to changes in lipid composition that can affect lipoprotein size, density, and binding. Additionally, genetic mutations in APOE profoundly impact the efficiency of lipid transport and metabolism, influencing an individual's susceptibility to lipid-related disorders like atherosclerosis and hyperlipidemia [21, 22].

Intriguingly, single nucleotide polymorphisms (SNPs) in APOE constitute the most significant genetic risk factor for developing AD [23], where the most commonly occurring APOE SNPs result in three different isoforms: APOE2 (Cysteine 112, Cysteine 158), APOE3 (Cysteine 112, Arginine 158), and APOE4 (Arginine 112, Arginine 158) [24,25]. This Arginine to Cysteine mutation effectively reduces steric bulk and polar surface area, allowing APOE the conformational freedom to pack more tightly. Mutations at both residue positions result in a similar structural consequence with an inverse functional response, as an Arg112Cys mutation enhances lipid-binding and lipoprotein stability. At the same time, the Arg158Cys decreases binding affinity for receptors [26]. As a result, excessive dietary lipid intake is better tolerated in an isoform-dependent manner APOE2 > APOE3 > APOE4 [27].

APOE3 is the most abundantly expressed isoform, commonly called the “neutral allele,” with balanced effects on lipid metabolism. APOE2 is associated with lower circulating lipid levels and is cardioprotective, with implications of being protective for neurodegenerative diseases like AD [28]. In comparison, APOE4 is consistently associated with higher circulating lipid levels, elevated risk of cardiovascular disease, and an increased susceptibility to AD [29].

Unlike other organs, the brain is approximately fifty percent lipid. It is compartmentalized from systemic circulation, predominantly relying on de novo lipogenesis and alternate mechanisms for the clearance of lipid metabolites [30, 31]. Where astrocytes play a critical role in regulating energy homeostasis within the brain, as they comprise the blood-brain barrier (BBB), transport essential

nutrients, and regulate the clearance of neurotransmitters from the synapse of neuronal cells [32]. In neurodegeneration, oxidative stress overburdens brain energy homeostasis, impeding the effective distribution of cholesterol and cholesterol metabolites, leading to toxic lipid accumulation in resident macrophages and impaired neuronal signaling [33]. In a diseased state, these effects can become more pronounced in an APOE isoform-dependent manner, as APOE4 predisposes an individual to pathogenic Aβ processing and clearance [34-36]. Currently, patients suffering from the debilitating symptoms of AD lack a directed therapeutic that displays clinical efficacy. Direct links between metabolic dysregulation and APOE4-associated deficits are well established, with APOE4 carriers making up approximately 50% of the AD population [37]. Therefore, assessing metabolically directed therapeutics targeting APOE-associated mechanisms is critical since this would provide the most significant impact for patients likely to develop AD.

1.3 PPAR Regulation and AD Association

Peroxisome proliferator-activated receptors (PPARs) are members of the nuclear hormone receptor superfamily that are ligand-activated transcription factors [38]. Researchers discovered PPARs through scientific investigations in the 1980s and 1990s. The initial discovery of PPARs stemmed from research on a class of compounds called peroxisome proliferators, known to induce the proliferation of peroxisomes in rat liver cells [39]. This research identified the effects of the PPAR orphan receptor mediating these compounds [40]. Subsequent studies uncovered three distinct PPAR isoforms: PPARα, PPARδ, and PPARγ [41].

A breakthrough in understanding PPARs came when researchers recognized that these receptors could interact with fatty acids, identifying their physiological role in lipid metabolism and glucose homeostasis [42]. The discovery of PPAR ligands, including the PPARα agonist fenofibrate, PPARγ agonist rosiglitazone, and the PPARδ agonist GW-0742, opened new avenues for research into the treatment of metabolic disorders like dyslipidemia, type 2 diabetes, and cardiovascular disease, respectively (**Figure 1.**).

PPARs exhibit inducible isotype-specific tissue expression responding to nutrient supply and energy demand. PPARα is primarily associated with regulating fatty acid catabolism, particularly in the liver, by up-regulating Acyl-CoA Oxidase [43-45]. PPARα is a central target in the management of dyslipidemia. PPARγ, on the other hand, is predominantly found in adipose tissue and plays a crucial role in adipocyte differentiation, lipid storage, and insulin sensitivity [42, 46, 47]. PPARγ is a central target in the management of type 2 diabetes and metabolic syndrome. PPARδ exhibits a broader tissue distribution with roles in various metabolic processes, including fatty acid oxidation, glucose homeostasis, and skeletal muscle function [48-50]. PPARδ ligands have not yet

achieved FDA approval, but they are commercially available as a nutritional supplement and commonly marketed as exercise mimetics. While PPARα and PPARγ have established roles in metabolic pathways, PPARδ's functions are more versatile, contributing to overall metabolic homeostasis.

PPARs present an exciting target for regulating APOE-associated deficits in patients with AD, as they can influence distinct genetic pathways involved in anti-inflammatory signaling, enhanced catabolism of lipids, and neurogenesis. PPARδ and PPARα are more highly expressed in the brain, whereas PPARα is predominantly localized in astrocytes [51]. PPARα is particularly interesting as activation in the brain has shown to be neuroprotective, enhancing mitochondrial biogenesis and reducing inflammatory activation of microglial cells [52-54]. PPARγ has been shown to reduce Aβ plaque-induced inflammation by inhibiting inflammatory chemokine nuclear factor kappa-light-chain-enhancer of activated B cells (NF-kB) and induction of brain-derived neurotrophic factors (BDNF), critical mediators of neurogenesis and synaptic plasticity [55-58]. Lastly, PPARδ has been shown to regulate insulin signaling, improve energy regulation, and remyelination in transgenic mouse models of AD [55, 56, 59, 60].

Dietary influences, combined with genetic predisposition to metabolic disorders, constitute a major confounding factor linking APOE involvement with AD progression. This underscores the rationale for identifying the underlying biological mechanisms that can be harnessed for therapeutic interventions. Targeting PPAR receptors for therapeutic benefit offers opportunities across diverse medical conditions but poses several challenges. These include off-target effects, tissue-specific responses, and, most importantly, controlling gene transcription ‘strength’ or rate. PPARs exert pleiotropic effects on various tissues and metabolic pathways, necessitating careful consideration of their therapeutic benefits and potential adverse outcomes. Understanding nuclear

receptor biology becomes an integral component for optimizing drug design, thus allowing for the maximum therapeutic potential of nuclear receptor-targeted drugs while minimizing associated risks.

Figure 1. Representative PPAR Pharmacophore Features

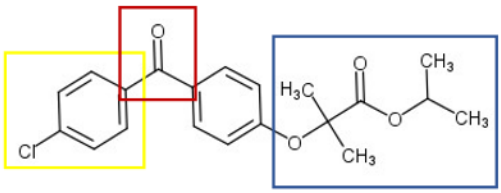

PPARα – Fenofibrate (prodrug)
EC_{50} 30 uM

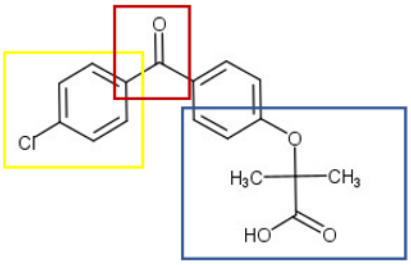

PPARα – Fenofibric acid (active drug)
EC_{50} 22.4 uM

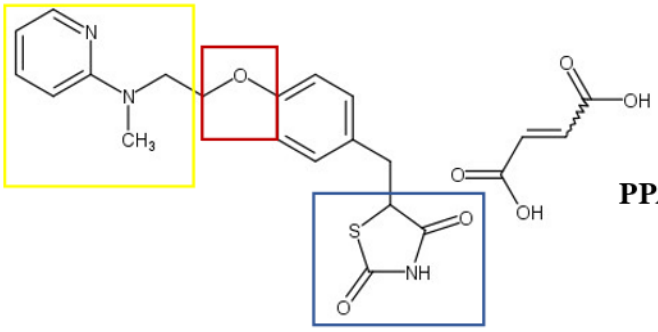

PPARγ – Rosiglitazone Maleate (Formulation)
EC_{50} 30 nM

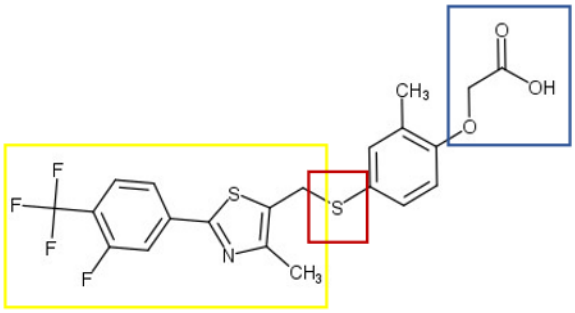

PPARδ – GW-0742
EC_{50} 1.1 nM

Legend
- Hydrophobic Tail
- Polar Anchor Point
- Active Site Moiety

The PPARα pharmacophore fenofibrate, an isopropyl ester prodrug, is the orally administered form of fenofibric acid, a 2-methylpropanoic acid isomer of butyric acid clinically approved to treat hypercholesteremia and hypertriglyceridemia. The PPARγ pharmacophore rosiglitazone, a maleate salt formulation, the ligand displays a thiazolidinedione (TZD) clinically approved to treat Type 2 diabetes by increasing insulin sensitivity in the peripheral tissues to improve glucose uptake and utilization. The PPARδ pharmacophore GW-0742, sold as a supplement, displays a phenoxy acetic acid and is marketed as an exercise mimetic to stimulate the metabolism and utilization of fatty acids stored as energy.

1.4 LXR Regulation and AD Association

Liver X Receptors (LXRs) are ligand-activated transcription factors that are closely related to PPARs, sharing approximately 40% similarity in the overall structure. LXRs were discovered in the mid-90s using a rat liver-derived cDNA library where it was shown that a subregion in the DNA binding domain (DBD) responsible for DNA binding specificity, referred to as the P box, was identical to that of Thyroid Hormone Receptors (TRs), RARs, and Vitamin D Receptors (VDR) [61]. LXRs exist in two highly conserved isoforms, LXRα and LXRβ, where LXRα is most abundantly expressed in the liver, and LXRβ is ubiquitously expressed in all tissues [62, 63].

LXRs play a pivotal role in maintaining cholesterol, fatty acid, and glucose homeostasis by upregulating transcription of ATP-binding Cassette transporter (ABCA1), APOE, Cholesteryl ester Transfer Protein (CETP), Fatty Acid Synthase (FAS), Cytochromes P450 (CYP) 7A1, Lipoprotein Lipase (LPL), Sterol Regulatory Element Binding Protein (SREBP) 1C, Carbohydrate Regulatory Element Binding Protein (ChREBP), and uniquely regulates its expression [64].

Endogenous LXR agonists arise from cholesterol enzymatic oxidation by CYP7A1, increasing oxysterol concentrations for bile acid synthesis and subsequent elimination from the liver. In addition, epoxy sterols provide a feedback mechanism to the mevalonate cholesterol synthesis pathway by inhibiting β-Hydroxy β-methylglutaryl Coenzyme A (HMG-CoA) and simultaneously binding to LXR, activating genes associated with cholesterol efflux, e.g., ABCA1, APOE [64-66]. The most potent endogenous oxysterol at physiologically relevant concentrations is the 24(S), 25-epoxy cholesterol (24,25EC), formed from the mevalonate shunt pathway and under oxidative stress (**Figure 2.**) [67].

LXRs' role in reverse cholesterol transport (RCT) pathways sparked the development of synthetic ligands for therapeutic benefit in patients with atherosclerosis. Systemically high levels of lipids in the form of Low-Density Lipoprotein (LDL) can lead to accumulation on arterial walls. Circulating macrophages are then recruited to the sight through interactions at LDLRs, influencing selective LDL uptake for subsequent removal. Continued macrophage challenge with LDL leads to excessive lipid accumulation, inducing an inflammatory phenotype called foam cells. These foam cells secrete pro-inflammatory cytokines, further recruiting macrophage aggregation at the site, eventually leading to atherosclerotic plaques. Synthetic pan-LXR agonists GW-3965 and T0901317 were able to reduce atherosclerotic plaques in LDLR and APOE knockout (KO) mice significantly; however, hepatic LXR activation also induced de novo lipogenesis and increased serum triglycerides (**Figure 2.**) [68]. While promising, the therapeutic advancement of LXR agonists has continued to be plagued by hepatic lipogenesis, a significant drawback towards clinical implementation.

Interestingly, it has been shown that LXRα and LXRβ have separate roles in regulating cholesterol. LXRα primarily acts as a sensor for dietary cholesterol, with LXRβ acting mainly in the immune response to maintain basal transcription. When challenged with a high-cholesterol diet, studies involving the murine knockout (KO) of LXRα showed a dramatic impact on hepatic cholesterol accumulation in combination with reduced bile acid excretion and composition. No noticeable changes had been observed in other tissues expressing LXRα, i.e., kidney, small intestines, spleen, and adrenal [69]. LXR pan-agonist treatment in LXRα KO mice rescued the deleterious effects observed in control mice. However, LXR target genes associated with lipogenesis SREBP1C and FAS were not upregulated, demonstrating non-overlapping roles for LXR activation [70].

Cholesterol in the brain is almost entirely derived from de novo cholesterol synthesis by astrocytes, which can then be transported via ABCA1 and APOE to neurons in the form of HDL. Since cholesterol cannot passively enter or exit the BBB, the elimination of cholesterol from the brain differs significantly from that of the liver and primarily involves its conversion into 24(S)-hydroxycholesterol (24S-HC) by the enzyme cholesterol 24-hydroxylase (CYP46A1), which is abundantly expressed in neurons [71]The 24S-HC metabolite is transported out of the CNS by HDL or passive diffusion. Once it crosses into systemic circulation, 24S-HC is transported back to the liver and converted to bile acid for removal.

The association of cerebral spinal fluid (CSF) HDL and LDL levels on AD pathology in cohort studies revealed little to no correlation with disease progression. However, AD patients did show significantly higher levels of 24S-HC in cerebral spinal fluid (CSF). Another endogenous LXR agonist, the oxysterol 27-hydroxycholesterol (27-HC), also showed a significant increase in the AD population compared as a ratio of 24S-HC/27-HC. Intriguingly, 27-HC is not produced in the brain but is derived primarily from the liver and is neurotoxic at increasing concentrations [72, 73]. This finding presents some confounding results, as the BBB should prevent the uptake of oxysterols from circulation and consequently prevent the accumulation of 27-HC. In the context of aging and metabolic-related disorders, this result could have a much more significant impact as the BBB begins to degrade, leading to increased susceptibility to endogenous metabolites and xenobiotics that can exert their effects on LXRs (**Figure 2.**).

As the LXRs are critical in regulating cholesterol and lipid metabolism, it remains to be seen how selective modulation of these receptors influences lipidomic profiles in AD. Other cholesterol-modulating drugs have shown only modest improvements in AD symptoms and fail to prevent disease progression, such as the Statin HMG-CoA inhibitor class of drugs.

Figure 2. Representative LXR Endogenous and Synthetic Agonists

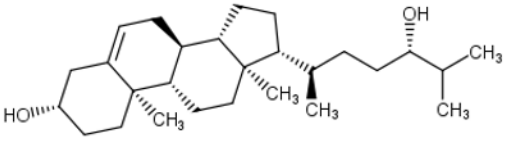

24(S)-Hydroxy Cholesterol
LXRα EC50: 4 uM
LXRβ EC50: 3 uM

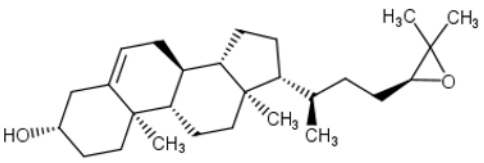

24(S),25-epoxy Cholesterol
LXRα EC50: na
LXRβ EC50: na

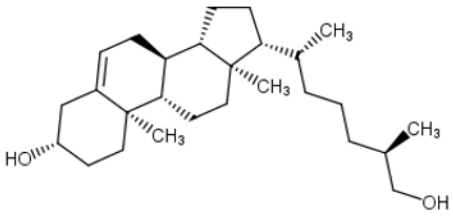

25(S)-27-hydroxy Cholesterol
LXRα EC50: 85 nM
LXRβ EC50: 71 nM

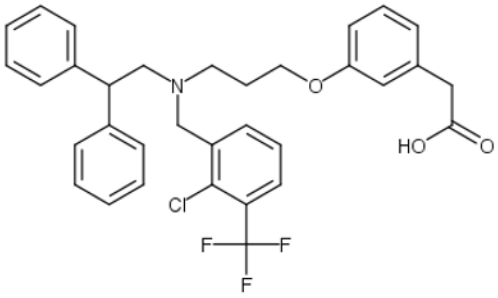

GW3965
LXRα EC50: 190 nM
LXRβ EC50: 30 nM

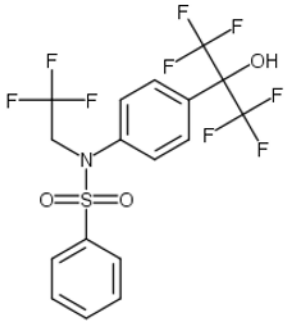

T0901317
LXRα EC50: 50 nM
LXRβ EC50: 50 nM

Oxysterols are the oxidized metabolites of cholesterol, which upregulate cholesterol influx and efflux mechanisms and are endogenous ligands for the LXR nuclear receptors. The cholesterol molecule contains multiple chiral centers. Oxidation can occur at various positions, forming oxysterols with different stereochemical configurations and affinity for each LXR isoform. Synthetic LXR ligands such as GW3965 and T0901317 display key pharmacophore elements encompassing hydrophobic moieties that are complementary to the LXR receptor's LBD alongside hydrogen bond acceptors and hydroxyl groups. Complementary hydrogen bond donor groups enhance binding affinity by forming hydrogen bonds with the receptor that support conformational bias and substrate selectivity. Ligands containing carboxylic acid moieties and linker regions, as seen in GW3965, display a six-fold selectivity for the more hydrophobic and elongated LXRβ LBD. The smaller T0901317 ligand displays comparable activation at each LXR isoform as the 1,1,1,3,3,3-hexafluoropropan-2-ol moiety interacts preferentially with the conserved AF-2 domain.

1.5 Computer-aided Drug Design (CADD)

A drug can be defined as a substance intended for use in the diagnosis, cure, mitigation, treatment, or prevention of disease as described by the FDA [74]. In 2019, the pharmaceutical industry invested $83 billion in the research and development of novel drugs, where many of the new drugs being produced are listed as "specialty drugs" or drugs that generally treat chronic, complex, or rare conditions [75]. Estimated costs for a drug to reach the market range from $1-2 billion [76]. Approaches that utilize computer-aided drug design (CADD) offer significant benefits in the successful early-stage development of drugs from both an economic and feasibility standpoint [77]. Approaches to CADD can vary based on the availability of experimental data and can be subdivided into two primary categories: structure-based drug design (SBDD) and ligand-based drug design (LBDD).

SBDD primarily focuses on the three-dimensional structure of the biological target, such as a protein or enzyme. It involves analyzing the detailed atomic and molecular interactions between the target and potential drug molecules. SBDD often relies on experimental techniques like X-ray crystallography, nuclear magnetic resonance (NMR), and Cryogenic Electron Microscopy (cryo-EM) to determine the high-resolution structure of protein complexes. SBDD provides a precise understanding of binding interactions and mechanistic details, enabling the design of drugs with high specificity for the target protein and minimizing off-target effects. The availability of high-quality structures limits SBDD, and obtaining such structures can be challenging.

LBDD focuses on the characteristics and properties of known active ligands (molecules that bind to the target) rather than the target itself. It involves analyzing the structure-activity

relationship (SAR) of ligands. LBDD often employs computational methods to analyze and model the relationships between the chemical structure of ligands and their biological activities. LBDD can be applied without detailed target structures, relying on available experimental data on ligand activities. It is more applicable when structural information about the target is limited or unavailable. LBDD may lack the precision of SBDD, as it relies on statistical correlations between ligand structures and activities. It may not be as effective for diverse targets compared to SBDD.

Both approaches have their strengths and limitations, and their effectiveness often depends on the specific characteristics of the target and available data. Integrating both SBDD and LBDD can provide a comprehensive strategy for drug discovery. The availability of structures and ligands for PPARs and LXRs is crucial in advancing CADD strategies targeting these nuclear receptors. The Protein Data Bank (PDB) contains crystallographic and NMR structures for various PPAR and LXR isoforms. These structures offer valuable insights into the three-dimensional conformations of the receptors and their binding sites, facilitating the identification of potential ligand interactions. Additionally, a diverse collection of known ligands with varying affinities for PPARs and LXRs provides a rich dataset for LBDD approaches.

The combination of structural information and ligand datasets enables computational methods such as molecular docking and dynamics simulations to explore and predict novel compounds' binding affinity and selectivity. Researchers in the field of CADD can leverage these resources to design and optimize PPAR and LXR modulators with therapeutic potential.

1.6 Previous Work

Our lab's previous work with the PPARδ/γ selective agonist **AU-9,** shown in **Figure 3.**, effectively improved cognition in a mouse AD model while avoiding PPAR toxicities, primarily attributed to the attenuated activation of PPARγ. While AU-9 displayed PPARδ activation, its effects were relatively unbalanced, with no activation of PPARα, a critical mediator of lipid regulation in astrocytes. Additionally, AU-9 displayed poor physiochemical properties and a molecular mass >500 g/mol, essential ADME parameters that could hinder effective biodistribution to the brain (**Table 1.**).

The structure of AU-9 offered similarities with the existing PPAR pharmacophore scaffolds, consisting of a lipophilic carboxylic acid attached to a weakly polar hydrophobic tail connected through a polar linker group. Compound AU-9's structure differed from the PPAR pharmacophore scaffolds with the inclusions of a sterically bulky para-benzoic acid active site moiety and a branched polar amine linker. In silico modeling identified the para-benzoic acid as the primary determinant of the decrease in PPARγ activity, and the weakly polar hydrophobic tail containing a 3,5-bis(trifluoromethyl) phenyl favored PPARδ selective activation. In silico predicted binding poses generated from AU-9 highlighted a conformational requirement to access the PPARγ LBD AF-2 [78, 79]. Various binding motifs were explored through manual iterative ligand design using predictive ADME filters to generate compound **7** (AU-403), a novel selective PPARα/δ agonist.

Figure 3. Evolution of AU-9 PPARδ Selective Agonist to AU-403 PPARα/δ Selective Agonist

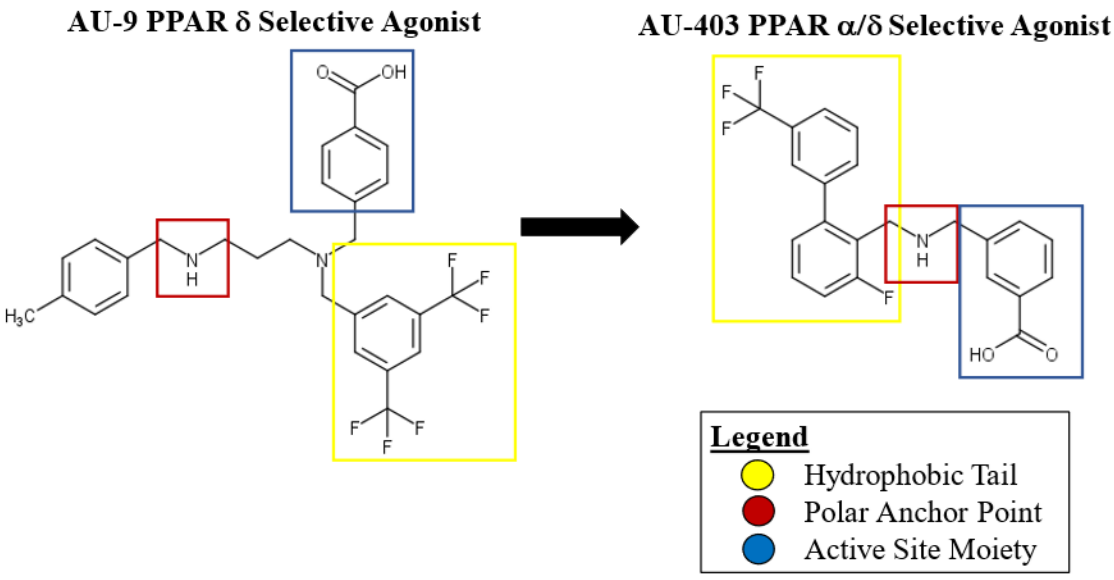

The ligand AU-403's weakly polar surface area of the halogenated aromatics enhances predictive docking scores through complementary aromatic interactions with the hydrophobic surface area of the PPARδ LBD, similar to observed predictive interactions of AU-9 and GW-0742. The dibenzylamine polar anchor point displayed by AU-403 can donate a hydrogen bond that distinguishes an apparent conformational bias for PPARα and PPARδ selective activation. The sterically hindered meta-benzoic acid displayed by AU-403 forms unfavorable interactions with the PPARγ LBD AF-2, similar to observed predictive interactions of AU-9.

Table 1. QikProp ADME Predictive Comparison - Property Descriptors, Descriptions, and Recommended Values Range.

Structure	mol_MW	QPlogPo/w	QPPCaco	QPlogBB	QPPMDCK	Human Oral Absorption
AU9	538.532	4.748	11.64	-0.149	104.557	1
AU-403	403.375	2.748	74.741	0.08	198.16	3

The AU-403 structural design focused on maintaining predictive ADME physiochemical properties conducive to oral drug delivery to the CNS. In contrast, the AU-9 chemical structure displayed a predictive ADME physiochemical profile non-conducive to oral drug delivery to the CNS. QikProp ADME predictive descriptors are described below.

Mol_MW: Molecular weight of the molecule, 130.0 – 725.0.
QPlogPo/w: Predicted octanol/water partition coefficient, -2.0 – 6.5.
QPPCaco: Predicted apparent Caco-2 permeability in nm/sec. Predictions are for non-active transport, <25 poor and >500 great.
QPlogBB: Predicted brain/blood partition coefficient. QikProp predictions are for non-active transport, -3.0 – 1.2.
QPPMDCK: Predicted apparent MDCK cell permeability in nm/sec. QikProp predictions are for non-active transport, <25 poor and >500 great.
Human Oral Absorption: Predicted qualitative human oral absorption. The assessment uses a knowledge-based set of rules, including checking for suitable values of %Human Oral Absorption, number of metabolites, number of rotatable bonds, logP, solubility, and cell permeability, 1, 2, or 3 for low, medium, or high.

Rationale and Research Objectives

Currently, the only FDA-approved treatments for Alzheimer's Disease (AD) that can change disease progression are Lecanemab and Aducanumab, which are both monoclonal antibodies targeting Aβ fibrils and Aβ plaques. However, these drugs have shown tenuous clinical efficacy with patients experiencing severe adverse side effects, including brain microhemorrhages, brain swelling, and accelerated brain atrophy. Furthermore, these drugs are administered via IV infusion and thus indirectly target Aβ in the brain. The remaining FDA-approved drugs for AD only treat cognitive and non-cognitive symptoms, i.e., memory/thinking and behavioral/psychological symptoms, respectively.

AD-associated neurodegenerative signs and symptoms often develop after years of significant disease progression, which leaves a large knowledge gap in the mechanisms that go awry. However, APOE4 genetic susceptibility coincides strongly with AD comorbidities such as dyslipidemia, type 2 diabetes, and cardiovascular disease, thereby identifying mechanisms for therapeutic intervention that can prevent disease progression. For this reason, it is hypothesized that developing novel therapeutics targeting PPAR/LXR will promote APOE function globally and delay or avoid AD by promoting clearance of pathogenic Aβ and accumulated lipids.

PPAR and LXR selective agonists have failed to reach clinical significance for AD due to off-target systemic toxicities yet show promising benefits in vitro and in vivo. Therefore, computer-aided drug design (CADD) was employed to evaluate a comprehensive library of PPAR and LXR selective agonists with their respective nuclear receptors, modeling specific amino acid interactions with known active ligands to build contact profiles for predictive drug design. In this manner, isoform selectivity is controlled, and undesirable effects may be avoided.

Chapter 2: Results and Discussion

2.1 PPAR and LXR Structural Organization

Understanding how ligands interact with the highly conserved activated function 2 (AF-2) is vital to determining the activity of PPAR, LXR, and other nuclear receptors (NRs) (**Figure 4**.). Testing the activity of ligands for NRs can be challenging due to several factors. NRs have diverse ligand binding domains (LBD) that accommodate a wide range of ligands. This makes assessing their binding affinity, specificity, and functional effects difficult. Moreover, several factors influence their activity, such as the cellular microenvironment, co-regulator proteins, and post-translational modifications, making experimental interpretation complex. Ligand binding can trigger downstream signaling events and changes in gene expression, which may not always directly correlate with the ligand concentration. Therefore, multiple endpoint measurements are necessary. The structural diversity of ligands and the requirement for reliable assays further complicate ligand screening.

CADD significantly enhances experimental validation in drug discovery by guiding ligand design, mechanism elucidation, optimization of experimental conditions, data interpretation, and lead optimization. Techniques such as ligand docking, molecular dynamics, and structural interaction fingerprints aid in rationalizing ligands with desirable properties, prioritizing potential drug targets, and predicting protein-ligand interactions and dynamic processes. Furthermore, molecular modeling facilitates lead optimization through iterative refinement of candidate compounds based on computational predictions and experimental feedback, ultimately accelerating the drug discovery process.

While the AF-2 is highly conserved among nuclear hormone receptors, amino acid residues within the LBD vary, allowing receptor-specific interactions with coregulator proteins and ligand modulation of transcriptional activity (**Figure 4.**). Therefore, it is critical to understand the rate-limiting factors at each receptor site to establish pharmacophore features that correlate to experimental EC_{50} values.

Figure 4. Structural Organization of Nuclear Receptors

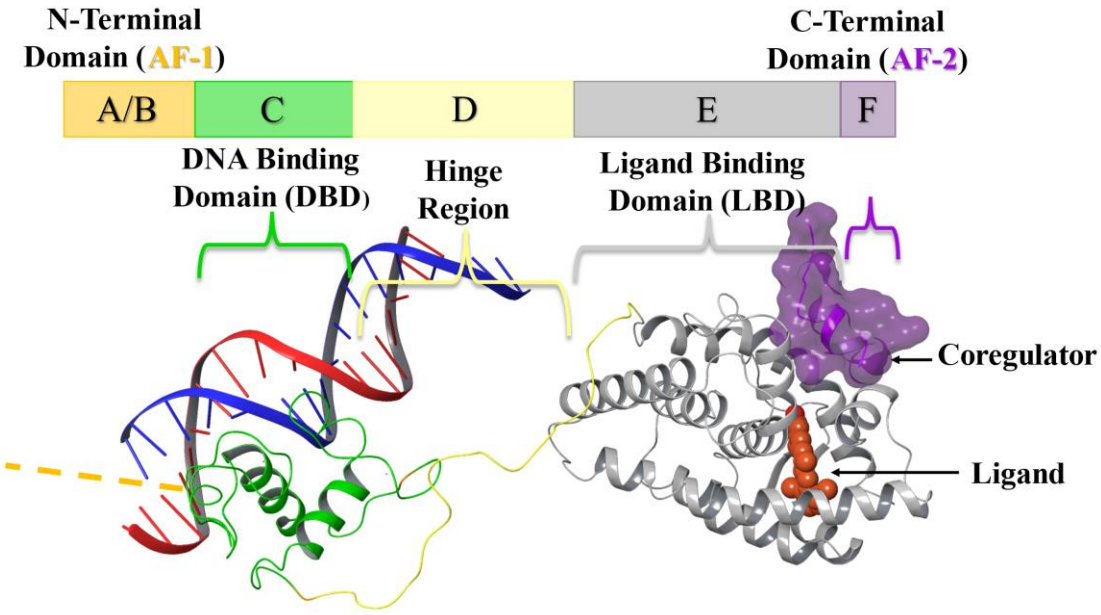

Nuclear receptors (NR) have a modular structure consisting of several functional domains, including the N-terminal activation domain (AF-1), DNA-binding domain (DBD), hinge region, ligand-binding domain (LBD), and the C-terminal activation domain (AF-2). The DBD is highly conserved among nuclear receptors and is responsible for sequence-specific DNA binding. It contains two zinc finger motifs that interact with obligate DNA sequences known as response elements (RE) located in the regulatory regions of the NR target genes, e.g., peroxisome proliferator (PPRE) and Liver-X (LXRE). In the unbound state, the apoprotein is complexed with a corepressor protein that dissociates upon ligand binding, conformationally reorganizing the LBD/AF-2 to recruit a coactivator protein for subsequent gene transcription.

2.2.1 In Silico PPAR Structure Activity Relationship (SAR): Receptor SiteMap Analysis

Understanding the primary binding site on a receptor is essential for creating effective ligands in drug design. SiteMap is a tool used in drug design that identifies potential binding sites on protein surfaces through grid-based searches. It generates detailed contour maps that highlight hydrophobic and hydrophilic regions. Determining nearby sites that could be useful for allosteric binding can also be crucial, e.g., coregulator proteins. However, in some cases, the location of a binding site for protein-ligand or protein-protein interactions has yet to be discovered despite the available protein structures. Computational studies suggest potential protein binding sites and predict receptor site physiochemical properties by evaluating complementary receptor site ligand interactions. SiteMap's SiteScore and other properties such as volume, hydrophobicity, hydrophilicity, balance, and Dscore can assist in evaluating and refining ligand-receptor interactions. This tool outperforms traditional surface coloring methods by providing comprehensive insights into binding site characteristics.

Sitemap analysis of each PPAR representative pose indicates that hydrophobic surface interactions outweigh hydrophilic surface interactions for all isoforms (**Figure 5.**). This is represented by the ratio of hydrophobic to hydrophilic surface area, also known as the balance score. The balance score provides valuable insights into the proteins' structural and functional properties. Docking scores favor more prominent hydrophobic ligands, as Van der Waals (vdW) interactions increase relative to protein hydrophobic surface area. While docking scores may not accurately represent the activity as it correlates to experimental EC_{50}/IC_{50} values, they can accurately capture ligand binding poses that distinguish conformational preferences associated with the activity.

Sitemap analysis showed that the PPARδ receptor site shares a similar volume to that of PPARγ and a similar hydrophilic surface area to that of PPARα. However, the PPARδ receptor site deviates significantly in terms of its hydrophobic surface area, approximately two times that of PPARγ and PPARα. Therefore, ligands with strong hydrophobic character are more likely to bind tightly with the PPARδ receptor site relative to PPARγ and PPARα. The balance score of 3.596 for the PPARδ receptor site indicates a predominance of hydrophobic character that can be exploited for ligand selectivity.

Figure 5. Result from SiteMap Analysis of PPARγ, PPARα, and PPARδ

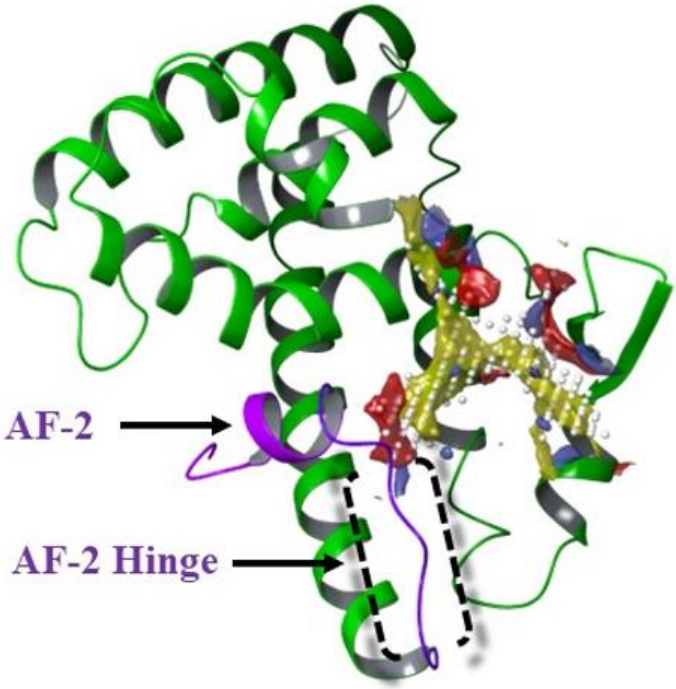

PPARγ – LBD
(PDB: 5Y2O)

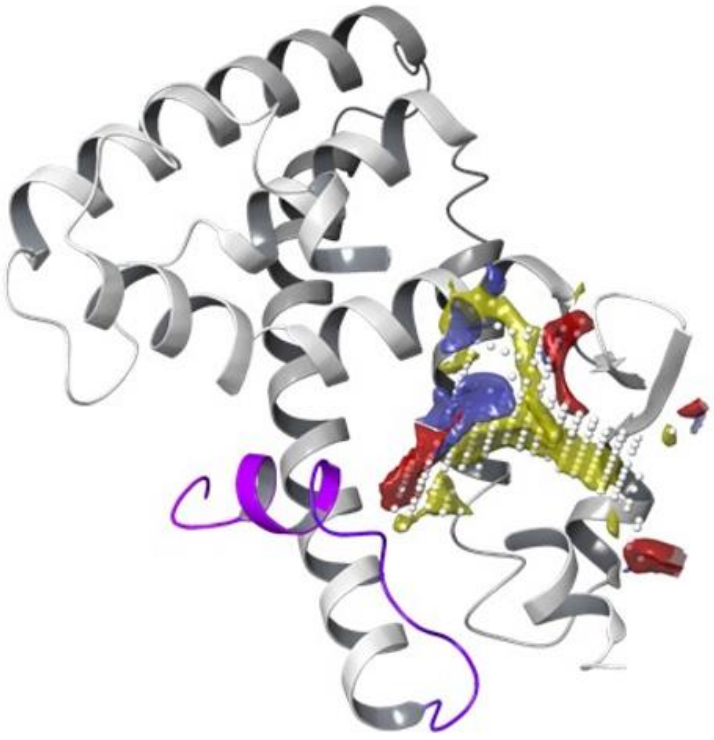

PPARα – LBD
(PDB: 3VI8)

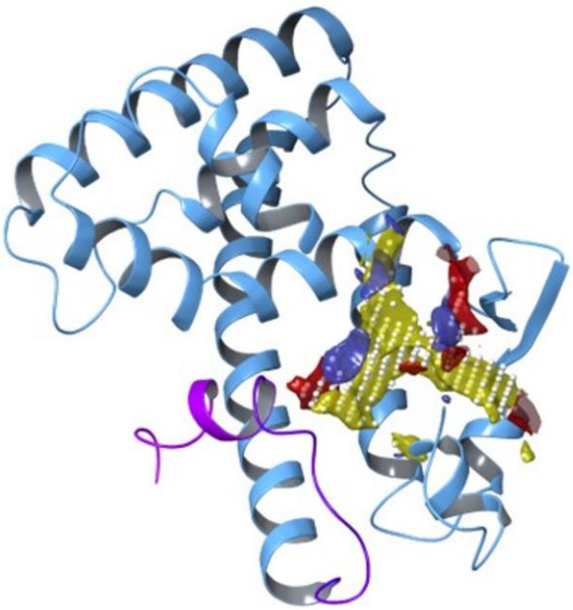

PPARδ – LBD
(PDB: 3TKM)

Sitemap Descriptors	PPARγ	PPARα	PPARδ
Volume	350	473	397
Phobic	1.472	1.073	2.385
Philic	0.838	0.589	0.664
Balance	1.756	1.822	3.594
Dscore	1.114	1.125	1.196

PPAR sitemap visual analysis: **Hydrogen-bond Acceptor map**, **Hydrogen-bond Donor map**, and **Hydrophobic map**. Phobic—regions that are favorable for occupancy by hydrophobic ligand groups. Philic—regions that are favorable for occupancy by hydrophilic ligand groups. The phobic and philic scores have been calibrated so that the average score for a tight-binding site is 1.0. Balance – phobic/philic. Dscore = 0.094 sqrt(n) + 0.60 e - 0.324 p. *n* – number of site points. *e* – enclosure score. *p*- hydrophilic score. Dscore values greater than 1 represent hydrophobic sites suitable for tight binding.

2.2.2 In Silico PPAR Structural Optimization: Initial Structure Identification of AU-9

Glide is a software tool available in the Schrodinger Maestro Suite used for molecular docking, which predicts the position and orientation of a ligand molecule relative to a receptor molecule. The goal is to identify a ligand's lowest energy binding mode with a given receptor, which can provide insight into the ligand's potential biological activity and help design new drugs. Glide can be run in two modes: rigid or flexible docking. The ligand is treated as a rigid molecule in the former, whereas in the latter, the ligand is allowed to adopt different conformations. The ligand position, orientation, and conformation combination is called a ligand pose.

Glide employs a comprehensive series of hierarchical filters to rigorously evaluate the ligand-receptor interactions. These filters meticulously test the spatial fit of the ligand to a pre-determined receptor site grid and scrutinize the complementarity of ligand-receptor interactions using a grid-based method. The initial filters are based on the empirical ChemScore function, which thoroughly evaluates the non-bonded interactions between the ligand and the receptor. The poses that successfully pass these initial screens proceed to the final stage of the algorithm, which involves evaluating and minimizing a grid approximation to the non-bonded interaction energy between the ligand and the receptor.

The final scoring of the poses is carried out using GlideScore, a multi-ligand scoring function developed by Schrödinger. The GlideScore combines several factors, such as the non-bonded interaction energy, the excess internal energy of the ligand conformation, and other terms that account for the entropy and desolvation effects. The composite Emodel score ranks each ligand pose and selects the best ones to report to the user. The Emodel score combines the

GlideScore and the non-bonded interaction energy, and it is a measure of the predicted binding affinity of the ligand to the receptor.

Initial structure identification is a crucial phase in drug discovery. It involves identifying chemical compounds with desired biological activity against a target, such as a disease-associated protein. This phase begins with target identification and validation, confirming that modulating the target's activity has a therapeutic effect.

Based on the previous experimental activity data of AU-9, Ligand-Based Virtual Screening (LBVS) was used to better understand this apparent PPARδ selectivity. LBVS is a computational approach used in drug discovery to identify new compounds that may exhibit similar biological activity to known active molecules. This technique relies on the structural and chemical properties of previously identified active ligands to screen virtual libraries of compounds. The process begins with constructing a pharmacophore model defining the essential features required for biological activity, such as hydrogen bond donors, acceptors, hydrophobic regions, and aromatic rings. By comparing these features against virtual compounds, LBVS can identify those that match the pharmacophore model, suggesting potential activity against the target. Additionally, similarity searches are performed using molecular structural fingerprints and other chemical descriptors to identify a compound's similarity to known actives. LBVS is advantageous because it can be useful to identify novel scaffolds and chemotypes, which can then be synthesized and tested experimentally.

GW-0742, a potent PPARδ agonist; rosiglitazone, a potent PPARγ agonist; and APHM13, a potent PPARα agonist, were used as comparisons in ligand docking studies to evaluate the apparent PPARδ selectivity of AU-9. Ligand docking poses were generated and evaluated by observing specific ligand binding poses and receptor contacts associated with

respective experimental EC_{50} values. Noticeably, potent PPAR agonists characteristically display a distinct binding motif with their representative LBD AF-2 domain.

All PPAR isoforms contain a Tyrosine residue centrally located on the c-terminal H12 Helix, i.e., AF-2, surrounded by coordinating Histidine residues on both sides. PPAR active site moieties frequently interact with the AF-2 through hydrogen bonding or ion-dipole interactions, which dictates the ligand's specificity for recruiting coregulator proteins. The representative PPAR cognate poses used for ligand docking studies revealed distinct ligand conformational requirements required to access each respective PPAR AF-2 (**Figure 6.**).

AU-9 displays a large lipophilic branched chemical structure that prevents ligand access to the AF-2 in both the PPARα and PPARγ cognate poses. However, AU-9 can selectively access the PPARδ AF-2, albeit inversely to most ligands containing an acidic or basic active site moiety. AU-9 instead prefers to conformationally align the 3,5-bis trifluoromethyl phenyl ring into the PPARδ AF-2 (Figure 9). The PPARδ LBD relies more on the ligand's steric "push" to reorganize the AF-2 into an active conformation. Thus, this domain is more accessible to complementary hydrophobic ligand contacts than PPARγ and, to a lesser extent, to that of PPARα (**Figure 7.**)

Figure 6. Representative PPAR Cognate Poses AF-2 Ligand Residue Conformations

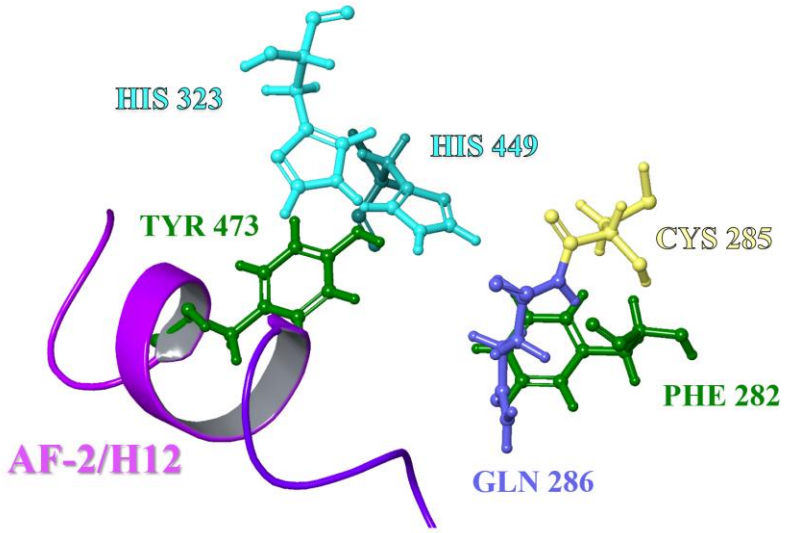

PPARγ – AF2

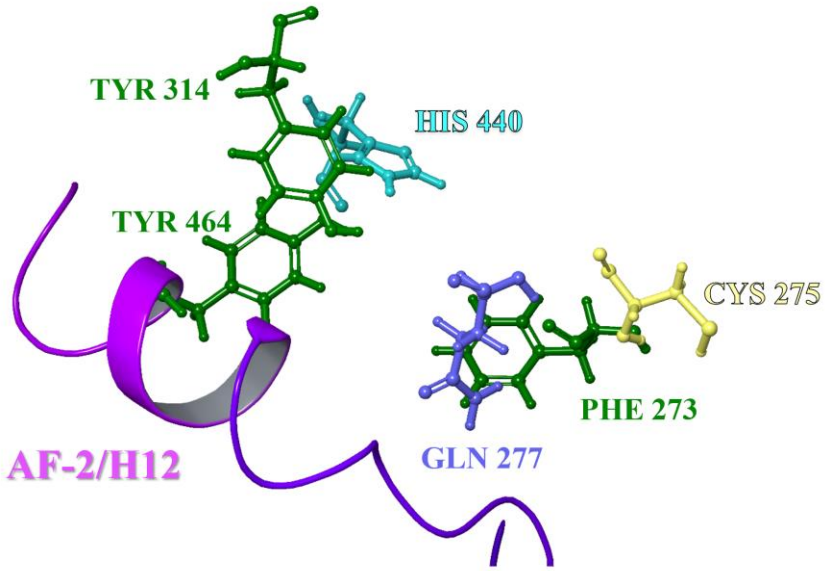

PPARα – AF2

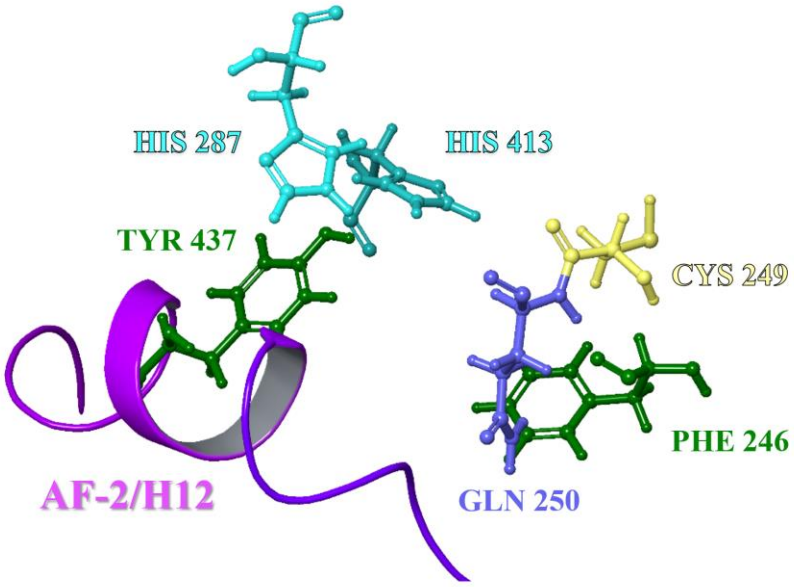

PPARδ – AF2

The PPAR LBD AF-2 domain amino acid residues are conserved, excluding the Tyrosine 314 residue in PPARα. However, the conserved Cysteine residue displays distinct conformations that direct the ligand's active site moiety via the polar anchor point to form interactions with the conserved AF-2/H12 Tyrosine residue.

Figure 7. In Silico PPAR SAR: Structure Identification of PPARδ Selective Agonist AU-9

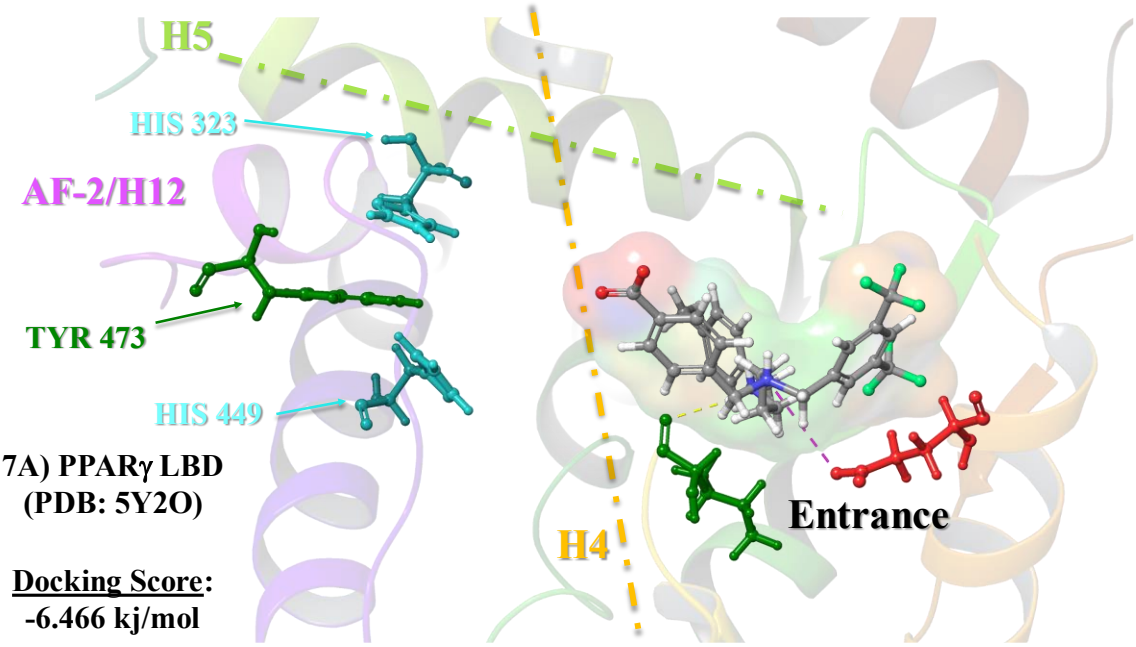

7A) PPARγ LBD (PDB: 5Y2O)

<u>Docking Score</u>: -6.466 kj/mol

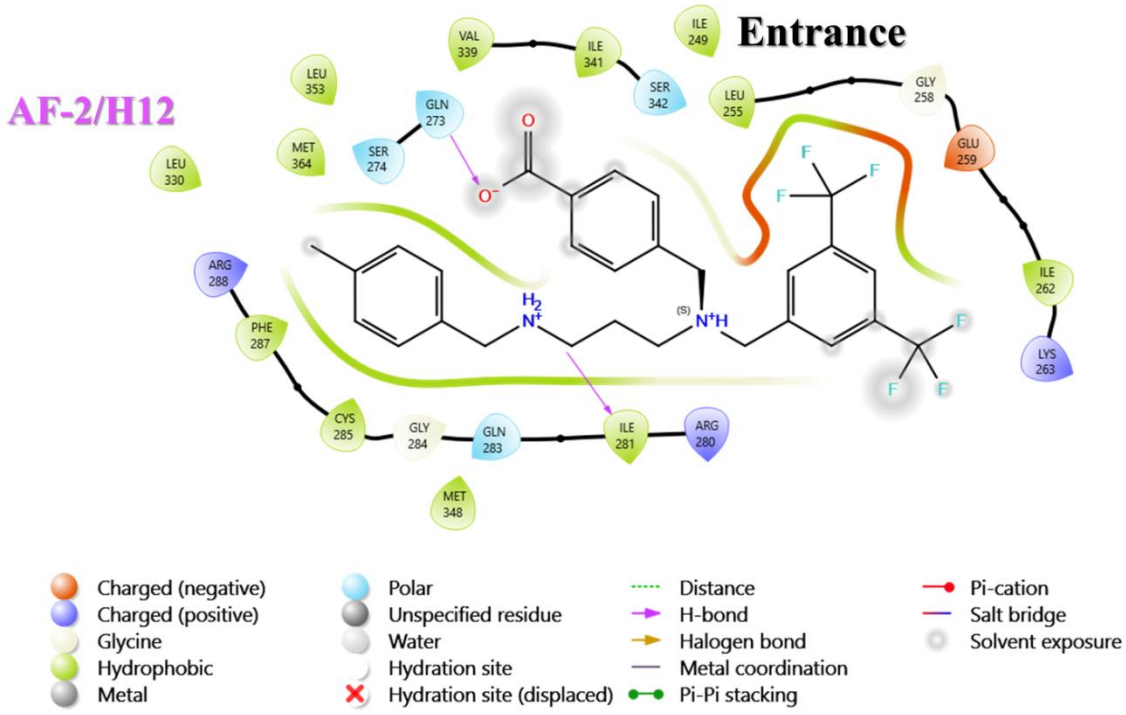

7A. Predictive binding pose of AU-9 in the PPARγ LBD) AU-9's lowest energy docking pose in the PPARγ LBD demonstrates the ligand's steric restrictions on accessing the AF-2, preferring to bind with its active site moiety near the entrance instead. The PDB: 5Y2O cognate crystal structure of the PPARγ LBD complexed with partial agonist pioglitazone indicates that ligand access to the AF-2 is crucial for activity as AU-9 was determined to have no apparent transactivation of PPARγ.

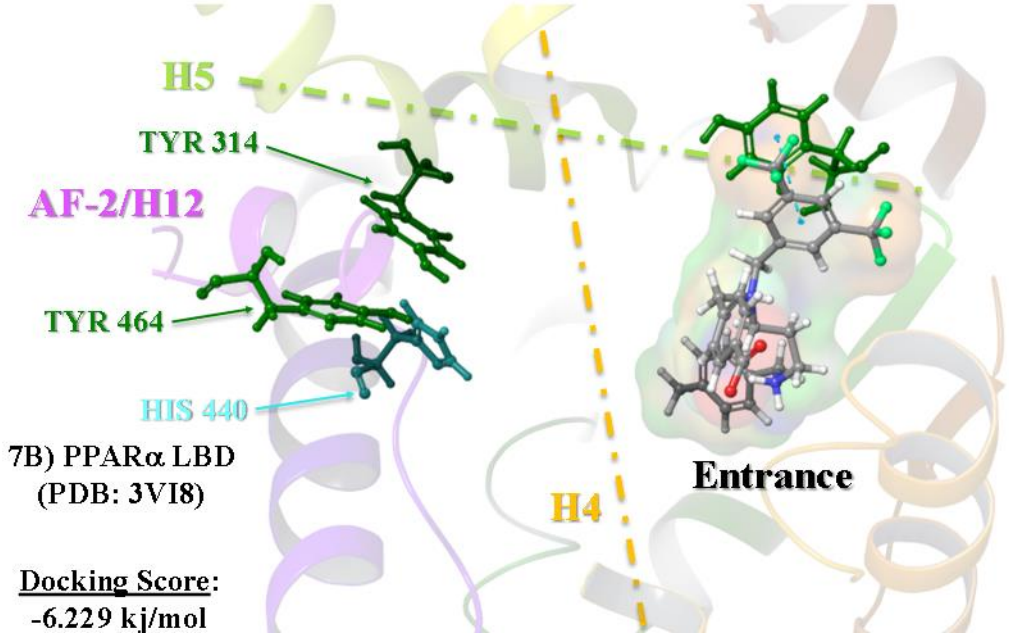

7B) PPARα LBD
(PDB: 3VI8)

Docking Score:
-6.229 kj/mol

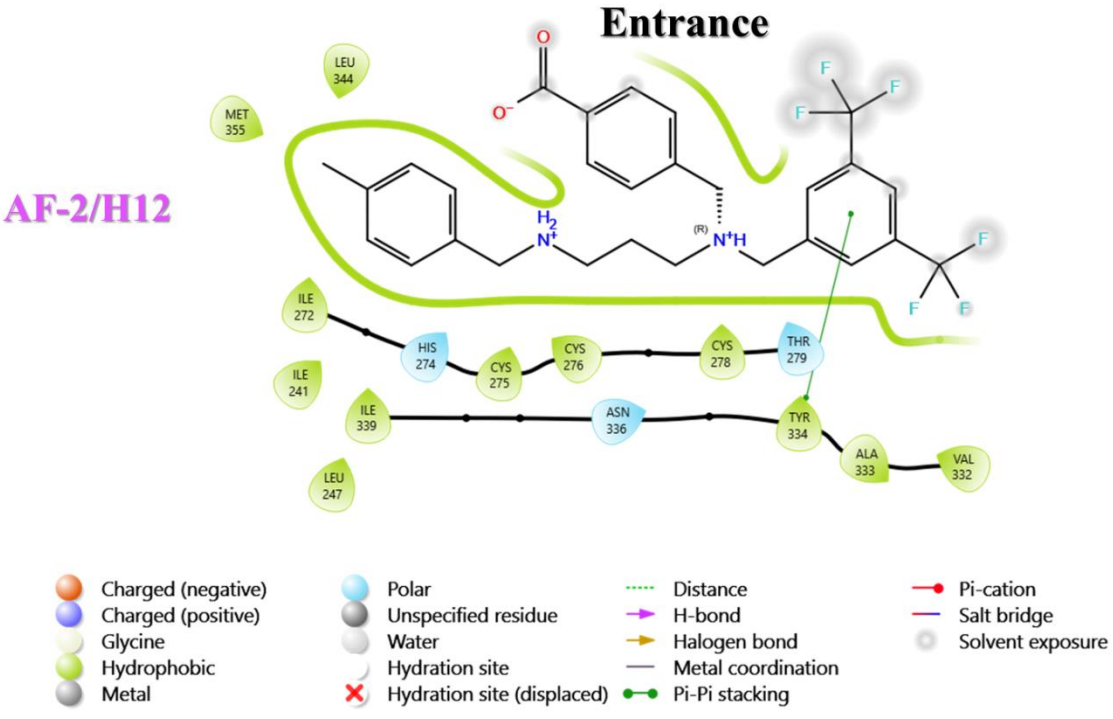

7B. Predictive binding pose of AU-9 in the PPARα LBD) AU-9's lowest energy docking pose in the PPARα LBD demonstrates similar steric restrictions for accessing the AF-2 as was observed at PPARγ. The PDB: 3VI8 cognate crystal structure of the PPARα LBD complexed with a potent agonist APHM13 indicates that ligand access to the AF-2 is independent of the steric bulk associated with the hydrophobic tail as the cognate ligand displays pyrene functionality and an experimental EC_{50} value of 43 nM.

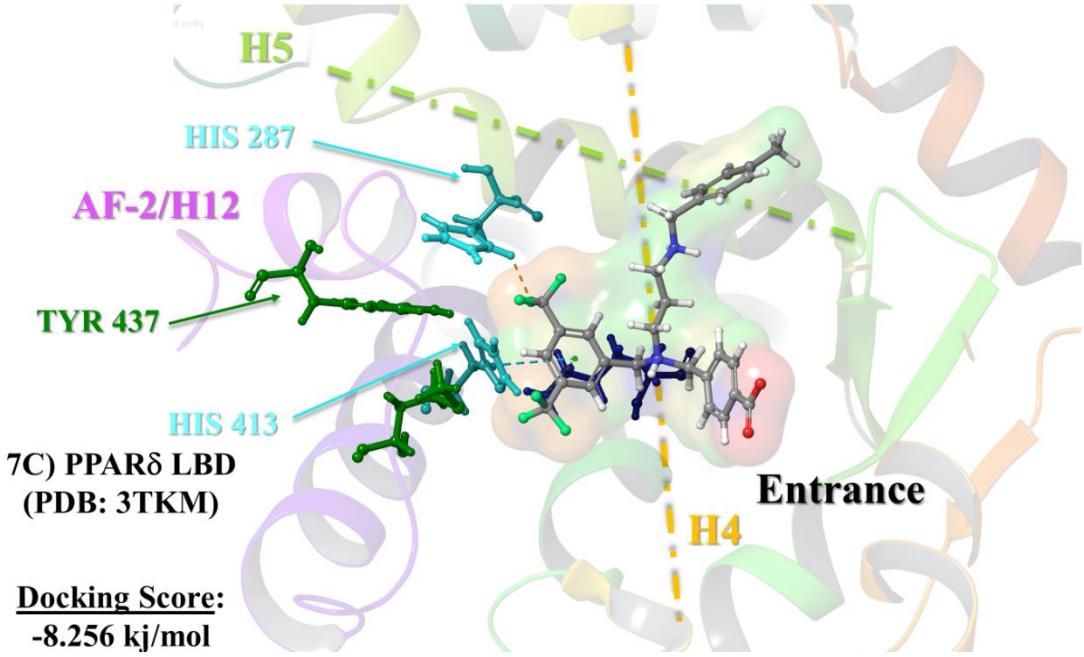

7C) PPARδ LBD
(PDB: 3TKM)

Docking Score:
-8.256 kj/mol

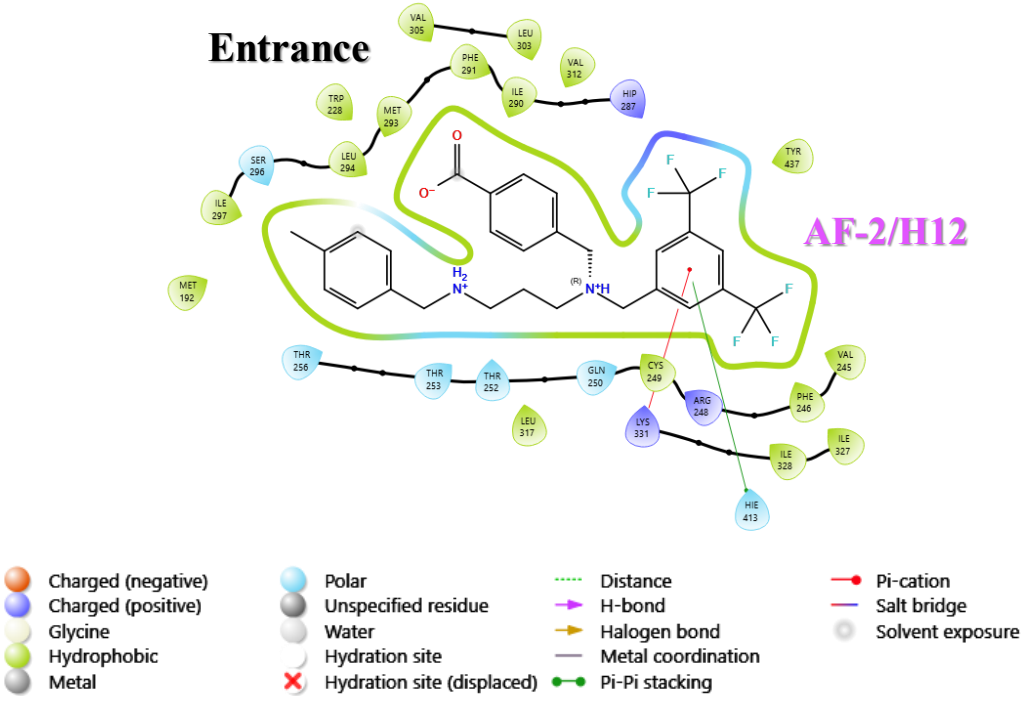

7C. Predictive binding pose of AU-9 in the PPARδ LBD) AU-9's lowest energy docking pose in the PPARδ LBD conversely demonstrates a steric requirement to access the AF-2, unlike the observations of PPARα and PPARγ. Interestingly, AU-9 displays a consistent binding conformation across all three PPAR isoforms. However, the PPARδ AF-2 favorably aligns with the weakly polar 3,5-bis trifluoromethyl phenyl hydrophobic tail. The PDB: 3TKM cognate crystal structure of the PPARδ LBD complexed with a potent agonist GW-0742 indicates that ligand access to the AF-2 is independent of the steric bulk associated with the active site moiety as the cognate ligand displays a phenoxy acetic acid functionality.

2.2.3 In Silico PPAR Structural Optimization: AU-9 to Compound 7 (AU-403)

The lead compound AU-9 was shown to be a strong PPARδ agonist with no apparent activation of PPARγ. However, AU-9 had a molecular mass of 538 g/mol and was not conducive to biodistribution towards the brain. Additionally, AU-9 did not display PPARα activity, a target of interest related to the astrocytic metabolism of lipids in AD. Therefore, compound 7 (AU-403) was designed to limit PPARγ activity, improve PPARα activity, and maintain PPARδ activity, emphasizing BBB distribution.

The AU-9 benzoic acid was determined to be the major contributor to the limited PPARγ activity, as the bulkier benzene creates steric hindrance, restricting favorable alignment and contacts for the active site moiety to the AF-2 domain. The weakly polar trifluoromethyl phenyl functionality on AU-9 was conducive to PPARδ activity, but the bulky branched structure limited PPARα conformational requirements for activity similar to PPARγ. Thus, the compound 7 (AU-403) design maintains these features while removing molecular mass and charge. Additionally, ADME Toxicity predictions were used to guide the efficiency of the molecular changes in combination with docking scores and conformational alignment with the PPAR AF-2 (**Figure 8.**).

Figure 8. Structural Optimization of the AU-9 PPARδ Selective Agonist to AU-403 PPARα/δ Selective Agonist

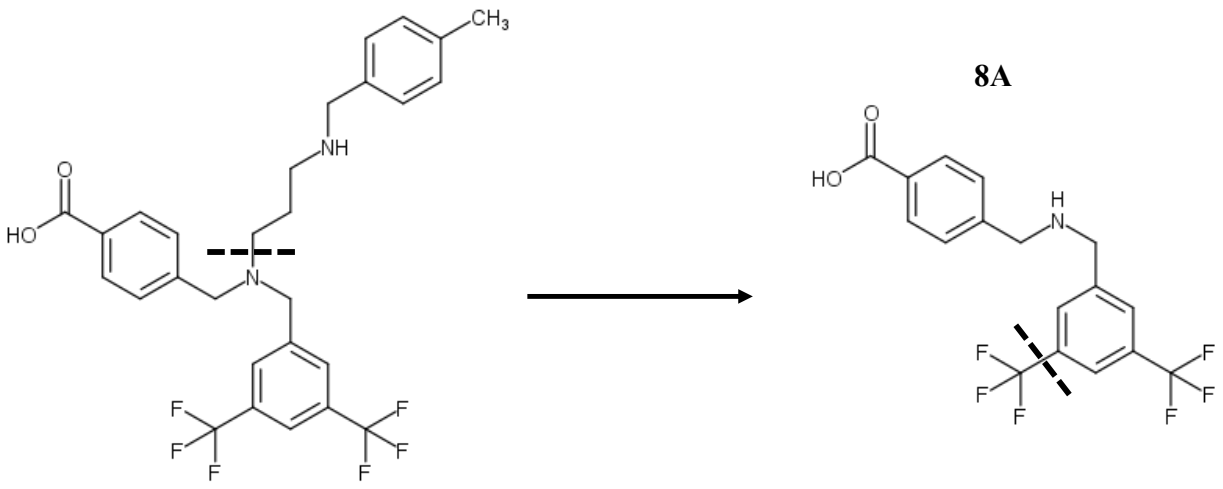

Structure	mol_MW	QPlogPo/w	QPPCaco	QPlogBB	QPPMDCK	Human Oral Absorption
AU9	538.532	4.748	11.64	-0.149	104.557	1
Mod1	**377.286**	**2.628**	**42.736**	**-0.005**	**448.473**	**2**

8A) The first modification (mod1) of the AU-9 structure was to remove the bridged hydrophobic tail to decrease molecular mass, charge, and conformational ambiguity. The cell membrane is primarily composed of a lipid bilayer, which is hydrophobic. This hydrophobic environment favors the passage of nonpolar or moderately polar molecules but poses a significant barrier to highly charged molecules. Consequently, Mod1 displays improved ADME Tox predictions across all criteria considered for oral bioavailability and BBB permeability.

8A-1. AU-9 Modification 1 (Mod1) PPARγ Predicted Binding Pose

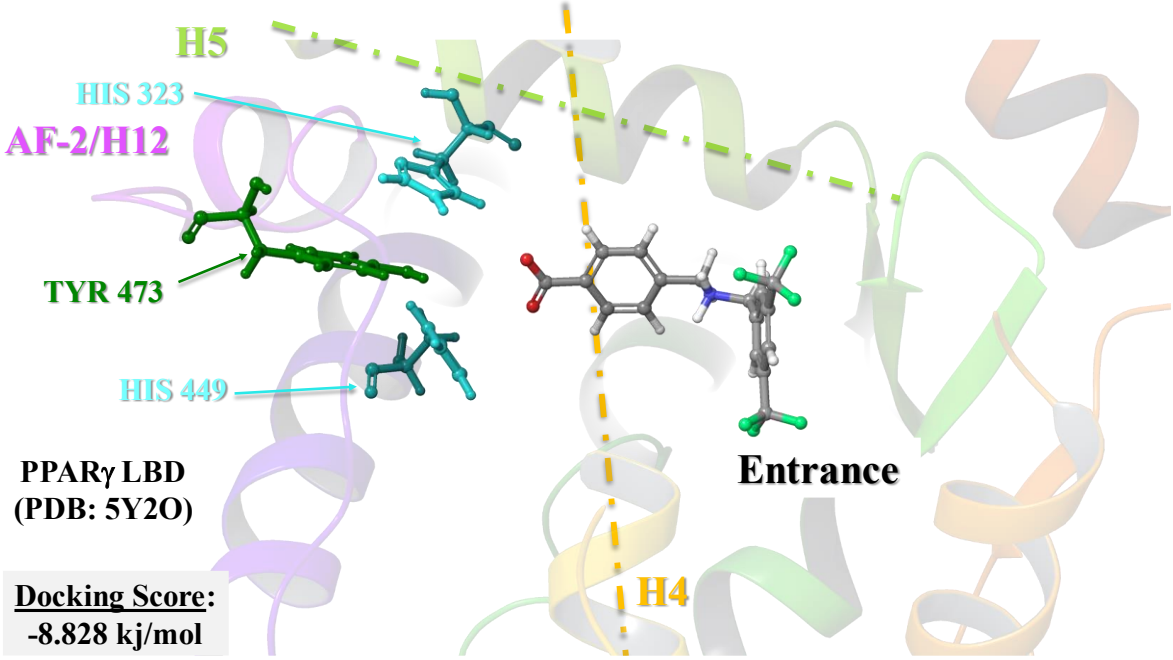

Docking Score:
-8.828 kj/mol

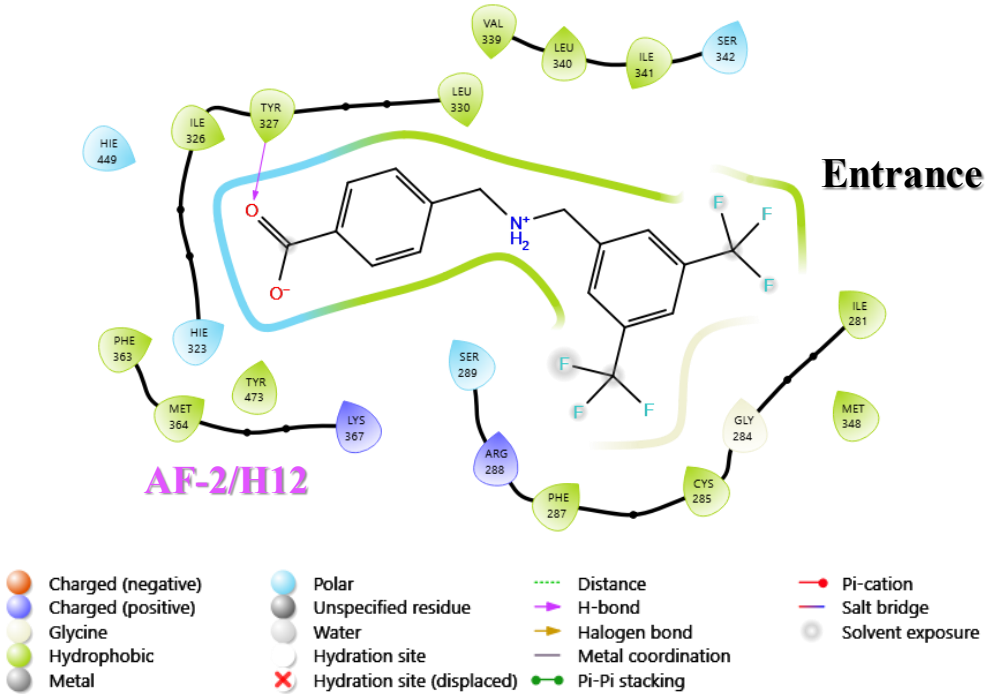

8A-2. AU-9 Modification 1 (Mod1) PPARα Predicted Binding Pose

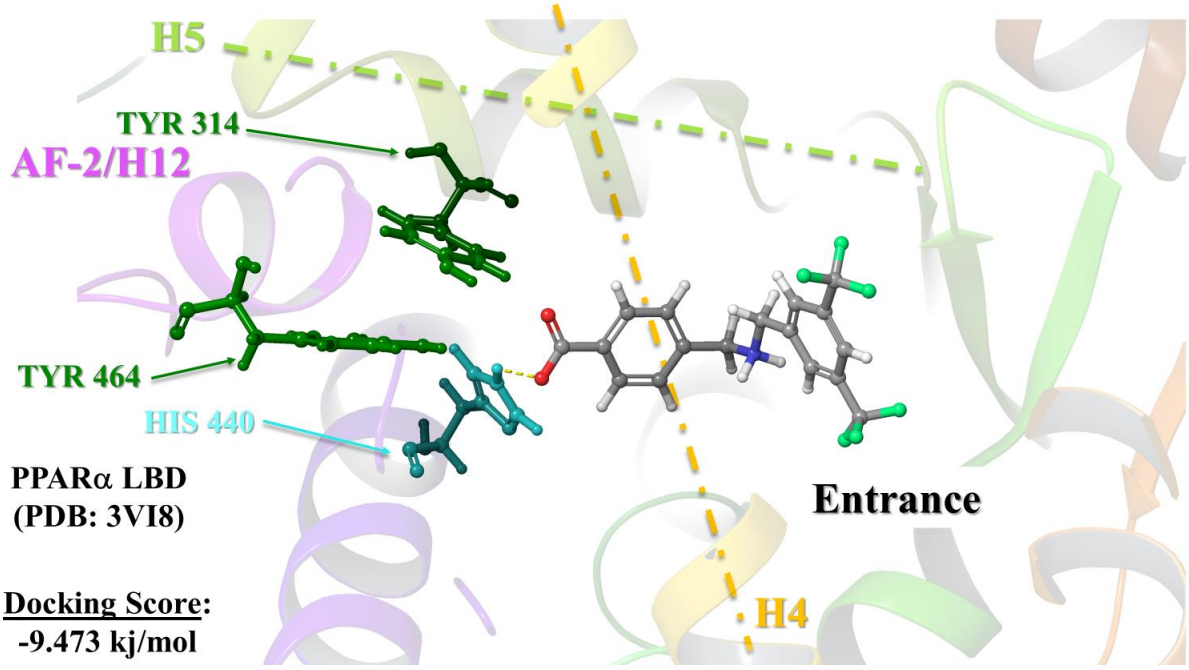

Docking Score:
-9.473 kj/mol

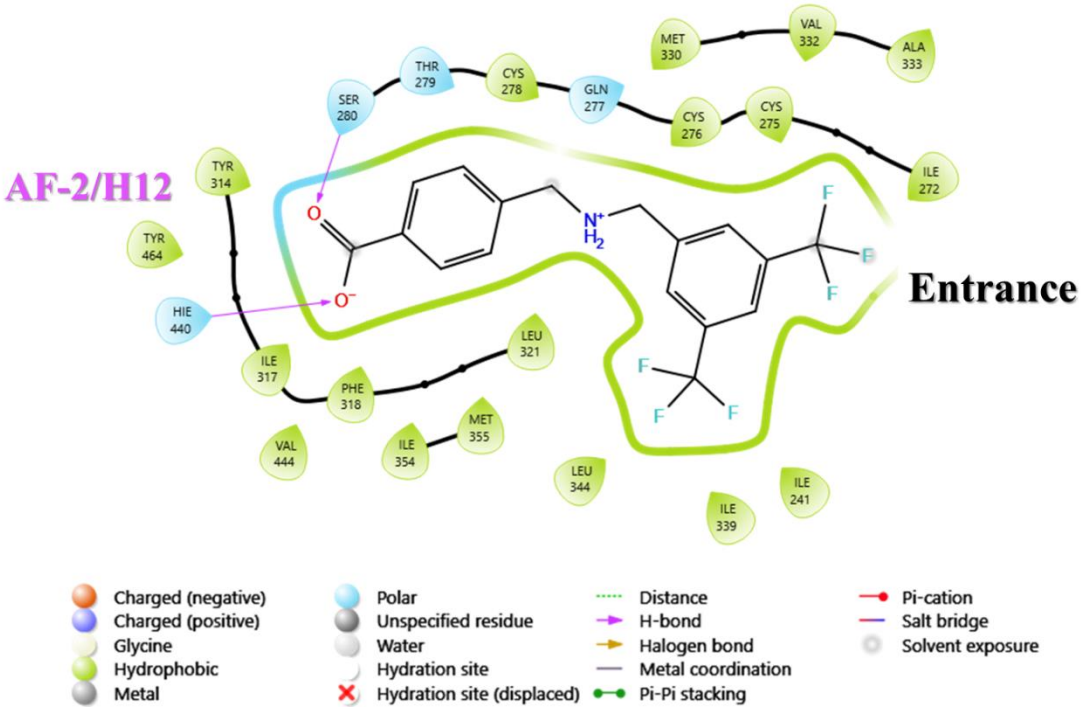

8A-3. AU-9 Modification 1 (Mod1) PPARδ Predicted Binding Pose

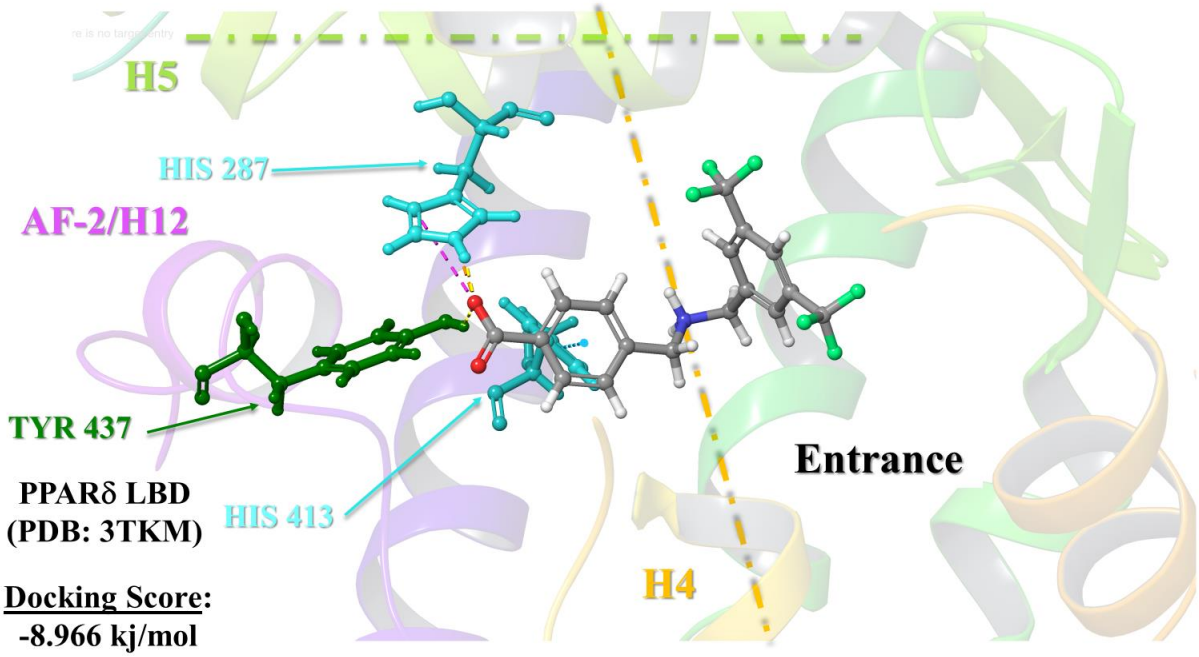

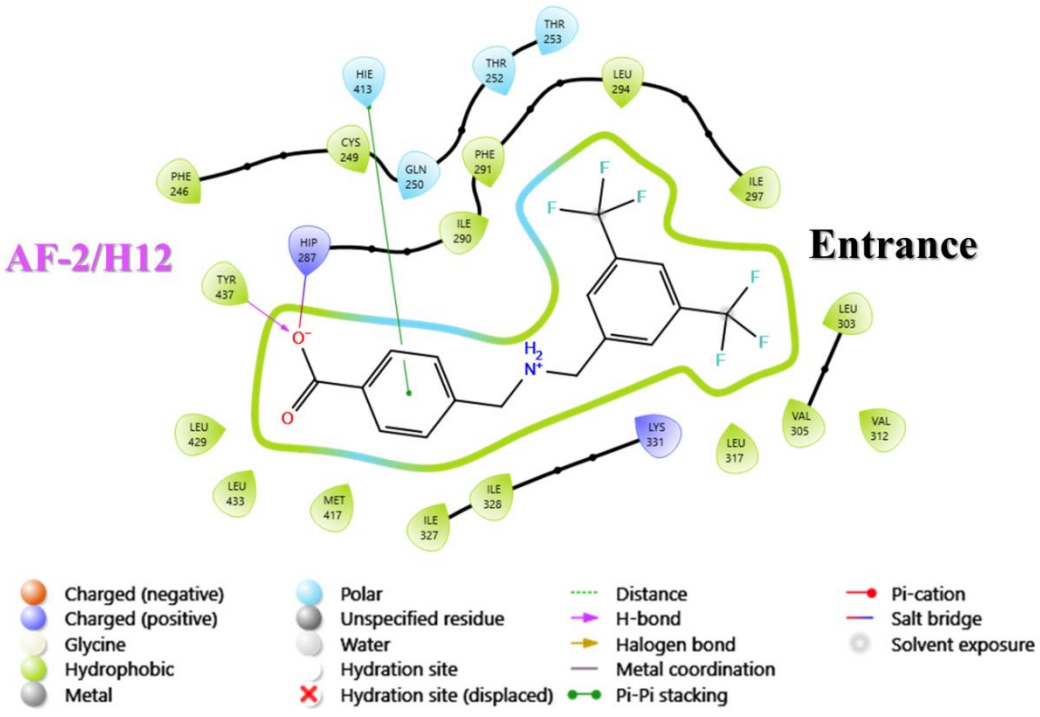

8A-1) Despite the limitation of Mod1 from extending far into the PPARγ AF-2, the docking scores have shown a notable improvement over AU-9. Although sterically hindered from entering the cognate pose AF-2 domain, the para benzoic acid still holds the potential for making robust contacts under conformational flux.

8A-2) Mod1 can extend closer to the PPARα AF-2, but the steric hindrance from the bis trifluoromethyl phenyl prevents contact between the para benzoic acid active site moiety and the AF-2 Tyrosine 464 residue. Mod1 docking scores have improved considerably from AU-9.

8A-3) Mod1 favorably forms strong coordinated contacts with the Tyrosine 437 AF-2 residue and accompanying Histidine residues. Docking scores have slightly improved over AU-9.

8B **8C**

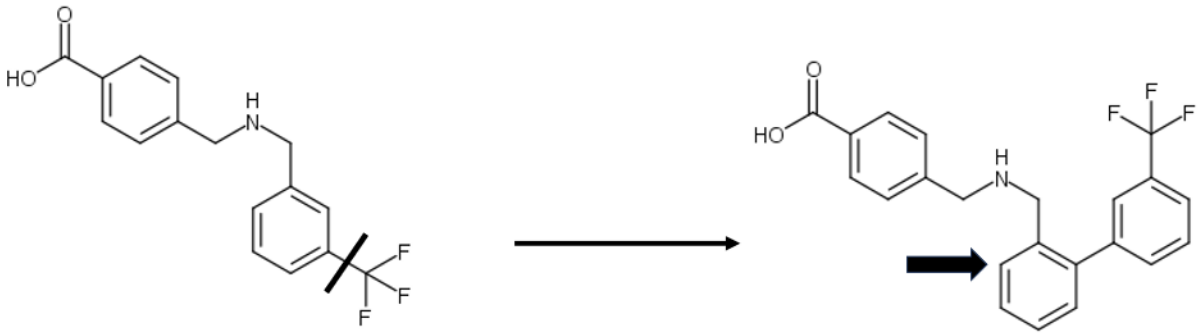

Modification 2 (Mod2) **Modification 3 (Mod3)**

Structure	mol_MW	QPlogPo/w	QPPCaco	QPlogBB	QPPMDCK	Human Oral Absorption
AU9	538.532	4.748	11.64	-0.149	104.557	1
Mod1	377.286	2.628	42.736	-0.005	448.473	2
Mod2	**309.287**	**1.768**	**48.149**	**-0.229**	**115.374**	**3**
Mod3	**385.385**	**2.551**	**70.532**	**-0.019**	**121.612**	**3**

8B) A trifluoro methyl was removed from the phenyl ring in the hydrophobic tail to get to Modification 2 (Mod2). Predictably, the removal of the hydrophobic trifluoro methyl shows a decrease in the predicted LogP and a slight improvement in the predicted Caco cell permeability. However, this decrease in hydrophobicity also decreases LogBB and MDCK predictive criteria.

8C) To improve LogBB and MDCK permeability predictions, an extension of the hydrophobic tail from the 1-phenyl position using the 3-substituted trifluoromethyl phenyl Modification 3 (Mod3) was chosen. Consequently, this led to an increase in LogP, QPPCaco, LogBB, and QPPMDCK predictive criteria.

8B-1. AU-9 Modification 2 (Mod2) PPARγ Predicted Binding Pose

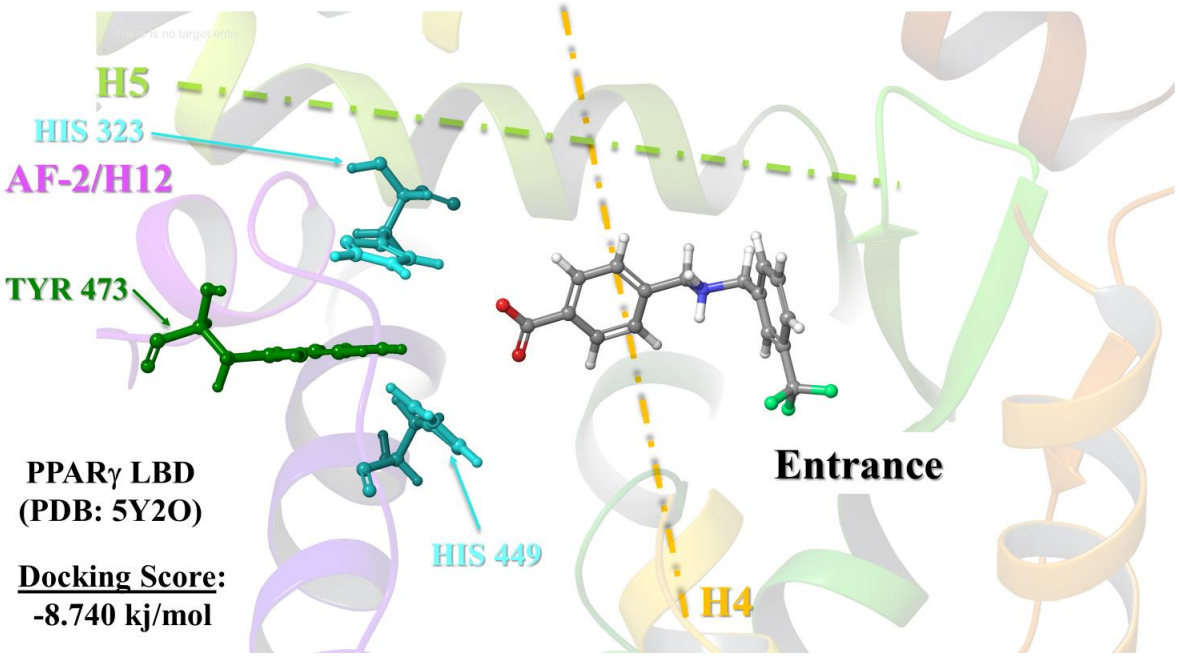

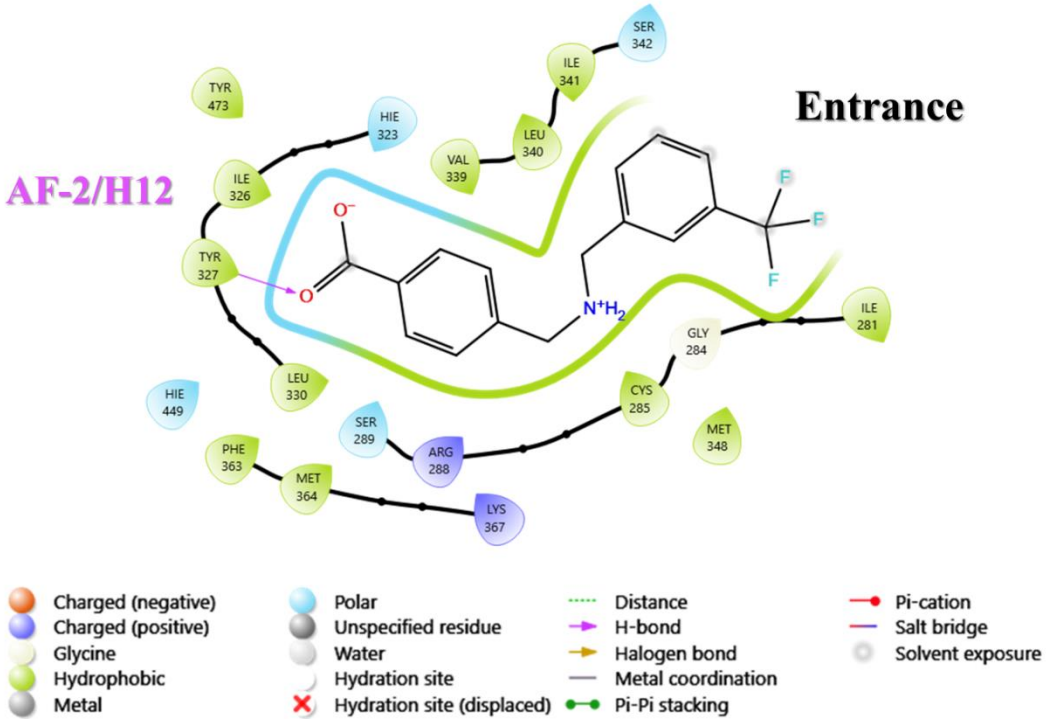

8B-2. AU-9 Modification 2 (Mod2) PPARα Predicted Binding Pose

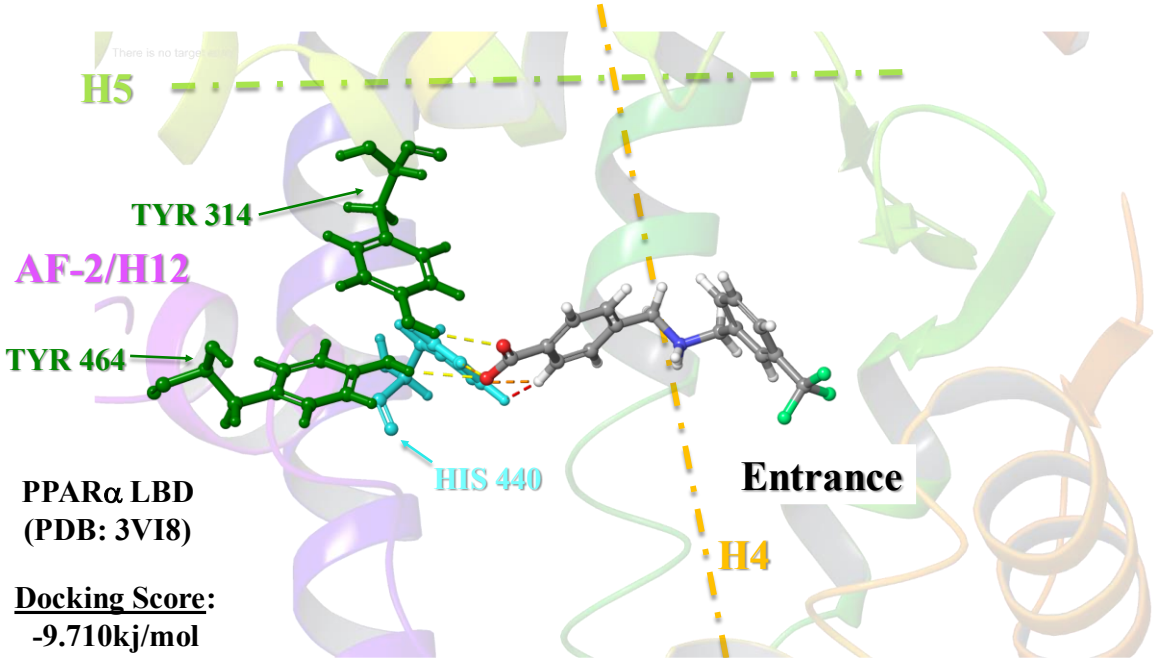

PPARα LBD
(PDB: 3VI8)

<u>Docking Score</u>:
-9.710kj/mol

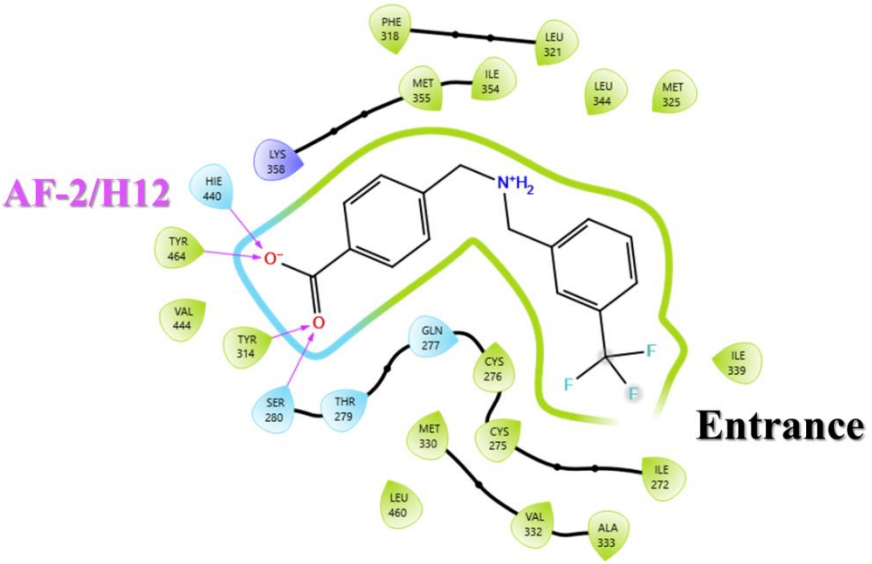

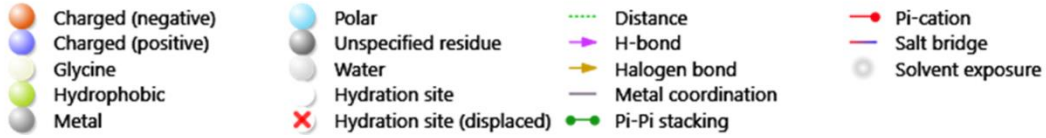

8B-3. AU-9 Modification 2 (Mod2) PPARδ Predicted Binding Pose

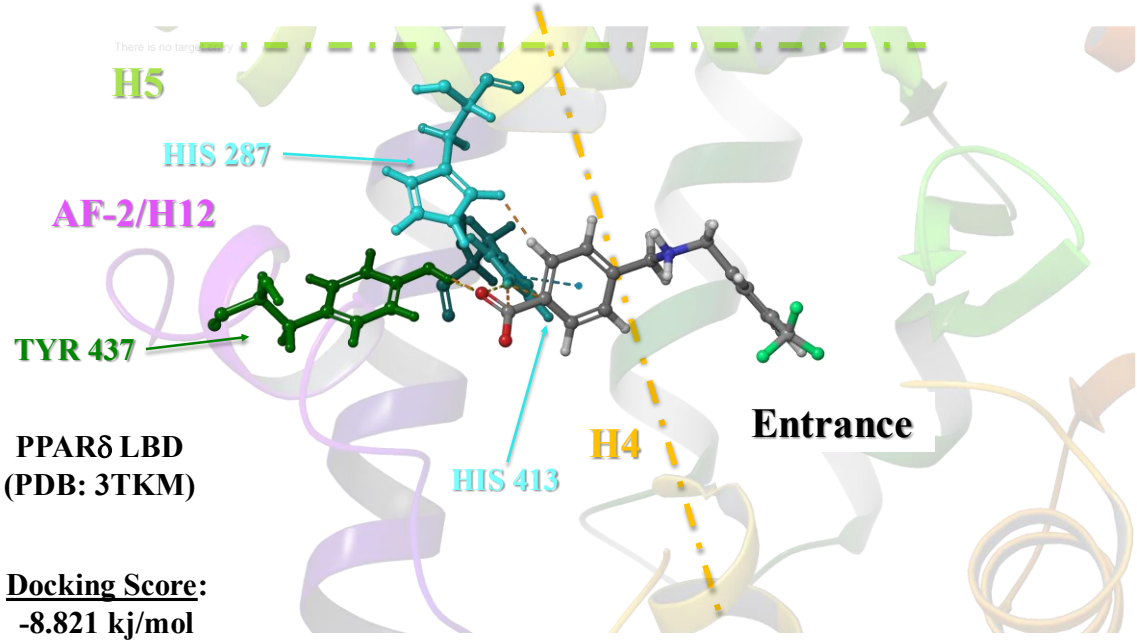

<u>Docking Score</u>:
-8.821 kj/mol

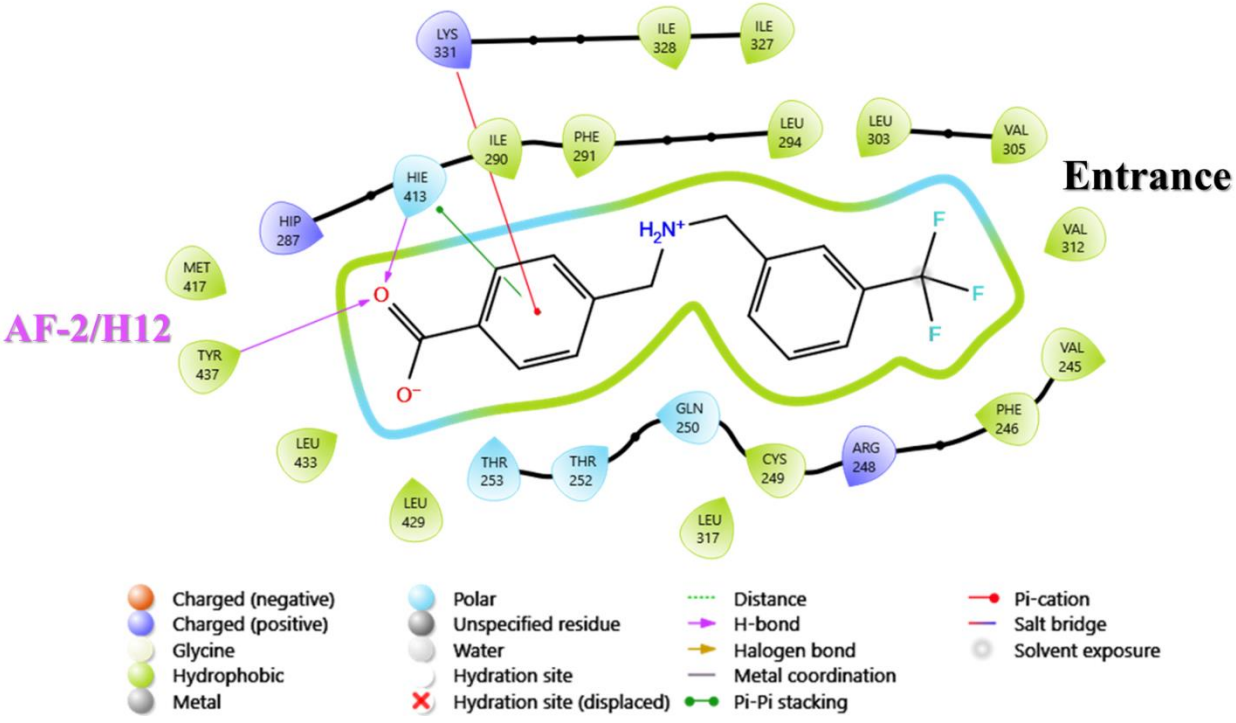

8B-1) Removing a trifluoromethyl substituent had little consequence on the PPARγ predicted binding pose of Mod2 with only a slightly increased docking score over Mod1.

8B-2) Removing a trifluoromethyl substituent allowed the Mod2 structure to now form strong contacts with the PPARα AF-2, which led to improved docking scores over Mod1.

8B-3) Mod2 forms coordinated contacts with the PPARδ Tyrosine 437 AF-2 residue and accompanying Histidine residues. However, these contacts are predominantly hydrophobic or aromatic, leading to increased docking scores for PPARδ.

8C-1. AU-9 Modification 3 (Mod3) PPARγ Predicted Binding Pose

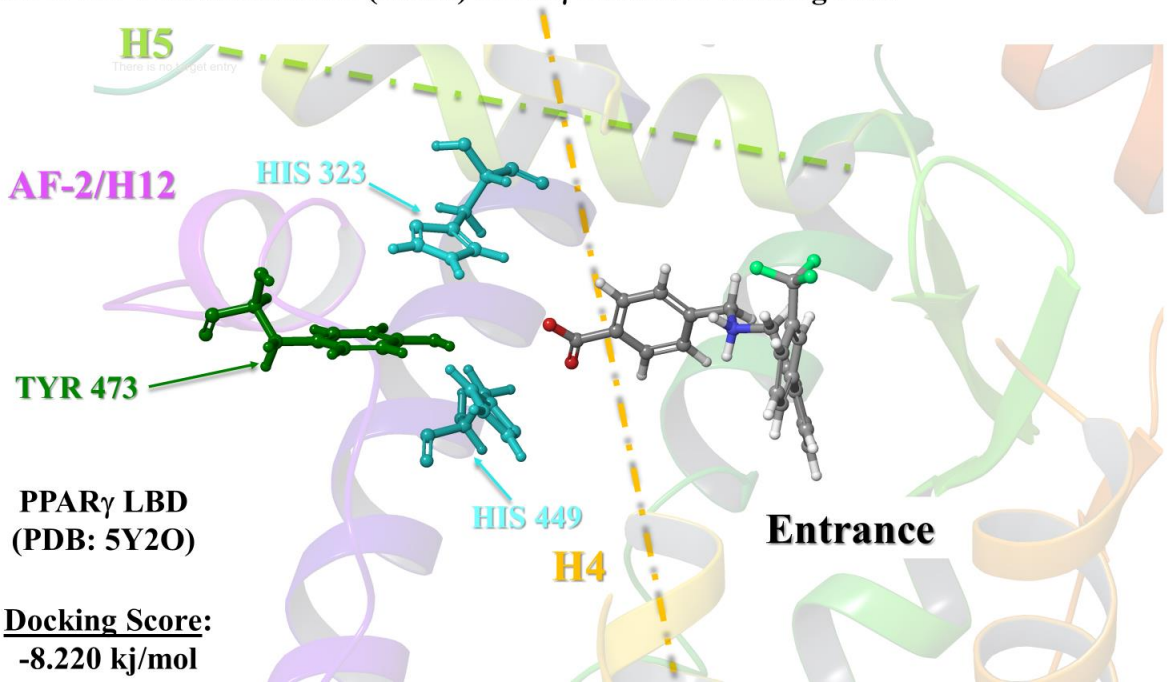

Docking Score:
-8.220 kj/mol

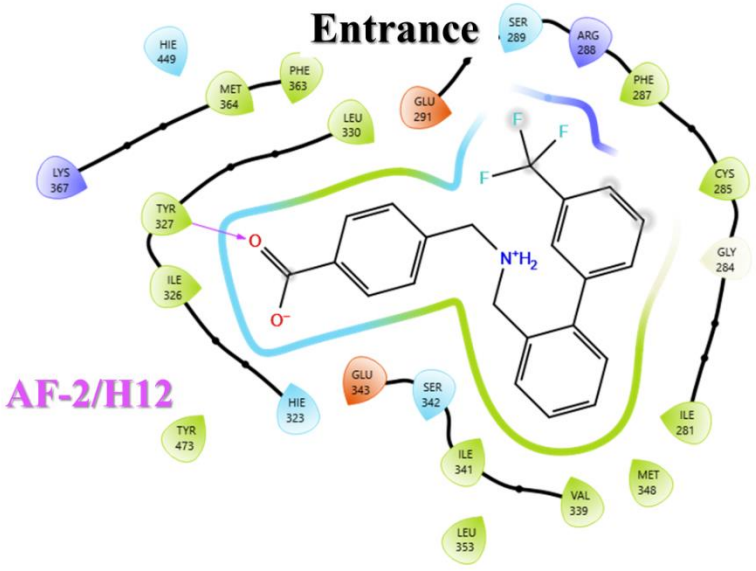

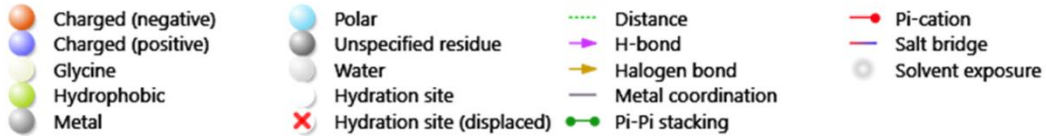

8C-2. AU-9 Modification 3 (Mod3) PPARα Predicted Binding Pose

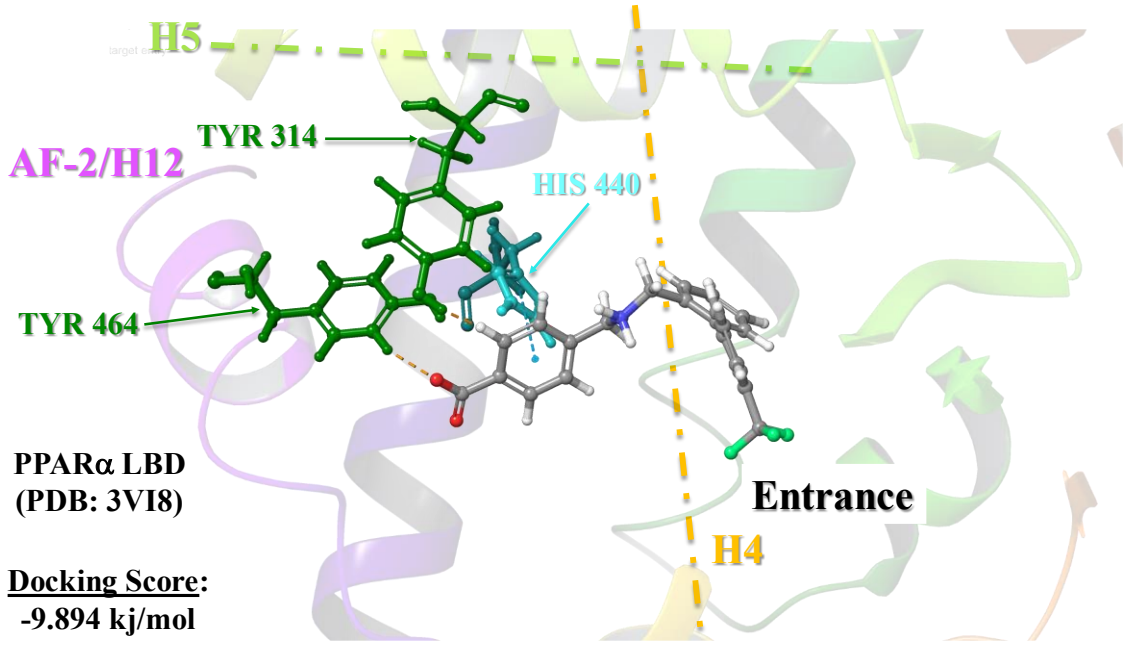

Docking Score:
-9.894 kj/mol

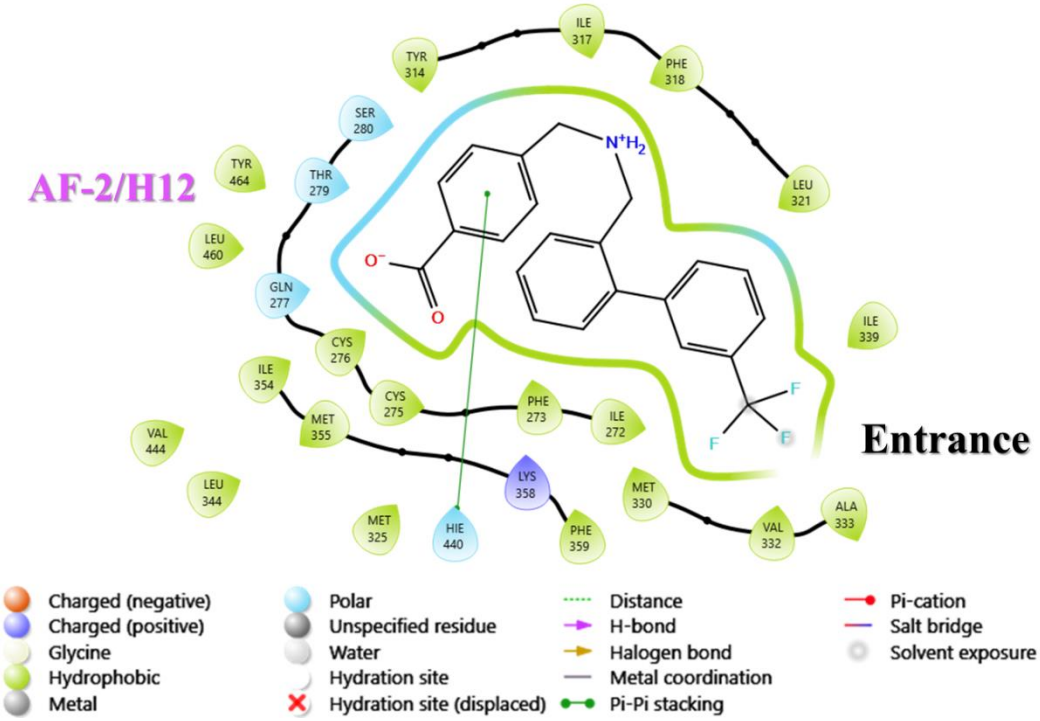

8C-3. AU-9 Modification 3 (Mod3) PPARδ Predicted Binding Pose

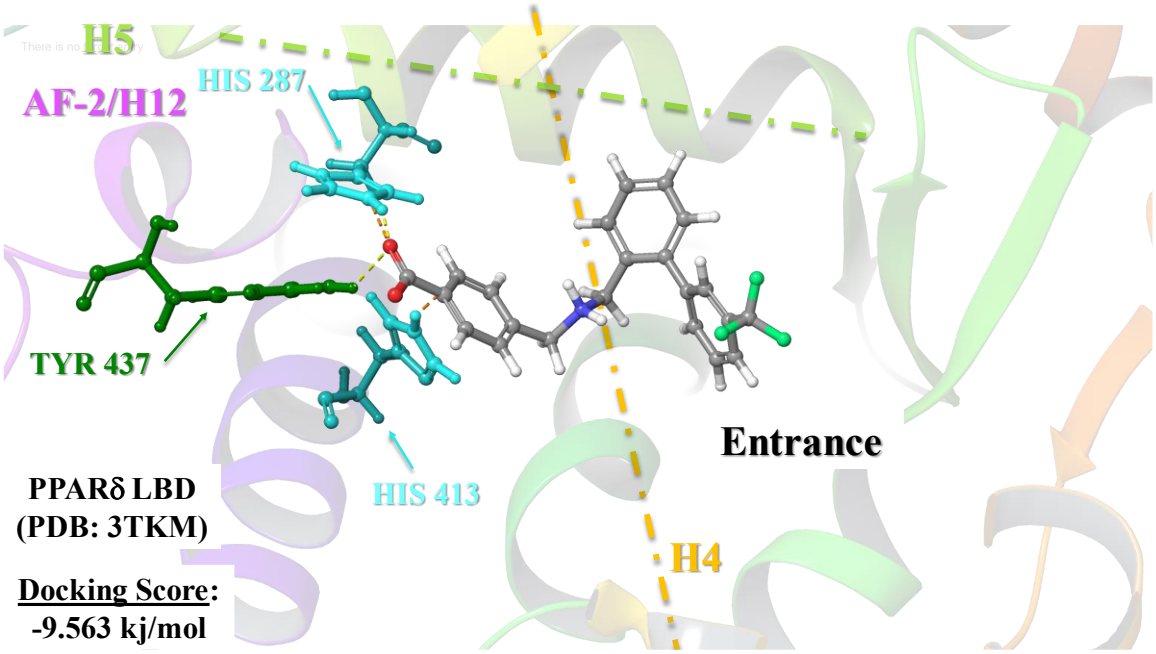

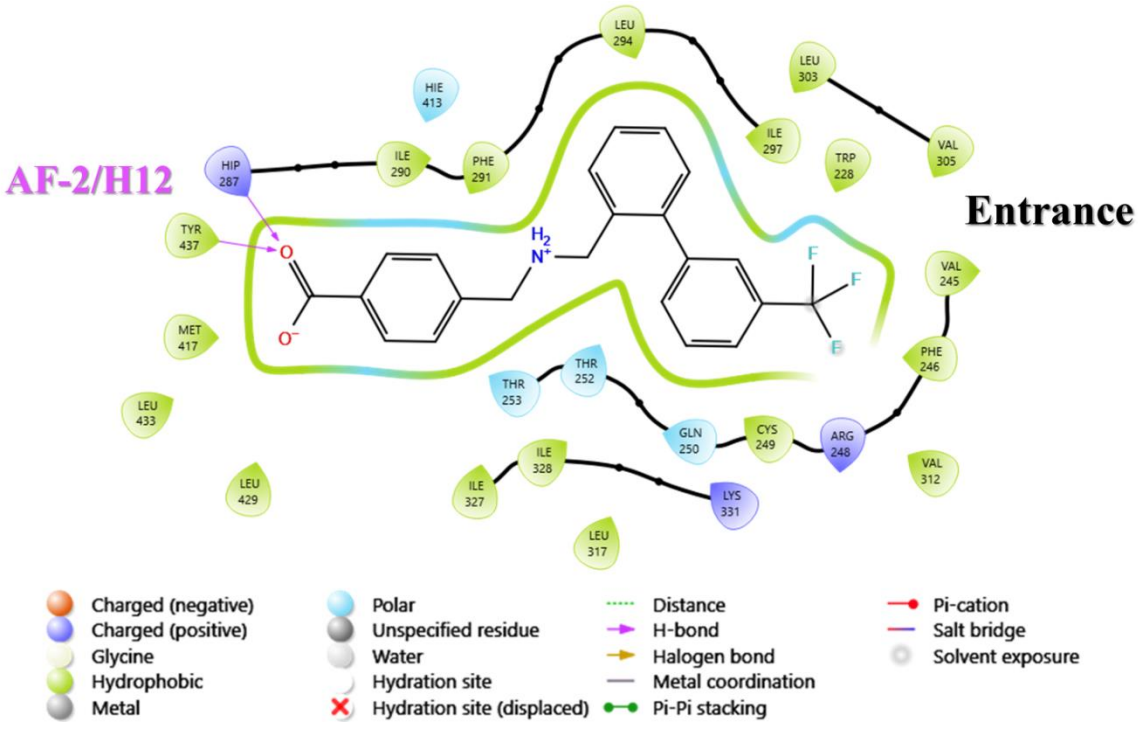

8C-1) Like Mod1, the Mod3 extension of the hydrophobic tail was observed to sterically restrict access to the PPARγ AF-2. This led to an increased Mod3 docking score as the hydrophobic tail displays a decrease in the weakly polar surface area associated with the Mod1 3,5-bis trifluoromethyl phenyl functionality.

8C-2) Conformational rotation around the connecting 1,1-biphenyl rings has favorably increased extension and contact with the PPARα AF-2. Additionally, docking scores have improved over Mod1 and Mod2.

8C-3) Mod3 active site moiety contacts with the PPARδ AF-2 have become more balanced between hydrogen bonds and hydrophobic interactions, improving docking scores over all previous modifications.

8D

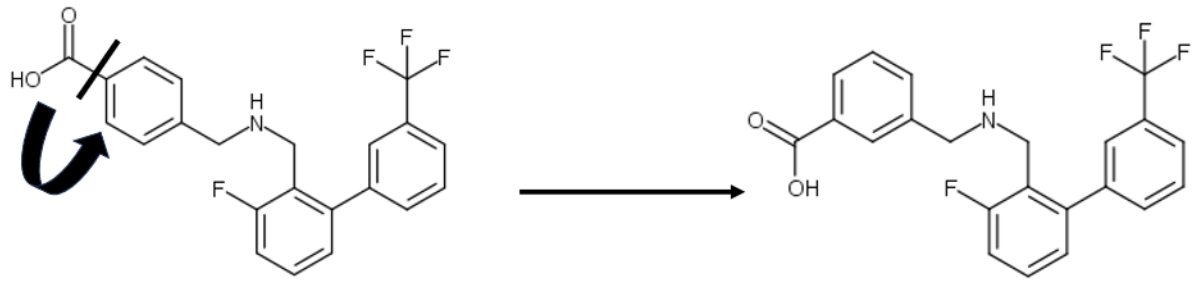

Modification 4 (Mod4) **Compound 7 (AU-403)**

Structure	mol_MW	QPlogPo/w	QPPCaco	QPlogBB	QPPMDCK	Human Oral Absorption
AU9	538.532	4.748	11.64	-0.149	104.557	1
Mod1	377.286	2.628	42.736	-0.005	448.473	2
Mod2	309.287	1.768	48.149	-0.229	115.374	3
Mod3	385.385	2.551	70.532	-0.019	121.612	3
Mod4	**403.375**	**3.126**	**54.911**	**-0.18**	**141.272**	**3**
AU-403	**403.375**	**2.748**	**74.741**	**0.08**	**198.16**	**3**

8D) A 3-fluoro substituent was added to the phenyl ring to increase the weakly polar surface area observed in Modification 4 (Mod4). This modification increased hydrophobicity with an unfavorable impact on LogP and Caco permeability predictions. However, MDCK permeability was favored over AU9, Mod2, and Mod3.

8D-1. AU-9 Modification 4 (Mod4) PPARγ Predicted Binding Pose

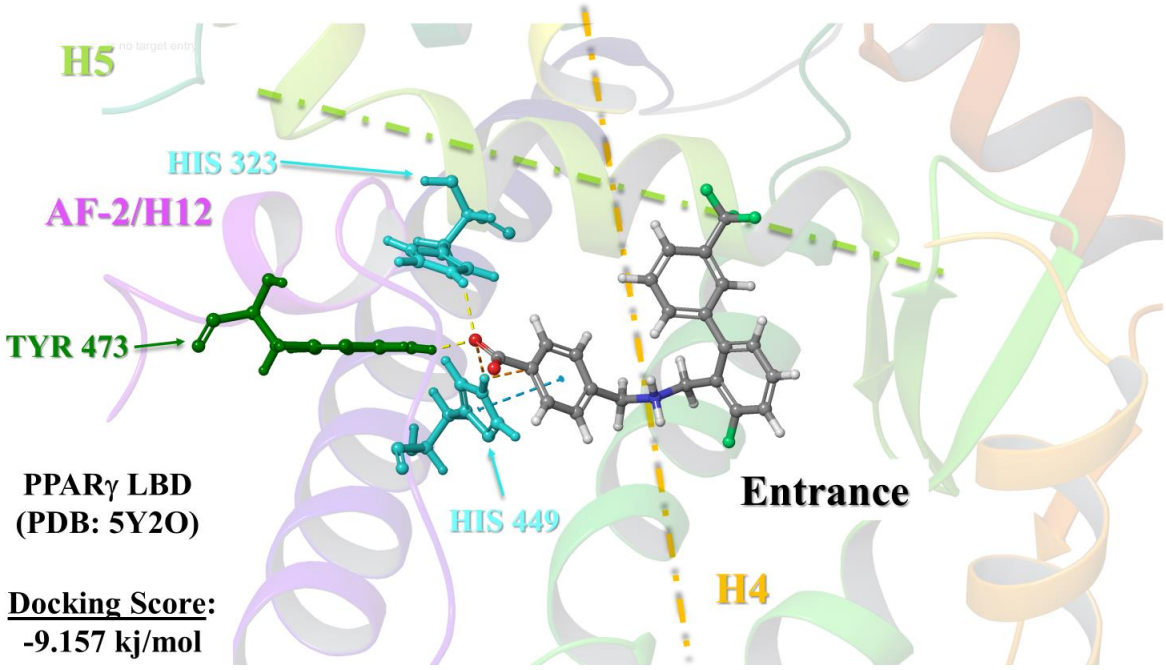

Docking Score:
-9.157 kj/mol

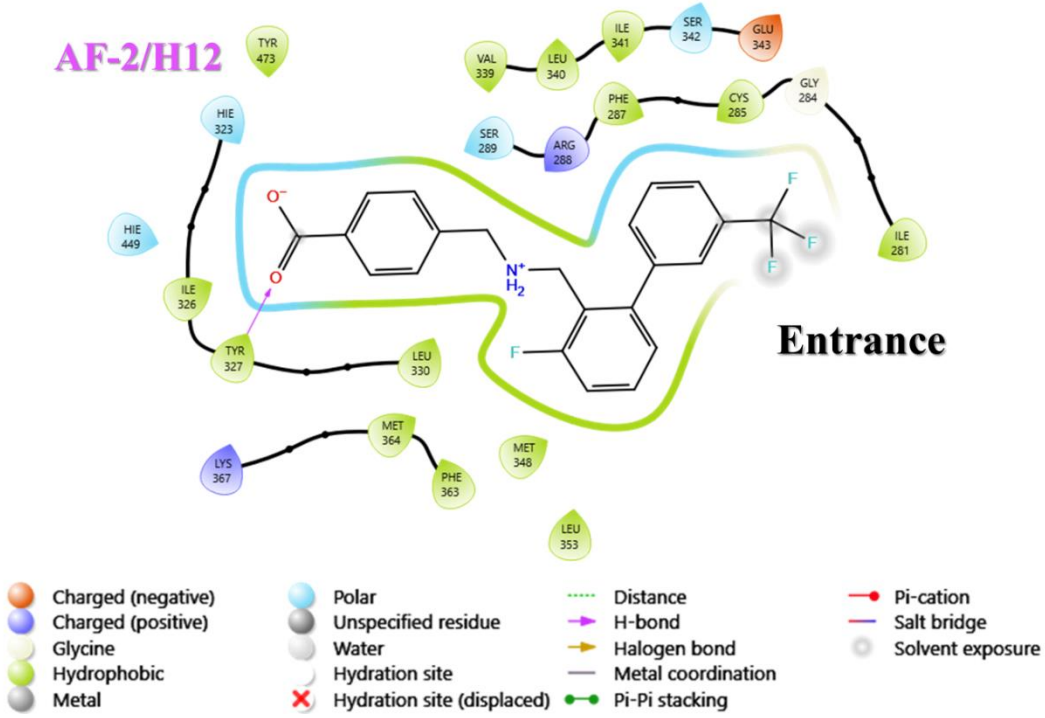

8D-2. AU-9 Modification 4 (Mod4) PPARα Predicted Binding Pose

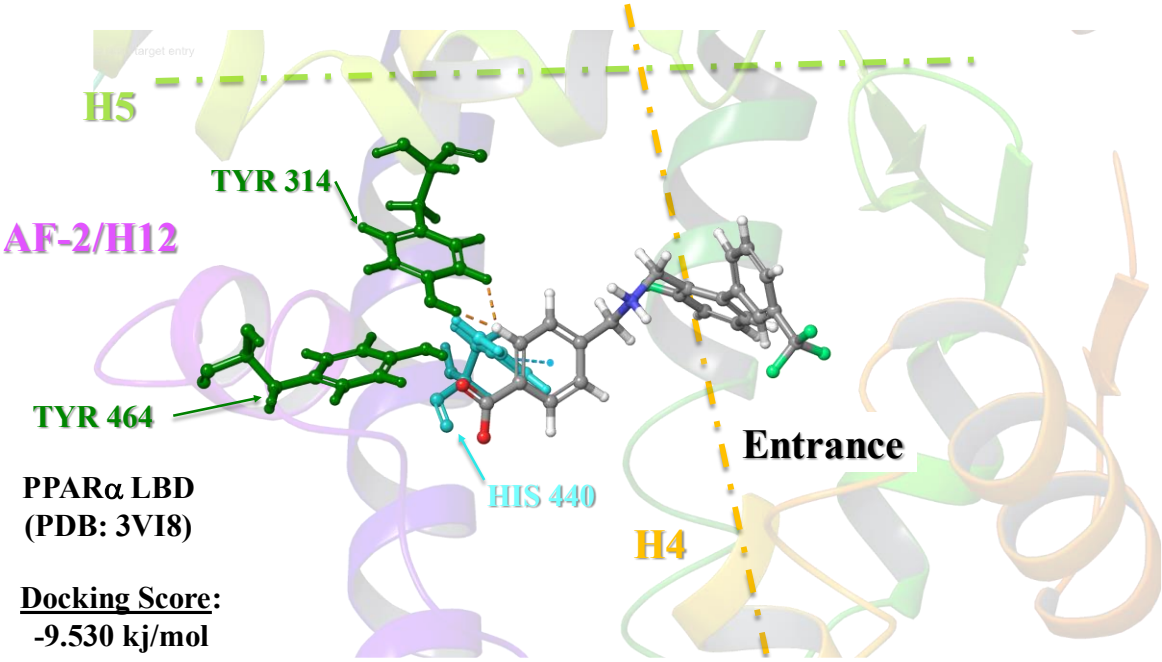

PPARα LBD
(PDB: 3VI8)

<u>Docking Score</u>:
-9.530 kj/mol

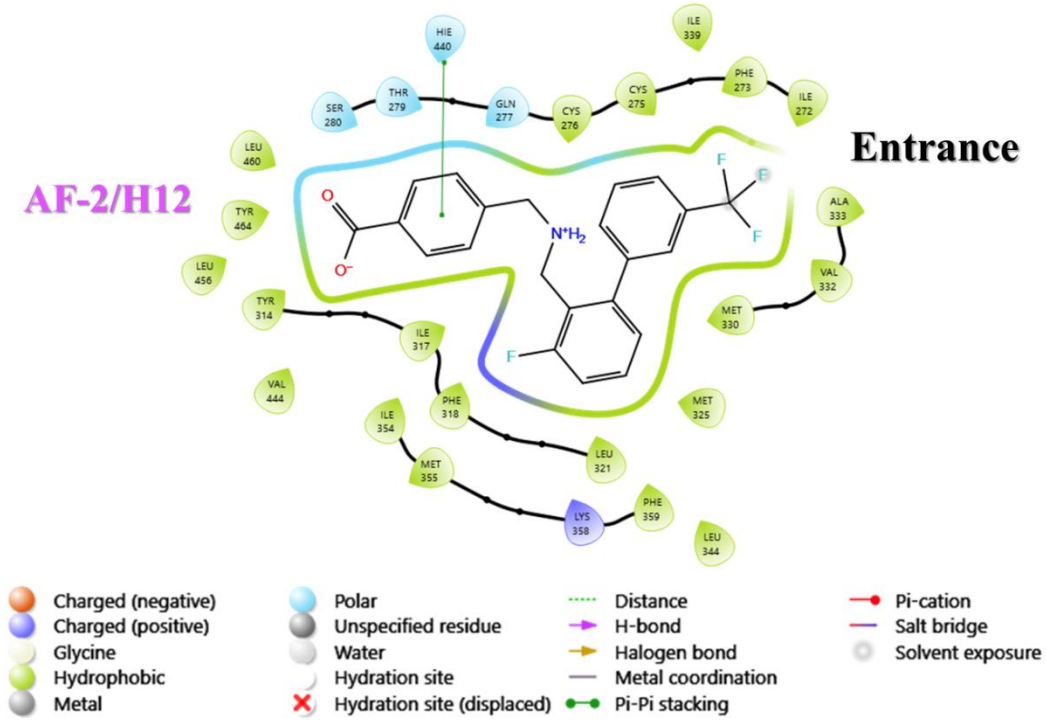

8D-3. AU-9 Modification 4 (Mod4) PPARδ Predicted Binding Pose

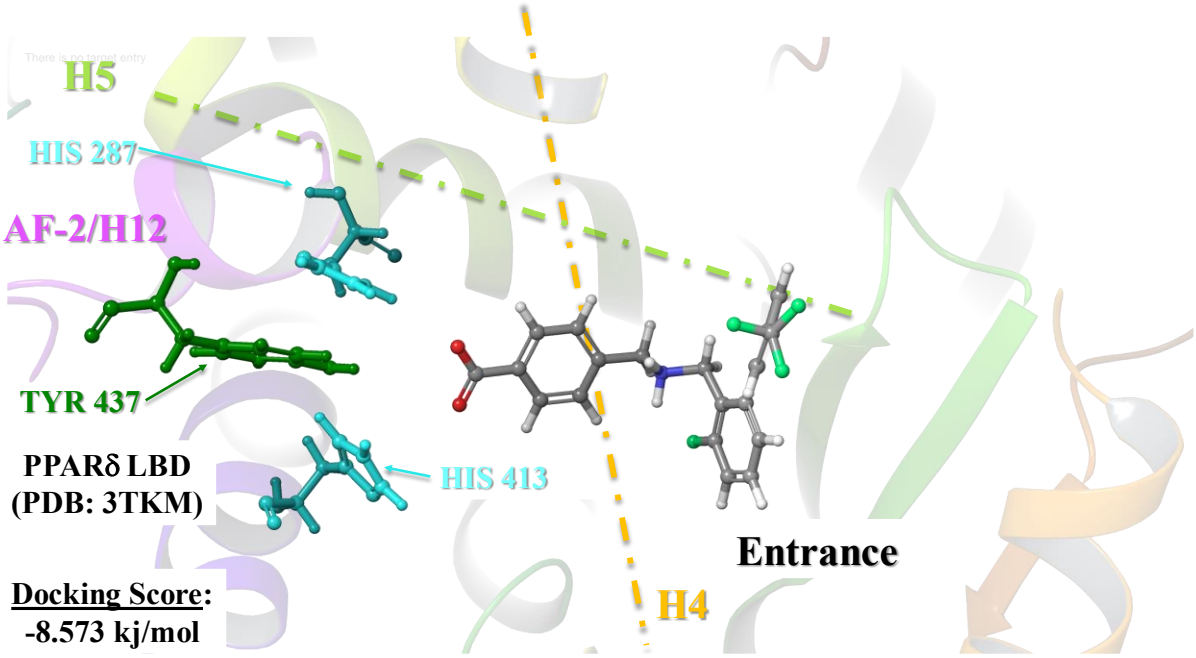

Docking Score:
-8.573 kj/mol

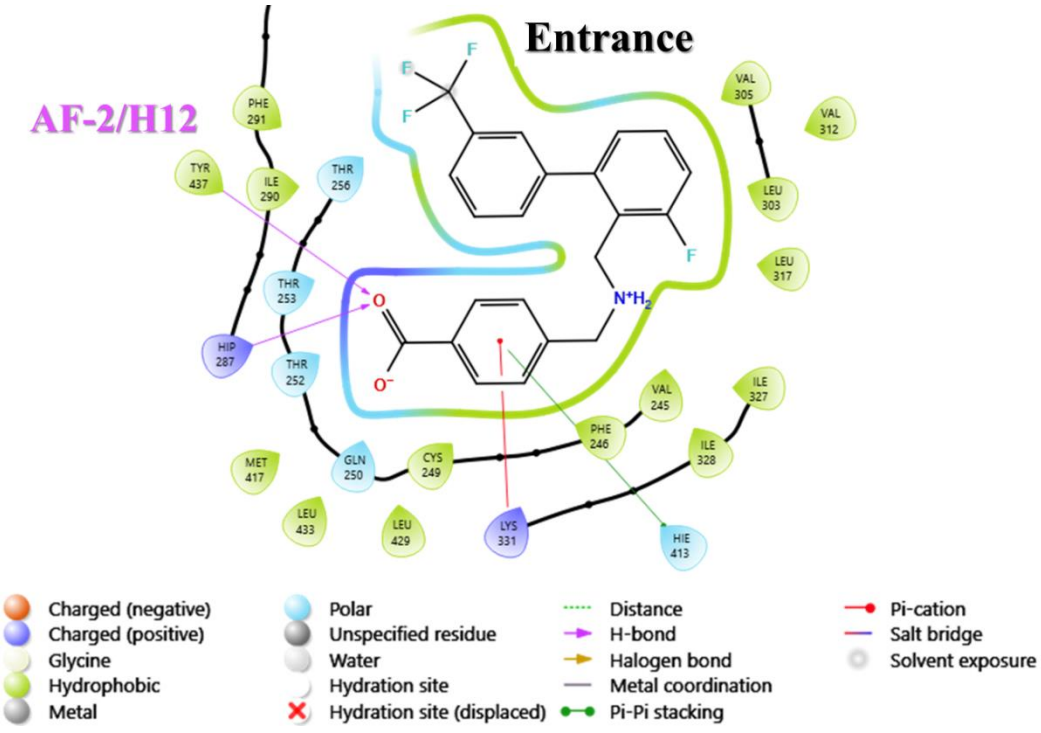

8D-1) Mod4 forms favorable contacts with the PPARγ AF-2 leading to an improved docking score over the other modifications.

8D-2) Mod4 conformationally aligns to the PPARα AF-2 like Mod3 with a modest increase in the docking score.

8D-3) Mod4 led to a loss of AF-2 contact at the PPARδ AF-2.

Table 2. QikProp and Docking Score Summary of AU-9 to Compound 7 (AU-403)

Structure	mol_MW	QPlogPo/w	QPPCaco	QPlogBB	QPPMDCK	Human Oral Absorption
AU-9	538.532	4.748	11.64	-0.149	104.557	1
Mod1	377.286	2.628	42.736	-0.005	448.473	2
Mod2	309.287	1.768	48.149	-0.229	115.374	3
Mod3	385.385	2.551	70.532	-0.019	121.612	3
Mod4	403.375	3.126	54.911	-0.18	141.272	3
AU-403	**403.375**	**2.748**	**74.741**	**0.08**	**198.16**	**3**

Structure	Docking Score PPARγ	Docking Score PPARα	Docking Score PPARδ
AU-9	-6.466	-6.229	-8.256
Mod1	-8.828	-9.473	-8.966
Mod2	-8.740	-9.710	-8.821
Mod3	-8.220	-9.894	-9.563
Mod4	-9.157	-9.530	-8.573
AU-403	**-7.163**	**-11.262**	**-11.358**

The structural optimization of AU-9 to AU-403 was guided by QikProp ADME predictions for BBB distribution and docking scores with each PPAR LBD. Favorable ligand contacts to the PPAR AF-2 are dominated by strong interactions that consequently increase docking scores. The AU-403 meta benzoic acid demonstrated a conformational bias that avoided the PPARγ AF-2 while maintaining strong interactions with PPARα and PPARδ.

2.2.4 In Silico PPAR SAR: Compound 7 (AU-403)

The benzoic acid active site moiety was moved to the meta position to improve the loss of PPARδ AF-2 contacts observed in Mod4. The predictive pose generated for compound 7 (AU-403) in the PPARγ LBD confirmed that the meta-substituted benzoic acid active site moiety did not form interactions with the AF-2 Tyrosine 473 residue. Consequently, an AU-403 dibenzylamine polar anchor point hydrogen bond to Cysteine 285 prevented further extension of the meta-benzoic acid into the AF-2, instead preferentially forming interactions with the AF-2 ancillary residues Tyrosine 327 and Lysine 367 (**Figure 9**.).

The predictive poses generated for AU-403 in the PPARα and PPARδ LBDs yielded overlapping results. It was observed that the AU-403 meta-benzoic acid adopted an inverse conformation to that of PPARγ, thus allowing favorable contact with the AF-2 Tyrosine residues. This observed conformational preference results from the AU-403 dibenzylamine nitrogen inversion, as the donor hydrogen bond to Cysteine interaction observed in PPARγ is absent in both the PPARα and PPARδ LBD predicted poses (**Figures 10 and 11**).

Figure 9. Predicted Binding Mode of Compound 7 (AU-403) in PPARγ LBD

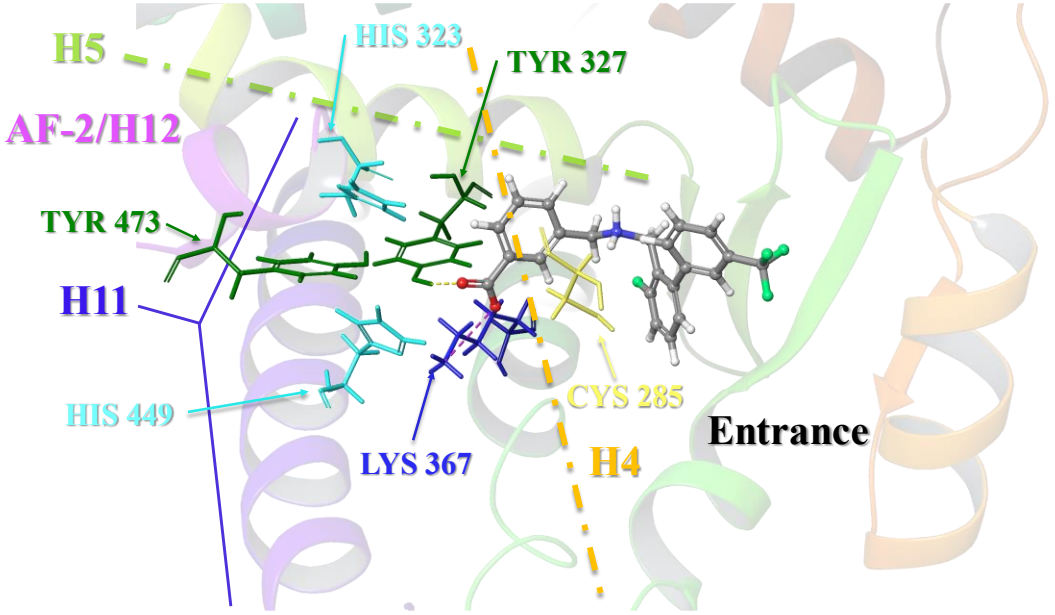

The aromatic Tyrosine 473 residue is a critical ligand contact site that regulates PPARγ AF-2 stability and coactivator/corepressor conformational bias. Additional supporting contacts from the basic Histidine 323 and 449 secure the AF-2 by clinching the H11 helix and H12/AF-2 during ligand-induced conformational flux. The AF-2 ligand access is coordinated by the Cysteine 285 residue to discern ligand conformational requirements and is more restrictive than PPARα and PPARδ. AU-403 displays a meta-substituted benzoic acid angled away from the Tyrosine 473 residue as the dibenzylamine contact with Cysteine 285 prevents further extension towards the AF-2. AU-403 forms a hydrogen bond with Tyrosine 327 and an ion-dipole contact with Lysine 367, enabling strong interactions with limited potential to stabilize the AF-2 for coactivator recruitment. Ligand docking poses were generated in the PDB: 5Y2O - Crystal structure of PPARgamma ligand binding-pioglitazone complex.

Figure 10. Predicted Binding Mode of Compound 7 (AU-403) in PPARα LBD

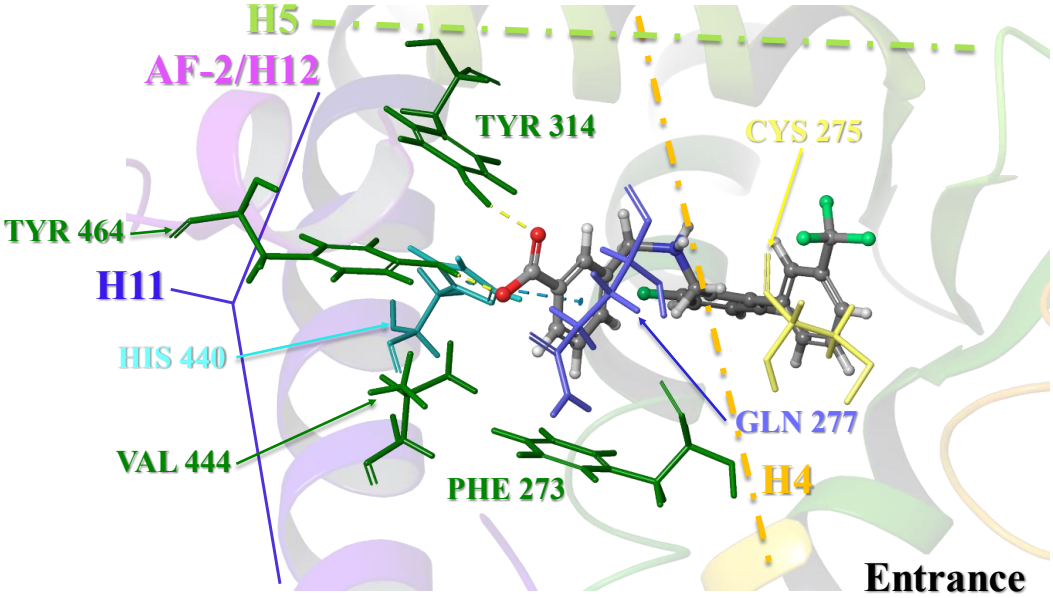

The aromatic Tyrosine 464 residue is the critical ligand contact site that regulates PPARα AF-2 stability and coactivator/corepressor conformational bias. Additional supporting contacts from the basic Histidine 440 and Histidine secure the AF-2 by clinching the H11 helix and H4 Helix during ligand-induced conformational flux. The Cysteine 275 residue is directed from the interior of the receptor site towards the entrance inverse to PPARγ conformational requirements. AU-403 displays a meta-substituted benzoic acid, which forms a hydrogen bond contact with Tyrosine 314, an aromatic hydrogen bond to Histidine 440, and an ion-dipole contact to the AF-2 Tyrosine 464, enabling strong interactions and good potential to stabilize the AF-2 for coactivator recruitment. Ligand docking poses were generated using the PDB: 3VI8 – Human PPAR alpha ligand binding domain in complex with a synthetic agonist APHM13 crystal structure.

Figure 11. Predicted Binding Mode of Compound 7 (AU-403) in PPARδ LBD

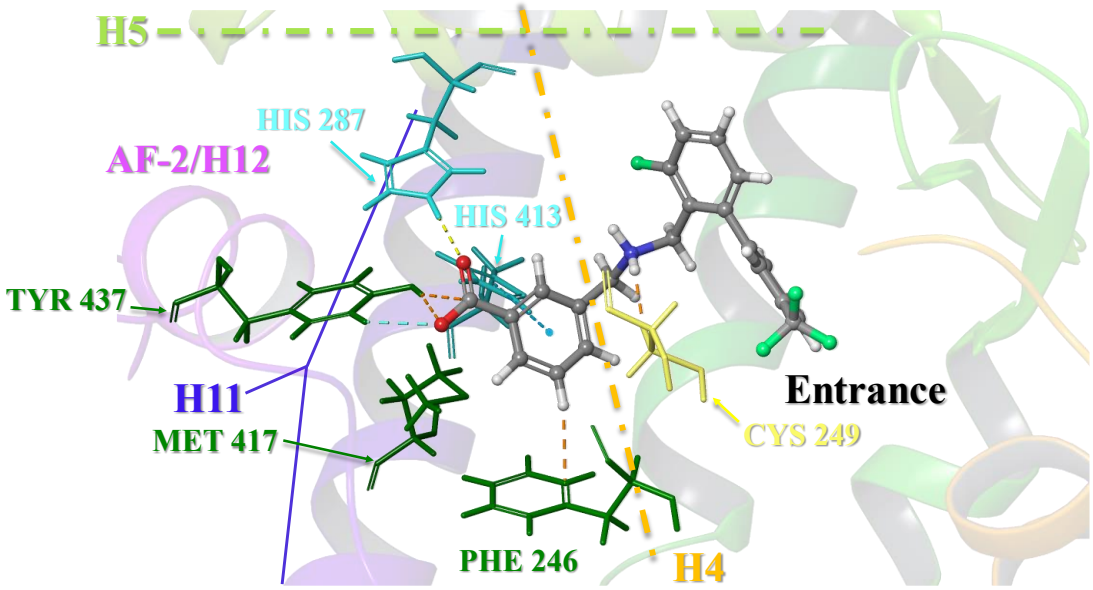

The aromatic Tyrosine 437 residue is the critical ligand contact site that regulates PPARδ AF-2 stability and coactivator/corepressor conformational bias. Additional supporting contacts from the basic Histidine 287 and 413 residues secure the AF-2 by clinching the H11 and H5 Helix during ligand-induced conformational flux. Like PPARα, the Cysteine 249 residue is directed from the interior of the receptor site towards the entrance as the ligand displaces the H4 Helix, conferring substrate overlap. In contrast to the other PPAR isoforms, the PPARδ AF-2 site contains hydrophobic residues that buffer Tyrosine 437, promoting the discernment of complementary ligand binding interactions. AU-403 displays a meta-substituted benzoic acid, which forms a hydrogen bond contact with Histidine 287 and aromatic hydrogen bonds with Tyrosine 437 and Histidine 413. When Phenylalanine 246 interacts with the hydrogen atom at position five on the benzene ring of the meta-substituted benzoic acid, it displaces the methyl group of Methionine 417 from the receptor site interior. When Phenylalanine 246 encounters the hydrogen atom located at position five on the benzene ring of the meta-substituted benzoic acid, it causes the methyl group of Methionine 417 to be displaced from the interior of the receptor site. This movement results in the sulfur atom shifting towards the ligand, causing disruption of intramolecular aromatic interactions with Tyrosine 437. This shift enables strong binding and has good potential to stabilize the AF-2 for coactivator recruitment. Ligand docking poses were generated using the PDB: 3TKM – Crystal structure PPAR delta binding GW-0742.

2.3 Synthetic Scheme for Compound 7 (AU-403)

The synthetic sequence described in **Figure 12.** started with a palladium (ii) acetate ($Pd(OAc)_2$) catalyzed Suzuki coupling between 2-bromo-6-fluorobenzaldehyde (**1**) and [3-(trifluoromethyl)phenyl]boronic acid (**2**) in a biphasic mixture of tetrahydrofuran (THF) and water using tetrabutylammonium bromide (TBAB) as a phase transfer catalyst to afford 3-fluoro-3'-(trifluoromethyl)-[1,1'-biphenyl]-2-carbaldehyde (**5**). Treatment of 3-(aminomethyl)benzoic acid (**3**) with thionyl chloride ($SOCl_2$) in the presence of anhydrous methanol (MeOH) to generate 3-(aminomethyl)benzoate hydrochloride salt which was neutralized in 1 M sodium hydroxide (NaOH) and extracted from with dichloromethane (DCM) to afford 3-(aminomethyl)benzoate (**4**). The condensation reaction between compounds **4** and **5** generates the imine intermediate in 1,2-dichloroethane (DCE), with subsequent reduction by sodium borohydride ($NaBH_4$) in MeOH to afford the secondary amine methyl 3-[{{[3-fluoro-3'(trifluoromethyl)-[1.1'-biphenyl]-2-yl]methyl}amino}methyl]benzoate (**6**). Final hydrolysis with aqueous NaOH in MeOH of 1c provided 3-[{{[3-fluoro-3'-(trifluoromethyl)-[1,1'-biphenyl]-2-yl]methyl}amino}methyl]benzoic acid (**7**).

Figure 12. Synthesis of PPARα/δ Dual Agonist Compound 7 (AU-403)

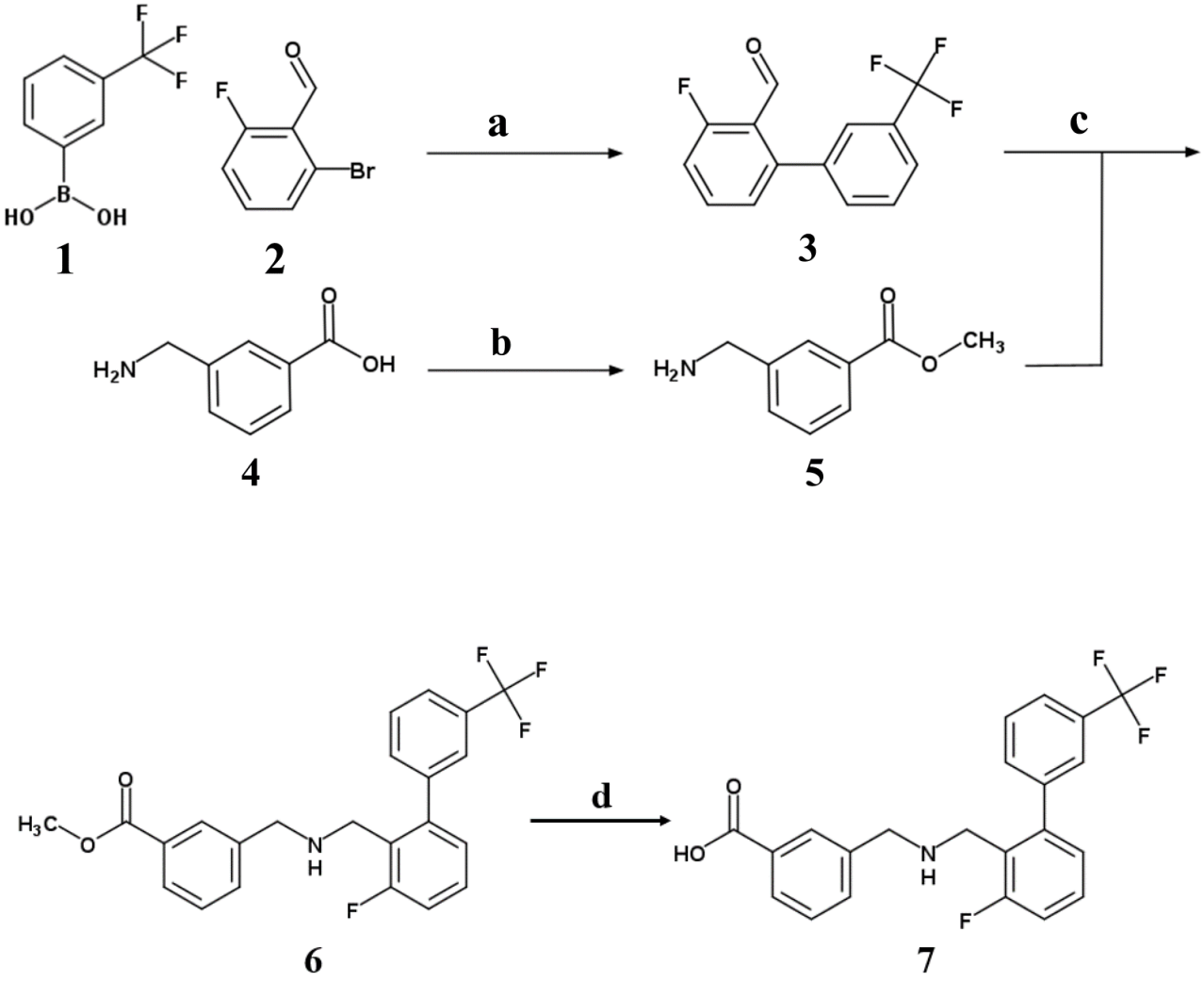

Reagents and conditions: (a) arylboronic acid, $Pd(OAc)_2$, TBAB, K_3PO_4, THF/H_2O (50 °C); (b) (aminomethyl)benzoic acid, $SOCl_2$, MeOH; (c) (i) (aminomethyl)benzoate, DCE; (ii) $NaBH_4$, MeOH (50 °C); (d) $NaOH{\cdot}H_2O$, MeOH.

2.4 In Vitro Evaluation of Compound 7 (AU-403): PPAR Transactivation

A transactivation assay is a powerful method for characterizing and functionally assessing how specific transcription factors or nuclear receptors regulate gene expression. This assay involves the attachment of a reporter gene to the target DNA promoter sequence for the nuclear receptor of interest to generate a DNA construct. This DNA construct is then inserted within a vector (e.g., plasmids, viral vectors, artificial chromosomes) capable of artificially carrying the foreign DNA into a cell where it can be replicated or expressed. Reporter genes are commonly used to highlight gene expression patterns, monitor gene expression and signaling pathways, and select cells expressing the reporter gene. Some examples of commonly used reporter genes include β-galactosidase, which turns a colorless substrate blue when cleaved, thus making gene expression patterns visible, green fluorescent protein (GFP), which produces green fluorescence, enabling real-time imaging of protein localization and dynamics within cells and tissues, firefly luciferase, which generates bioluminescent light when luciferin is oxidized, allowing luminescence-based assays for monitoring gene expression and signaling pathways, Renilla luciferase, similar to firefly luciferase but with different substrate specificity, enabling dual luciferase assays for internal normalization, and β-lactamase, which confers resistance to antibiotics, allowing selection of cells expressing the reporter gene.

The plasmid vector and an expression plasmid that encodes the nuclear receptor of interest are transfected into a suitable cell line, e.g., HEK-293. After treatment with compounds or stimuli that activate the nuclear receptor, the transcriptional activity is measured by quantifying the expression of the reporter gene. This is usually done using assays specific to the reporter gene, such as luciferase luminescence or fluorescence measurements. Transactivation assays are

essential for gaining insights into the function of nuclear receptors, screening for potential therapeutic compounds, and understanding gene regulation mechanisms that aid in drug discovery.

The precursors to compound 7 (AU-403), as well as subsequent derivatives, were evaluated for human PPAR in vitro potency and efficacy using a cell-based transactivation assay in HEK-293 cells transfected with a pGL3 luciferase reporter vector containing the respective target human-promoter PPAR recognition element (PPRE): hPPARα - acetyl-coenzyme A (acetyl-CoA), hPPARδ - PPARδ response element (DRE), hPPARγ - adipocyte protein 2 (AP2). Emax was measured relatively to a representative PPARα agonist fenofibrate (EC_{50} 30 uM), PPARδ agonist GW-0742 (EC_{50} 1.1 nM), and PPARγ partial agonist pioglitazone (EC_{50} 500 nM).

Optimization efforts to design AU-403 focused on incorporating a trifluoromethyl substituent to maintain weakly polar interactions in the ligand's hydrophobic tail, which was hypothesized to be a determinant factor in the PPARδ activation profile observed in the AU-9 predicted binding pose. Additionally, the bulkier para-benzoic acid in AU-9 was hypothesized to be a determinant factor in its attenuated activation of PPARγ. Therefore, the benzoic acid active site moiety was maintained in AU-403 to avoid PPARγ activation, with an alteration to the meta-substituted stereo isoform to selectively elicit PPARα and PPARδ activation.

The results from the transactivation activity in **Table 3.** demonstrate that AU-403 was able to achieve modest activation of PPARα relative to Fenofibrate while maintaining PPARδ potency relative to GW-0742, supporting the hypothesized chemical structural influences that confer the AU-9 PPAR activation profile. However, the indicated meta-substituted benzoic acid in AU-403 displayed minor PPARγ activity relative to pioglitazone, a partial agonist.

Table 3. Transactivation Activity: PPAR Nuclear Receptors Compound 7 (AU -403)

	hPPARα		hPPARδ		hPPARγ	
Compound	**EC_{50} (uM)**	**E_{max} (%)**	**EC_{50} (uM)**	**E_{max} (%)**	**EC_{50} (uM)**	**E_{max} (%)**
Compound 7	* 60	~ 50	* 0.0016	~ 70	* > 2	~ 25
Fenofibrate	30		1.47		1.06	
GW-0742	> 1		0.0011		> 1	
Pioglitazone	1				0.5	

E_{max} = maximum activation in percent of control compound. EC_{50} = reported values (Caymen Chemical). *Estimate of compound 4 EC_{50} based on % E_{max} of control compound. All E_{max} values were the average of three replicate samples.

2.5.1 Evaluation of compound 7 (AU-403) Physiochemical Properties: LogP and LogD

Physicochemical properties refer to a molecule's physical and chemical characteristics that determine its behavior and interactions in biological, chemical, and environmental systems. Understanding the physicochemical properties of molecules is essential to comprehend their structure, function, and activity in different contexts. This knowledge is crucial in drug discovery, as it helps predict and manipulate the behavior of substances to deliver a drug to the intended target tissue effectively.

LogP, or the logarithm of the partition coefficient, is a measure of a molecule's solubility in two immiscible solvents, typically octanol and water. The partition coefficient is defined as the ratio of the concentration of the molecule in the hydrophobic phase (octanol) to its concentration in the hydrophilic phase (water) at equilibrium. Thus, LogP indicates the likelihood that a compound will dissolve in a particular solvent, a critical criterion in early-stage drug discovery when evaluating the therapeutic application of a potential drug's distribution and absorption into a biological system. Generally, a higher partition coefficient indicates a greater tendency for a compound to dissolve in the hydrophobic phase, and a lower partition coefficient indicates a greater tendency to dissolve in the hydrophilic phase.

LogD, or the logarithm of the distribution coefficient, similarly measures a compound's lipophilicity by considering its ionization state at a given pH using a buffered aqueous phase. LogD is more effective than logP in evaluating subcellular localization or pH partitioning because it takes into account the ionization state of a molecule across a diverse range of pH environments within the biological system, spanning from acidic compartments like lysosomes (pH ~ 4.5-5) to pH conditions of the bloodstream (pH ~7.4) and more alkaline environments such as the small

intestine (pH ~6-8) or renal tubules (pH ~7.4-8). By considering pH-dependent ionization, LogD provides insights into both the lipophilicity of the neutral species and the impact of pH on solubility.

Determination of LogP and LogD provides values that affect various pharmacokinetic properties of a drug, such as its ability to dissolve, be absorbed by the body, distribute throughout the body, undergo metabolism, and be excreted (ADME). A drug with a high LogP value, which indicates high lipophilicity, can have better absorption through cell membranes. However, it can also experience slower clearance and longer half-life due to its affinity for lipid-based environments. As a result, this can lead to non-specific binding, accumulation in fatty tissues, and limited aqueous solubility, ultimately reducing its effectiveness. On the other hand, a drug with a lower LogP value, characterized by greater hydrophilicity, may exhibit faster clearance, shorter half-life, and better aqueous solubility, leading to enhanced bioavailability. While low LogP drugs may have limited penetration into cell membranes and tissues, they are less prone to off-target accumulation, resulting in more specific and predictable pharmacological effects. Nevertheless, the ultimate effectiveness of each drug is impacted by various factors beyond LogP, including target specificity, mechanism of action, dose regimen, and individual patient characteristics.

There has yet to be an FDA-approved PPARδ agonist, and based on the inherent hydrophobicity of the PPARδ LBD, this is likely a result of drug designs that maximize tight ligand binding via entropically favored hydrophobic displacement of water from the receptor site. This is further aggregated by ligand polar anchor points frequently consisting of lipophilic ethers, thioethers, and aliphatic carboxylic acids. Yet there are numerous FDA-approved PPARα agonists consisting of the fibrate class of drugs, PPARγ agonists consisting of the TZD-glitazone class of drugs, and more recently PPARα/γ dual agonists consisting of the glitazar class of drugs.

Therefore, the drug design of AU-403 focused specifically on sustaining physiochemical characteristics that allowed the ligand to maintain strong interactions coinciding with an ADME profile intended for oral delivery to the CNS.

The results from the PPAR transactivation assays demonstrated promising potential for AU-403 as a first-in-class PPARα/δ agonist, requiring further exploration as a therapeutic candidate for preclinical development for AD. LogP and LogD studies for AU-403 were carried out against a set of representative PPAR and LXR agonists. These comparison agonists were chosen based on their toxicity profile and to evaluate potential physiochemical properties indicating a major drawback toward clinical application.

LogP and LogD values were determined for AU-403 compared as a free drug to the PPARγ agonist rosiglitazone maleate salt formulation, PPARα agonist fenofibrate (prodrug), PPARδ agonist GW-0742 free drug, LXR pan agonist T0901317 free drug, and the LXR pan agonist GW3965 as a hydrochloride salt (**Table 4.**). LogP values were determined using a two-to-one v/v octanol to neutral water. LogD values were determined using a salt-free aqueous citrate buffer pH of 4 and an aqueous phosphate-buffered saline (PBS) pH of 7.4, representing the stomach's acidic nature and the blood's physiological conditions. A drug intended for oral delivery should have sufficient solubility in the gastrointestinal fluids to facilitate dissolution and absorption. Ideally, the drug should be moderately to freely soluble in water to ensure efficient absorption as it exits the stomach's acidic environment, pH 1.5-3.5, and encounters the more alkaline environment of the duodenum and small intestine, pH 6 - 8.

PPAR Agonist Physiochemical Properties Evaluation of LogP and LogD

As a free drug, compound 7 (AU-403) displays comparable aqueous solubility to rosiglitazone maleate, a clinically approved formulation, with LogD values of 1.23 and 1.66 at a pH of 4 and 7.4, respectively. Maleic acid, which forms maleate salts when neutralized with a base, can improve the solubility and stability of certain drugs, enhancing their bioavailability. As might be expected, the rosiglitazone maleate salt formulation improved aqueous solubility in a pH-buffered environment, indicated by ideal LogD values of 1.67 and 1.66, and had decreased aqueous solubility in neutral water and decreased solubility in ethanol indicative of the salt formulation.

The fenofibrate prodrug form requires formulation for adequate oral bioavailability as the isopropyl ester dramatically decreases aqueous solubility, demonstrated by LogP and LogD values of 4.8 and > 5 at pHs of 4 and 7.4. As a result, fenofibrate is commonly formulated and administered in the micronized form (Antara), nanoparticle tablets (Tricor), and in the active form as a choline salt of fenofibric acid (Trilipix).

The GW-0742 phenoxy acetic acid has an approximate pKa of 4.8 and displayed an acceptable LogD of 3.24 when exposed to a citrate buffer at a pH of 4. However, the LogD increased to > 5 when exposed to phosphate-buffered saline (PBS) at a pH of 7.4 and a LogP of 6.57 in neutral water. These results suggest that the phenoxyacetic acid is practically insoluble when exposed to neutral water and a PBS-balanced salt solution, which may lead to subcellular localization, e.g., lysosomes. Consequently, GW-0742 would require further formulation for adequate bioavailability, demonstrating potential toxicity associated with its failure to reach human clinical trials.

LXR Agonist Physiochemical Properties Evaluation of LogP and LogD

The LXR pan agonist T0901317 displays LogP and LogD values > 4, consistent with what should be expected without an ionizable functional group. While T0901317 has shown promise in preclinical models for various potential therapeutic applications, including metabolic disorders, cardiovascular diseases, and cancer, its translation into human clinical trials has not been approved. The toxicities that prevent clinical advancement of T0901317 are generally associated with LXR-induced hepatotoxicity; however, LogP and LogD values suggest inherent toxicity associated with its deposition into off-target tissues.

GW3965 is another LXR pan agonist primarily studied in preclinical research rather than clinical trials. Similar to T0901317, GW3965 was valued as a promising therapeutic application for metabolic disorders such as dyslipidemia, atherosclerosis, and Type 2 diabetes. This is largely attributed to its apparent LXRβ selectivity, thus limiting LXRα-associated toxicities. However, the calculated LogP and LogD values of 8.2, 5.34, and 4.9 would suggest that GW3965 is equally likely to display toxicities, as observed with T0901317. While GW3965 and other LXR agonists hold promise for various clinical applications based on preclinical data, further research, including clinical trials, would be needed to evaluate their safety, efficacy, and potential side effects in human subjects. Additionally, challenges such as off-target effects, pharmacokinetic properties, and patient selection criteria will need to be addressed to realize the clinical potential of these compounds.

Table 4. Results PPAR and LXR Agonist Partition Coefficients: Octanol and Water

	$LogP_{o/w}$	$LogD_{o/w}^{pH=4}$	$LogD_{o/w}^{pH=7.4}$	Solubility in DMSO (mg/mL)	Solubility in Ethanol (mg/mL)
Compound 7	0.78	1.23	1.66	35	28
Rosiglitazone (PPARγ)	2.56	1.67	1.66	34	1
Fenofibrate (PPARα)	4.80	5.01	5.01	15	1
GW-0742 (PPARδ)	6.57	3.24	5.00	25	10
T0901317 (LXRα)	4.82	4.10	4.09	100	50
GW3965 (LXRβ)	8.20	5.34	4.90	20	2

According to 'Lipinski's Rule of 5' (developed at Pfizer), the logP of a compound intended for oral administration should be <5. Drug logP values approaching 5 and above indicate compromising bioavailability. Therefore, adequate drug concentrations cannot be reached or maintained to achieve the desired therapeutic effect. Additionally, lipophilic drugs may deposit in fatty tissue and, thus, are challenging to excrete, leading to the drug's bioaccumulation that will impact systemic toxicity. A drug targeting the central nervous system (CNS) should ideally have an approximate logP value of 2. For oral and intestinal absorption, the ideal logP value is between 1.35 and 1.8. Samples were run in triplicate, and the average value was reported. The pH of buffered aqueous phases was made to assess solubility across a range of physiologically relevant settings.

2.5.2 Evaluation of Compound 7 (AU-403) Physiochemical Properties: Parallel Artificial Membrane Permeability Assay (PAMPA)

The Parallel Artificial Membrane Permeability Assay (PAMPA) is an in vitro technique used in drug discovery and development to predict the passive permeability of drug candidates across biological membranes, particularly the blood-brain barrier (BBB) and gastrointestinal (GI) tract epithelium. In PAMPA, a synthetic lipid membrane is sandwiched between two aqueous compartments, simulating the lipid bilayer structure of biological membranes. The drug candidate is introduced to the donor compartment, and its passive diffusion across the lipid membrane into the acceptor compartment is measured. By quantifying the drug permeation rate, PAMPA provides information on the compound's membrane permeability properties, including its ability to cross biological barriers.

However, it has some limitations that need to be considered. For example, PAMPA is less biologically complex compared to in vivo systems. Thus, it has limited predictive accuracy for in vivo permeability and cannot model active transport mechanisms. PAMPA also has variability in membrane composition between setups and a limited dynamic range for compounds with extreme permeability properties. Despite these limitations, PAMPA is still a valuable tool in drug development to screen and prioritize lead compounds based on their membrane permeability characteristics.

A 4% Lecithin in dodecane solution was used due to its ability to form a lipid bilayer that closely mimics biological membranes. As a naturally occurring mixture of phospholipids, lecithin contains phosphatidylcholine, a major component of cell membranes, e.g., intestinal epithelium. This composition allows lecithin to create an artificial membrane with properties similar to those

of biological membranes, including fluidity and barrier function. Additionally, lecithin is readily available, stable, and easy to handle, making it a practical choice for laboratory assays. While other lipid mixtures or synthetic membranes could be used in PAMPA assays, lecithin is often preferred due to its biocompatibility and ability to simulate cellular membrane environments accurately.

This method offers a cost-effective and rapid alternative to cell-based permeability assays, allowing a quick, efficient determination of a compound's ability to cross membranes passively. The BioAssay Systems' PAMPA-096 Kit contains all the necessary components to conduct an assay to evaluate gastrointestinal (GI) membrane permeability. The protocol involves preparing donor and acceptor plates, assembling PAMPA filters, and incubating test compounds for passive diffusion across the artificial membrane. Samples were then collected from the apical (A) side and measured by UV absorbance to determine the change in concentration in response to passive diffusion into the basolateral side (B) over time. The obtained data was used to calculate the apparent permeability rate (Papp), measured in cm/sec, and assess the membrane permeability of compound 7 (AU-403) compared to the low permeability standard, medium permeability standard, and high permeability standard provided in the BioAssay kit (Chemical identities were not disclosed by the manufacturer).

The AU-403 chemical structure is a zwitterion at physiological pH containing a positively charged dibenzylamine (conjugate acid) and a negatively charged benzoate (conjugate base), resulting in an overall neutral charge. The LogD value of 1.66 indicates that AU-403 prefers the lipid phase approximately forty-seven times more than the aqueous phase, suggesting balanced lipophilic characteristics. This balance between hydrophilic and lipophilic properties is critical to predict potential pharmacokinetic behavioral influences, including ADME. Despite ideal lipophilic characteristics, the overall neutral charge of the AU-403 zwitterion could hinder its

ability to efficiently cross biological membranes, potentially leading to poor absorption and distribution to target tissues.

The PAMPA results revealed that AU-403, a zwitterionic compound, exhibited approximately three-fold higher permeability than the high permeability standard provided in the kit (**Table 5.**). This notable increase suggests that AU-403 possesses enhanced membrane permeability characteristics, potentially attributed to its zwitterionic functionality. The neutral charge of the zwitterion may facilitate favorable interactions with both hydrophilic and lipophilic regions of the artificial lipid membrane, promoting efficient passage through the membrane barrier. These findings underscore the importance of considering the zwitterionic nature of AU-403 in its pharmacokinetic behavior and drug disposition, highlighting its potential for improved membrane permeation and bioavailability in biological systems.

Table 5. PAMPA Gastrointestinal (GI) Membrane Permeability

Compound	Mean P_{app} (10^{-6} cm/s)
	A to B
*Low Permeability Std.	0.6
*Medium Permeability Std.	2.2
*High Permeability Std.	5.2
Compound 7	14.4

All compounds were evaluated at the same dose (500 uM) based on the manufacturer's instructions (BioAssay Systems). Values are based on cm/sec.* Permeability standards were provided in the kit.

2.5.3 Evaluation of Compound 7 (AU-403) Physiochemical Properties: Caco-2 PAMPA

Caco-2 human epithelial cells derived from a human colon adenocarcinoma are commonly used to study drug absorption and transport in the intestine. When these cells are grown on a permeable membrane filter, they spontaneously differentiate into a layer of polarized cells that resemble the epithelial lining of the small intestine. This model system replicates crucial characteristics of the intestinal epithelium, such as tight junctions, brush border enzymes, and transporter proteins.

While traditional PAMPA focuses on passive permeability across a lipid bilayer, Caco-2 PAMPA assays consider both passive and active mechanisms involved in drug transport across the intestinal epithelium. Therefore, while traditional PAMPA provides valuable information on a compound's passive permeability properties, Caco-2 PAMPA offers a more comprehensive understanding of its behavior in a biologically relevant context, providing a more accurate prediction of oral absorption and bioavailability.

Nadolol, Metoprolol, and Digoxin were used as standards for comparison with AU-403 in the Caco-2 PAMPA assay. Nadolol, a non-selective beta-blocker, exhibits high hydrophilicity and low passive permeability, serving as a reference compound for evaluating substances with similar characteristics. Metoprolol, a selective beta-1 adrenergic receptor antagonist, demonstrates moderate lipophilicity and permeability, making it suitable for assessing compounds with intermediate permeability levels. Digoxin, a cardiac glycoside, is highly polar and undergoes active transport mediated by P-glycoprotein (P-gp) in the intestine, making it a reference compound for evaluating substances susceptible to efflux transporter interactions.

The Caco-2 PAMPA assay results for compound 7 (AU-403) demonstrated distinct permeability behavior compared to the reference compounds, as evidenced by the Papp, efflux ratio, and mean % solution recovery (**Table 6.**). Papp values measure the extrinsic properties of a molecule and are more accurate when compared to reference drugs with an established pharmacokinetic profile. These results demonstrated that AU-403 exhibited a greater Papp than nadolol and digoxin, with values of 24.0 x 10^{-6} cm/s (A to B) and 17.3 x 10^{-6} cm/s (B to A), respectively. This suggests a greater ability of AU-403 to traverse the Caco-2 cell monolayer in the apical to basolateral (A to B) direction than the reverse basolateral to apical (B to A) direction. In contrast to the P-gp substrate digoxin, which displayed a pronounced efflux ratio of 330, indicative of active efflux transport (B to A), AU-403 exhibited a notably lower efflux ratio of 0.720. This suggests minimal involvement of efflux transporters in the cellular disposition of AU-403. Additionally, AU-403 demonstrated lower mean % solution recovery rates than the reference compounds, particularly in the A to B direction (77.1%). This may suggest increased cellular uptake or metabolism of AU-403 within the Caco-2 cells, impacting its overall permeability measurements.

The results obtained from both the passive diffusion PAMPA and Caco-2 PAMPA assays confirm AU-403's robust permeability characteristics. In the Caco-2 PAMPA assay, AU-403 was determined to be either a poor or non-efflux transporter substrate. This consistency across different assay platforms increased confidence in AU-403's passive permeability profile and highlighted its suitability for further development as a drug candidate for AD.

Table 6. Caco-2 PAMPA Result for Compound 7 (AU-403)

Compound	Mean P_{app} (10^{-6} cm/s)		Efflux Ratio	Mean %Solution Recovery		Rank	
	A to B	B to A		A to B	B to A	P_{app}	Efflux Transporter Substrate
Nadolol	0.0144	ND	-	89.7	ND	Low	-
Metoprolol	23.2	ND	-	91.3	ND	High	-
Digoxin	0.0543	17.9	330	85.6	93.0	Low	Likely
7	24.0	17.3	0.720	77.1	93.0	High	Poor or non-

ND means not determined. Binning Criteria*: Low permeability: Papp ≤ 0.600 (×10-6 cm/s), Moderate permeability: 0.600 < Papp < 6.00 (× 10-6 cm/s), High permeability: Papp ≥ 6.00 (×10-6 cm/s).*The binning criteria of permeability are proposed based on CB routine Caco-2 permeability assay conditions (2.00 μM dosing concentration and 120 minutes incubation). The boundaries for low and high permeability binning are equivalent to 50.0% and 85.0% of the "calculated Fa" in human. Substrate Potential**: likely: Era ≥ 2.00, Poor or non: ERa < 2.00.

2.5.4 Evaluation of Compound 7 (AU-403) Physiochemical Properties: MDCKII-MDR1 PAMPA

The MDR1 gene, also known as ABCB1 or multidrug resistance protein 1 (MDR1), produces the P-glycoprotein (P-gp) found in cell membranes. P-gp is part of a group of ATP-binding cassette transporters and acts as an efflux pump to move substances out of cells. These substances include chemotherapy drugs, antibiotics, antivirals, and many other medications. The abundance of MDR1/P-gp in various tissues such as the BBB, intestines, liver, and kidneys is vital in determining how drugs are absorbed, distributed, metabolized, and excreted (ADME). Changes in the function of P-gp, which can result from mutations or alterations in the MDR1 gene, can impact drug disposition and contribute to multidrug resistance in cancer chemotherapy and other treatments.

The BBB poses a significant challenge in delivering drugs to the CNS due to the abundance of efflux transporters such as P-gp. In vitro assays using cell lines that overexpress the P-gp MDR1, such as the Madin-Darby Canine Kidney II (MDCKII)-MDR1 cell line, are valuable tools for evaluating the permeability of compounds across the BBB. These cell-based models mimic the expression of MDR1 at the BBB, enabling researchers to assess the likelihood of efflux-mediated transport and predict CNS penetration in vivo. The MDCKII-MDR1 cell line is a reliable platform for investigating the interaction between potential drug candidates and MDR1, providing insights into the ability of the compounds to overcome efflux barriers and achieve therapeutic concentrations in the CNS across the BBB.

The results from the MDCKII-MDR1 PAMPA assay for AU-403 showed that Nadolol had a Papp of 0.137 x 10^{-6} cm/s in the A to B direction, while Metoprolol showed a Papp of 21.1 x 10

$^{-6}$ cm/s in the same direction (**Table 7.**). Digoxin had a Papp of 0.299 x 10^{-6} cm/s from A to B and 6.97 x 10^{-6} cm/s from B to A, resulting in an efflux ratio of 23.3. In comparison, AU-403 had a Papp of 26.8 x 10^{-6} cm/s from A to B and 17.2 x 10^{-6} cm/s from B to A, with an efflux ratio of 0.642. Digoxin's mean % solution recovery was 82.5% from A to B and 97% from B to A, while for AU-403, the mean % solution recovery was 89.5% from A to B and 90.7% from B to A.

The results of the MDCKII-MDR1 PAMPA assay for AU-403 have shown interesting permeability characteristics when compared to reference compounds. Nadolol, known to have low permeability, had minimal passive permeability with a low Papp value in the A to B direction. In contrast, Metoprolol exhibited moderate permeability, with a Papp value falling between nadolol and AU-403. Digoxin, a substrate of the P-gp efflux transporter, showed significant efflux-mediated transport, as evidenced by its high efflux ratio. Interestingly, AU-403 demonstrated notably higher permeability in both directions than the reference compounds, comparable to the results from the Caco-2 PAMPA assay. The efflux ratio for AU-403 was substantially lower than digoxin's in both active transport PAMPA assays, further validating that it is a poor or non-substrate for P-gp efflux transporters. Overall, these results offer valuable insights into the physiochemical profile of AU-403 and its potential implications for BBB permeation in the context of AD.

Table 7. MDCKII-MDR1 PAMPA Result for Compound 7 (AU-403)

Compound	Mean P_{app} (10^{-6} cm/s)		Efflux Ratio	Mean %Solution Recovery		Rank
	A to B	B to A		A to B	B to A	P_{app}
Nadolol	0.137	ND	-	85.7	ND	Low
Metoprolol	21.1	ND	-	87.4	ND	High
Digoxin	0.299	6.97	23.3	82.5	97.0	Low
7	26.8	17.2	0.642	89.5	90.7	High

ND means not determined. The in vitro cell based models are more appropriate for passively transported compounds and the efflux phenomena might complicate the permeability result. And the permeability results for compounds with efflux phenomena should be interpreted in combination with the application conditions. Binning Criteria*: Low permeability: Papp ≤ 1.0 (×10-6 cm/s), Moderate permeability: 1.0 < Papp < 8.0 (×10-6 cm/s), High permeability: Papp ≥ 8.0 (×10-6 cm/s.). *The boundaries for low and high permeability binning are equivalent to 50% and 85% of the "calculated Fa" in human. Please notice the binning criteria is proposed based on WuXi's routine MDR1-MDCK II permeability assay (test conc.of 2 μM, 2.5 hours incubation).

2.6.1 In Vitro Functional Activity: 3T3-L1 Adipocyte Differentiation Lipotoxicity Assessment of Compound 7 (AU-403)

3T3-L1 cells are a type of fibroblast-like cell line derived from mouse embryos. They are commonly used as an in vitro model for studying adipocyte biology, particularly adipogenesis, the process by which precursor cells differentiate into mature adipocytes or fat cells. These cells are widely utilized in research focused on understanding the molecular mechanisms underlying adipocyte differentiation, lipid metabolism, insulin sensitivity, and obesity-related disorders. Additionally, 3T3-L1 cells investigate the pharmacological effects of various compounds, such as drugs and natural compounds, on adipocyte differentiation and lipid accumulation in the context of toxicity.

Drugs like rosiglitazone facilitate PPARγ activation, which is crucial for adipocyte differentiation and plays a central role in lipid metabolism and insulin sensitivity. However, excessive PPARγ activation, as seen with rosiglitazone, can lead to lipid-induced toxicity, particularly in the context of adipocyte differentiation in models like 3T3-L1 cells. While rosiglitazone promotes adipocyte differentiation and enhances lipid uptake and storage within adipocytes, which can be beneficial for managing insulin resistance and diabetes, prolonged exposure to rosiglitazone can lead to adverse effects, e.g., weight gain, edema, and inflammation.

One significant concern is the excessive accumulation of lipids within adipocytes, leading to adipocyte hypertrophy and dysfunction. This dysregulated lipid metabolism can trigger a cascade of events, including releasing pro-inflammatory cytokines and adipokines, ultimately contributing to chronic low-grade inflammation, insulin resistance, and metabolic syndrome. Moreover, rosiglitazone-induced activation of PPARγ can alter gene expression profiles in

adipocytes and other tissues, such as the liver and skeletal muscle. This can disrupt systemic lipid metabolism, leading to toxic ectopic lipid deposition, hepatic steatosis, and skeletal muscle insulin resistance, further exacerbating metabolic disturbances.

While rosiglitazone can be therapeutically beneficial for managing insulin resistance and diabetes, balancing its activation to avoid lipid-induced toxicity and associated metabolic complications is crucial. This highlights the importance of understanding the nuanced effects of PPARγ modulation in adipocyte differentiation and lipid metabolism to mitigate adverse effects and optimize therapeutic outcomes.

The process of differentiating 3T3-L1 cells into adipocytes closely resembles the natural process of adipogenesis. First, the cells are cultured in a growth medium to allow for proliferation and preparation for differentiation until they reach confluence. Then, the induction phase begins by replacing the growth medium with a specialized differentiation medium containing insulin, dexamethasone, and a synthetic PPARγ agonist, i.e., rosiglitazone. These pharmaceutical agents activate distinct pathways involved in adipocyte differentiation, including glucose uptake, lipid synthesis, and PPAR signaling. Upon activation, PPARγ forms heterodimers with retinoid X receptors (RXRs), and together, they bind to PPREs in the promoter region of the AP2 target gene. Activation of the PPARγ pathway leads to the transcriptional activation of adipogenic genes, including those encoding adipocyte-specific proteins such as adiponectin, fatty acid binding protein 4, and lipoprotein lipase.

Over a few days, the cells undergo morphological changes, transitioning from a fibroblastic to a round shape, and gather lipid droplets typical of mature adipocytes. At the end of the experiment, the differentiated 3T3-L1 mature adipocytes are stained with Oil Red O. Oil Red O is a lysochrome (fat-soluble) diazo dye commonly used for staining, visualizing and quantifying

neutral triglycerides and lipids in cells or tissues, particularly in adipocyte differentiation assays such as those using 3T3-L1 cells. After staining with Oil Red O, the lipid droplets appear as red-stained structures against a background of unstained cells.

The quantification of Oil Red O staining is a straightforward process that involves destaining the stained cells or tissues with isopropanol or another suitable solvent to solubilize the Oil Red O dye. The resulting solution is then transferred to a microplate. The solution's optical density (OD) is measured spectrophotometrically at 510 nm, corresponding to the absorption peak of Oil Red O. The OD measurement indirectly measures the amount of lipid accumulation in the sample, with higher OD values indicating greater lipid content based on the dissolution of Oil Red O.

Oil Red O staining was quantified by comparing the OD values of the stained treatment samples to those of the known lipid standard rosiglitazone and an untreated control sample. The results in **Figure 13.** predictably show a significant increase in lipid accumulation with the rosiglitazone-positive control. The PPARα agonist fenofibrate and PPARδ agonist GW-0742 treatment groups had no significant effect on the induction of lipids relative to the untreated control, indicating either a lack of specificity for PPARγ or differential transcriptional regulation associated with PPARγ target genes. In comparison, compound 7 (AU-403) had only a minimal increase in lipid induction. However, the difference between the no-treatment and positive control was insignificant. In combination with supporting results from the PPAR transactivation assays, AU-403 displays minor activation of PPARγ. This attenuated response, combined with a promising physiochemical ADME profile, further strengthens the potential of AU-403 as a viable option in AD-related patients.

Figure 13. PPARγ Mediated Adipocyte Differentiation in 3T3-L1 Fibroblasts

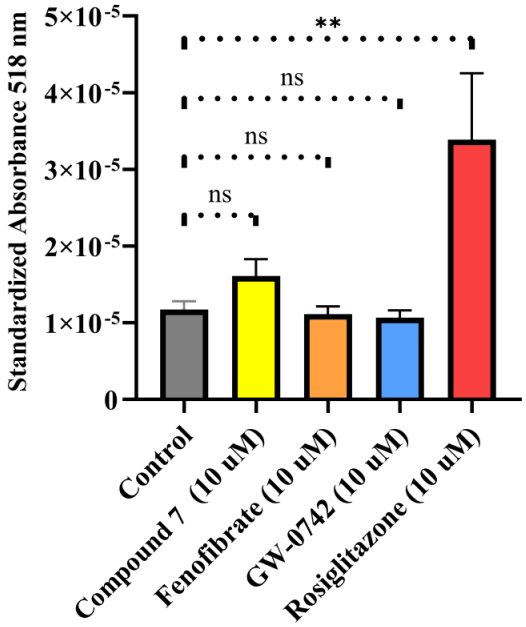

Values were determined spectrophotometrically by standardizing the absorbance measurement of the oil red O stain at 510 nm to that of a DAPI stain at Ex 358/ Em 461. All values were obtained from eight replicate samples at a drug concentration of 10 uM. A repeated measures One-Way ANOVA was used to compare treatment groups. A Dunnett's multiple comparisons test was used to determine significance compared against the control group. ns = not significant. ** = 0.003.

2.6.2 In Vitro Functional Activity: Hepatic (HepG2) Lipotoxicity Assessment of Compound 7 (AU-403)

HepG2 cells are a type of human liver cancer cells that were first obtained from a 15-year-old male with a well-differentiated hepatocellular carcinoma. They are frequently used in laboratory studies as an in vitro model to investigate various liver-related conditions, such as drug metabolism, liver physiology, viral hepatitis, and hepatic lipid metabolism. These cells possess several characteristics of normal liver cells, making them a valuable tool for researching liver biology and associated diseases.

One standard method of modeling and studying hepatic steatosis, known as fatty liver disease, is to evaluate the ability of a potential therapeutic to induce lipid accumulation in HepG2 hepatocytes. This condition is characterized by the abnormal storage of lipid droplets in liver cells and can be caused by various factors like obesity, insulin resistance, and excessive alcohol consumption. Induction of lipid accumulation in HepG2 cells mimics aspects of hepatic steatosis in vitro. Screening HepG2 cells for steatosis induction in vitro is essential for early drug discovery because it provides valuable insights into the potential hepatotoxicity of compounds, particularly those targeting PPAR and LXR. Both PPAR and LXR agonists have been associated with adverse effects such as hepatomegaly, hepatic steatosis, and dyslipidemia in preclinical and clinical studies.

This phenomenon occurs through several mechanisms orchestrated by PPAR and LXR signaling pathways. These receptors regulate lipid metabolism by promoting fatty acid uptake, synthesis, and storage within hepatocytes. Activation of PPARs and LXRs stimulates the expression of genes involved in lipogenesis and adipogenesis, leading to increased lipid droplet formation. PPAR and LXR agonists also alter lipid transport processes, enhancing fatty acid uptake

from circulation and promoting cholesterol efflux from cells. These changes result in the accumulation of triglycerides and cholesterol esters within hepatocytes. Furthermore, activation of PPARs and LXRs can induce inflammation and oxidative stress in the liver, exacerbating hepatocyte injury and contributing to steatosis development.

Overall, the dysregulation of lipid metabolism, lipid droplet formation, altered lipid transport, and inflammatory responses mediated by many PPAR and LXR agonists have hindered the advancement of these classes of compounds toward clinical application. To assess potential toxicity profiles associated with selective PPAR modulation and inherent toxicities related to ADME physiochemical properties, AU-403 was evaluated and compared to established PPARγ agonist rosiglitazone, PPARδ agonist GW-0742, and LXR pan agonists T0901317 and GW3965. All of these reference compounds are known to exhibit hepatic toxicities. HepG2 predominantly expresses PPARα, ruling out strict PPARγ and PPARδ gene transcriptional regulation on the observed toxicity.

PPAR Agonist Lipotoxicity Profile Evaluation in Hepatocytes (HepG2)

HepG2 cells were treated for twenty-four hours at 5 and 10 uM drug concentrations under standard conditions, as shown in **Figure 14.**, compared to a dimethyl sulfoxide (DMSO) vehicle-treated control. The extent of lipid accumulation after drug treatment was evaluated by Oil red O staining, similar to the method described in the previous section for 3T3-L1 adipocyte differentiation. The Oil Red O stain results show a comparable dose-response increase in hepatic lipid induction for both rosiglitazone and GW-0742. Interestingly, GW-0742 has a reported PPARγ EC50 value of 2 uM and had no effect on 3T3-L1 adipocyte differentiation, yet it displays a similar hepatic lipid induction profile compared to the PPARγ agonist rosiglitazone. In comparison, AU-403 was shown to have some degree of PPARγ activation, evidenced by the results in Table 1 and Figure 10, yet had no effect on hepatic lipid induction, instead appearing to decrease lipid content with an increasing dose-response indicative of PPARα hepatic gene induction.

LXR Agonist Lipotoxicity Profile Evaluation in Hepatocytes (HepG2)

The compound T0901317 appeared to have a comparably modest effect on lipid induction with both drug concentrations. Based on the role of LXRα in hepatocytes, the degree of lipid induction could be reasoned to be partially dependent on the availability of extracellular lipid uptake in the form of LDL and not an immediate consequence of gene induction. The results from the GW3965 treatment group support this assessment, which had no impact on hepatic lipid induction with an increasing dose response. Notably, Caymen Chemical reports GW3965 as having a six-fold preference for LXRβ over LXRα. These results suggest that LXRα is primarily responsible for gene-specific hepatic lipid induction, which is avoided by compound 7 (AU-403).

Both rosiglitazone and GW-0742 are highly selective for their target receptors, 60 nM and 1 nM, respectively. However, GW-0742 reportedly activates PPARα at 1 uM concentrations thirty times more potent than the well-tolerated PPARα agonist fenofibrate. Rosiglitazone is reported as having no PPARα activity, however, it displayed a similar hepatic lipid induction to GW-0742.

Figure 14. PPAR/LXR Agonist Relative Lipid Accumulation Results: Hepatic (HepG2) Lipotoxicity

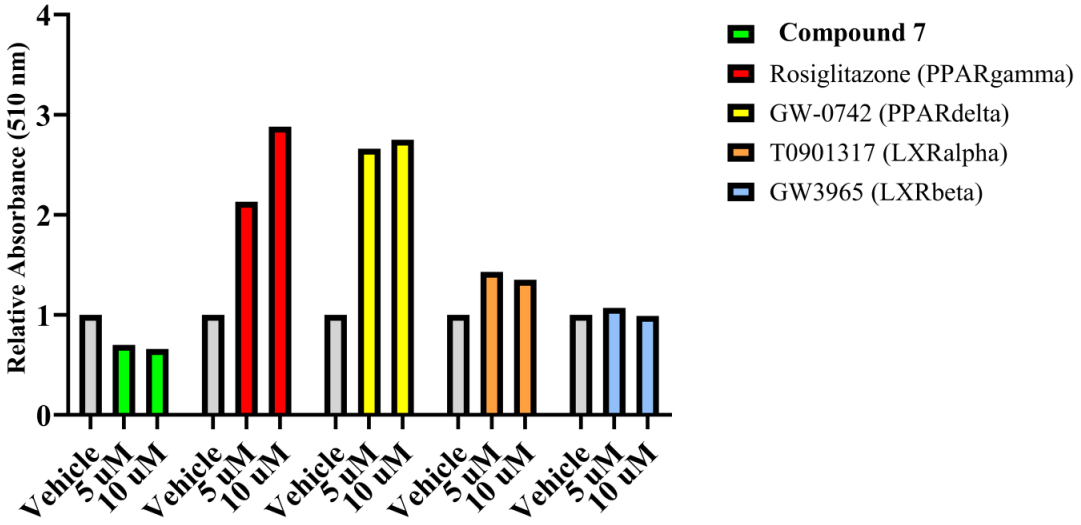

Values were determined spectrophotometrically by standardizing the absorbance measurement of the oil red O stain at 510 nm to that of a DAPI stain at Ex 358/ Em 461. All values were the average of three replicate samples.

2.7 In Vitro Evaluation of Compound 7 (AU-403): LXR Transactivation

Further testing was conducted in vivo with compound 7 (AU-403) in 3xTg AD mice given a one-month daily intraperitoneal injection of 5 mg/kg (data not reported). The results from the AU-403 treatment determined a significant reduction in brain Aβ plaque deposition compared to a vehicle-treated control and a significant reduction in tau hyperphosphorylation (data not reported). Additionally, AU-403 induced uptake of a fluorescent-tagged Aβ peptide (HiLyte Fluor 488) in primary rat microglial cells comparably to LXR pan agonist GW3965 (data not reported). These results prompted further investigation to determine AU-403 activation of LXRα and LXRβ.

LXRs and PPARs are nuclear receptors that regulate lipid metabolism, but they have distinct roles in autophagy and clearance processes. While PPARs primarily regulate lipid metabolism and adipocyte differentiation, LXRs have been implicated in cholesterol homeostasis and inflammation. Specifically, LXRs promote cholesterol efflux and inhibit cholesterol synthesis, which can impact cellular processes such as autophagy. In contrast, PPARs are more directly involved in regulating lipid storage and adipogenesis. Therefore, LXRs may indirectly influence autophagy and clearance more than PPARs, with LXRs primarily affecting cholesterol metabolism pathways that intersect with autophagic processes.

LXRs play a crucial role in the autophagic clearance Aβ in AD due to their involvement in regulating lipid transport. Autophagy is a cellular process responsible for degrading and recycling damaged or dysfunctional cellular components, including misfolded proteins such as Aβ. LXRs have been found to regulate gene expression in autophagy, promoting the clearance of Aβ aggregates from the brain. Additionally, LXRs have anti-inflammatory properties and can suppress neuroinflammation associated with AD progression. Therefore, activation of LXRs has emerged

as a potential therapeutic strategy for enhancing Aβ clearance and reducing neuroinflammation in AD. However, the precise mechanisms by which LXRs modulate autophagy and Aβ clearance in the context of AD pathology require further investigation.

Compound **7** (AU-403) was evaluated for human LXR in vitro potency and efficacy using a cell-based transactivation assay in HEK-293 cells transfected with a Gal-4 plasmid vector containing the hLXRα and hLXRβ ATP-binding cassette transporter (ABCA1) - LXR recognition elements where the individual experimental values were standardized to renilla (**Table 8.**). For AU-403, Emax was measured relatively to representative LXR agonists GW3965 (LXRα EC_{50} = 190 nM, LXRβ EC_{50} = 30 nM) and T0901317 (LXRα ~ LXRβ EC_{50} = 50 nM).

A comparison between the more selective LXRβ agonist GW3965 and LXR pan agonist T0901317 with AU-403 (Table 7) demonstrated an apparent selective activation of the LXRβ isoform coinciding with a comparative hepatocyte lipid accumulation profile observed by GW3965 in Figure 14. Unlike GW3965 and T0901317, however, AU-403 displayed no apparent activation for LXRα. This result is unique as very few LXR agonists have been demonstrated to display an inherent selection between the two isoforms. Instead, selectivity is gained through ligand size and hydrophobic surface area. Similar to the observation of PPARδ agonists.

In combination with the hepatic lipid accumulation profile observed by AU-403 in Figure 14., these results have been hypothesized to be a consequence of selectivity for PPARα over LXRα. As AU-403 displayed no apparent activation of LXRα in transactivation assays and a lipotoxicity profile similar to PPARα agonist fenofibrate.

Table 8. Transactivation Activity LXR Result: Compound 7 (AU-403)

	hLXRα		hLXRβ	
Compound	**EC_{50} (nM)**	**E_{max} (%)**	**EC_{50} (nM)**	**E_{max} (%)**
7	nd	ns	*43	~ 70
GW3965	190		30	
T0901317	50		50	

E_{max} = maximum activation in percent of control compound. EC_{50} = reported compound values.*Estimate of compound 4 EC_{50} based on % E_{max} of control compound. All E_{max} values were the average of three replicate samples. nd = not determined. ns = not a significant change from control.

2.8 In Silico LXR Structural Optimization: Structure Identification of Compound 7 (AU-403)

The compound 7 (AU-403) LXR transactivation results and a well-balanced safety profile demonstrated by the physiochemical evaluation presented a unique opportunity to further explore selective optimization of the LXRβ LBD. This distinct avoidance of LXRα-induced hepatotoxicities via LXRβ selectivity could provide renewed therapeutic potential in this previously stigmatized class of compounds. To further understand potential modes of LXR selectivity related to ligand binding, in silico modeling was used to evaluate the predicted binding poses of AU-403 in representative LXR cognate ligand binding poses. To compare LXRβ selectivity, AU-403 was docked into the cognate binding poses for GW3965 using the PDB 3IPQ LXRα LBD and 4NQA LXRβ LBD. The lowest-energy docking poses generated for AU-403 used standard precision rigid ligand docking. These poses were subjected to flexible-induced fit docking to gain predictive accuracy (**Figure 15.**).

Rigid ligand docking and induced fit docking are two prominent methods used in the computational modeling of ligand-receptor interactions, each with distinct approaches and applications. Rigid ligand docking assumes that both the ligand and the receptor maintain fixed conformations throughout the docking process. This method simplifies calculations and is computationally efficient, making it suitable for high-throughput virtual screening where speed is essential. However, it often fails to capture the dynamic nature of biological systems, potentially missing fundamental interactions and yielding lower accuracy in predicting binding affinities and specificities.

In contrast, induced fit docking allows flexibility in both the ligand and the receptor. This method acknowledges that receptors can undergo conformational changes upon ligand binding, resulting in a more accurate representation of molecular interactions. Induced fit docking provides a more realistic binding model in vivo by iteratively adjusting the receptor's conformation and redocking the ligand. This flexibility comes with a higher computational cost and increased complexity, making induced fit docking slower and more computationally intensive than rigid ligand docking. However, the enhanced accuracy of induced fit docking in capturing the true nature of ligand-receptor interactions makes it invaluable in detailed drug design and understanding intricate biological mechanisms. While rigid ligand docking offers speed and simplicity, induced fit docking delivers precision and realism, each serving distinct roles.

It is essential to consider induced fit docking for nuclear receptors due to their inherent flexibility and dynamic behavior. Nuclear receptors undergo substantial conformational changes upon ligand binding, affecting ligand specificity and affinity. Induced fit docking accurately models these adjustments, offering better predictions than rigid docking methods. This is crucial for understanding how different ligands induce distinct receptor conformations, impacting co-activator and co-repressor recruitment for gene regulation. In drug design, particularly for diseases related to nuclear receptor dysfunction, induced fit docking facilitates the development of more effective and selective therapeutics. Additionally, it enhances understanding of the detailed mechanisms of ligand-induced receptor activation, providing deeper insights into physiological processes.

From the AU-403-induced fit predicted binding pose generated for LXRβ, the 1,1-biphenyl ring containing the trifluoromethyl was deleted to create an R group extension to the

AF-2 Tryptophan and Histidine residues. This trifluoromethyl substituent appeared to be sterically hindering aromatic interactions with the LXRβ AF-2, preventing strong interactions, an observed requirement for PPAR activation. Thus, a linear extension was built from the AU-403-induced fit docking pose using R-group enumeration with pi-cation aromatic ring fragments. Pi-cation aromatic rings were hypothesized to have increased interaction in the form of hydrogen and aromatic hydrogen bonds to assist in the recruitment and stabilization of the LXRβ AF-2 (**Figure 16.**).

While interactions with the AF-2 had increased with the first R-group enumeration, docking scores had depreciated, and the linking imidazole ring was devoid of interaction with the active site Phenylalanine residues, a potential determinant to gain an increase in predicted binding affinity. To circumvent this issue, a benzyl carbon was inserted between the imidazole ring and parent AU-403 structure to allow conformational flexibility and increase the opportunity to take advantage of aromatic residue interactions. However, this additional benzyl carbon caused the pi-cation aromatic ring system to extend too far into the AF-2, creating several repulsive contacts that would infer disruption and destabilization toward activation (**Figure 17.**).

Based on the pi-cation R-groups that displayed favorable interactions with the LXRβ AF-2 Tryptophan and Histidine residues, i.e., furan and pyridine, it was decided to shift the pi-cation aromatic ring to the 1,1-biphenyl 4-position (R1) and the benzyl aromatic substituent was moved to the 2-position (R2). This change in structural features allowed the R1 substituent to form aromatic interactions with the AF-2 Histidine residue and the R2 to form aromatic interactions with the Phenylalanine residues, allowing a conformational preference for alignment (**Figure 18.**).

The AU-403 derivatization for LXRβ selective ligands included R1-groups consisting of 3-furanyl and 2-, 3-, and 4-pyridinyl aromatic rings that could form strong interactions with the AF-2 and weakly polar 2-, 3-, and 4-fluorophenyl rings for the R2-groups to strengthen aromatic interactions for enhanced predicted binding affinity. To test this hypothesis, a neutral phenyl R2 substituent was used as a control to assess experimental SAR.

Figure 15. Compound 7 (AU-403) Induced Fit Docking: Structural Optimization for the LXRβ LBD

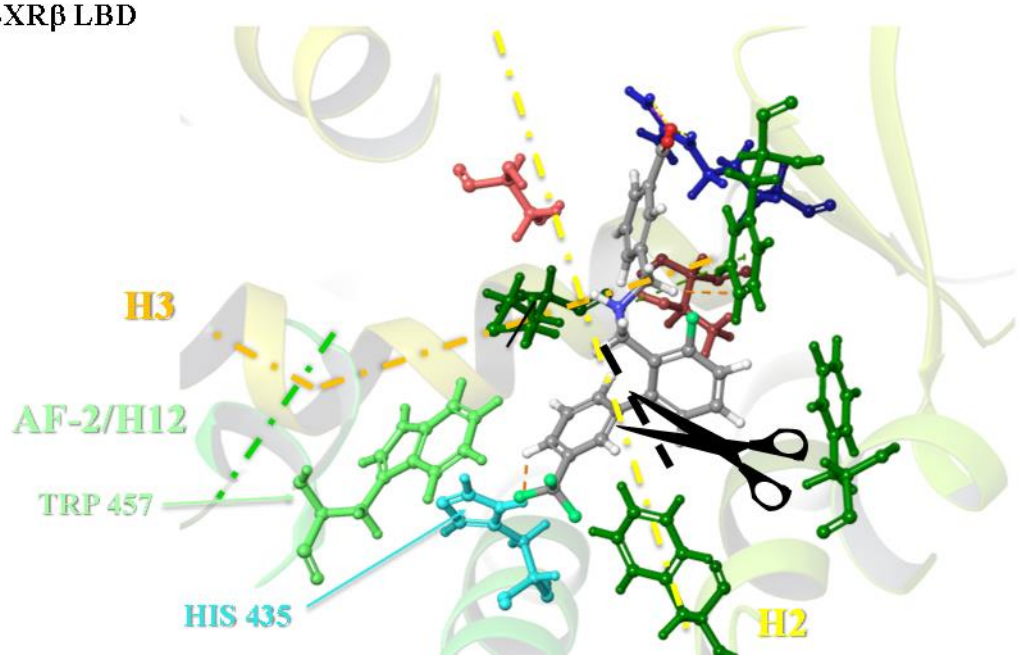

Using 3D Builder in the Maestro workspace, the induced fit docking pose for AU-403 was derivatized in the biphenyl 6-position to reduce steric interactions with the LXRβ AF-2.

Figure 16. Compound 7 (AU-403) Derivatization by Pi-Cation R-Group Enumeration

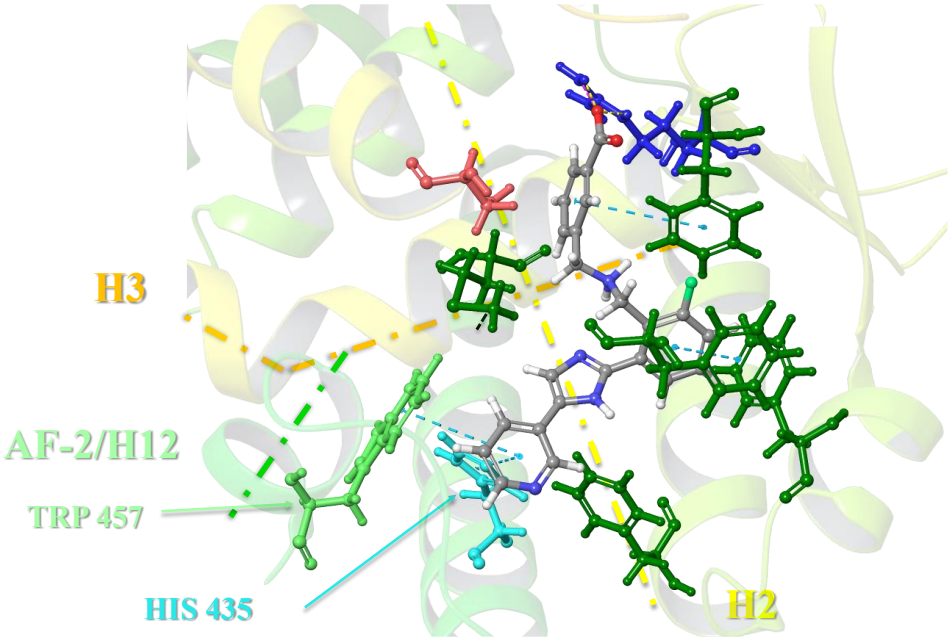

R-group enumeration was used to extend functionality to the LXRβ AF-2 using pi-cation aromatic rings. While the Tryptophan and Histidine AF-2 residues formed aromatic hydrogen bonds with the ligands pyridinyl ring, overall docking scores had decreased in comparison to the AU-403 parent structure.

Figure 17. Compound 7 (AU-403) Derivatization Benzyl Extension of Pi-Cation R-Group Enumeration

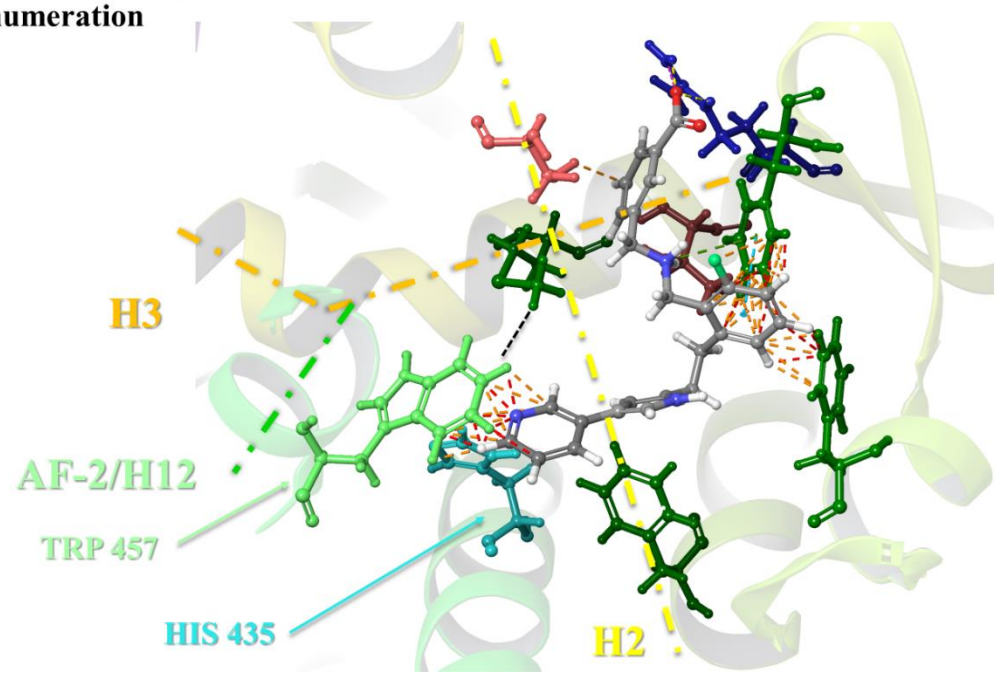

A benzyl carbon was inserted between the imidazole ring and parent AU-403 structure in the 1,1-biphenyl 6-position to allow conformational flexibility and increase the opportunity to take advantage of aromatic residue interactions. This structural modification increased the overall length of the ligands to extend into the AF-2 creating repulsive interactions with the Tryptophan and Histidine. Additionally, this steric clash prevented conformational alignment with the Phenylalanine residues that line the LXRβ LBD.

Figure 18. Compound 7 (AU-403) Derivatization to Generate LXRβ Selective Leads

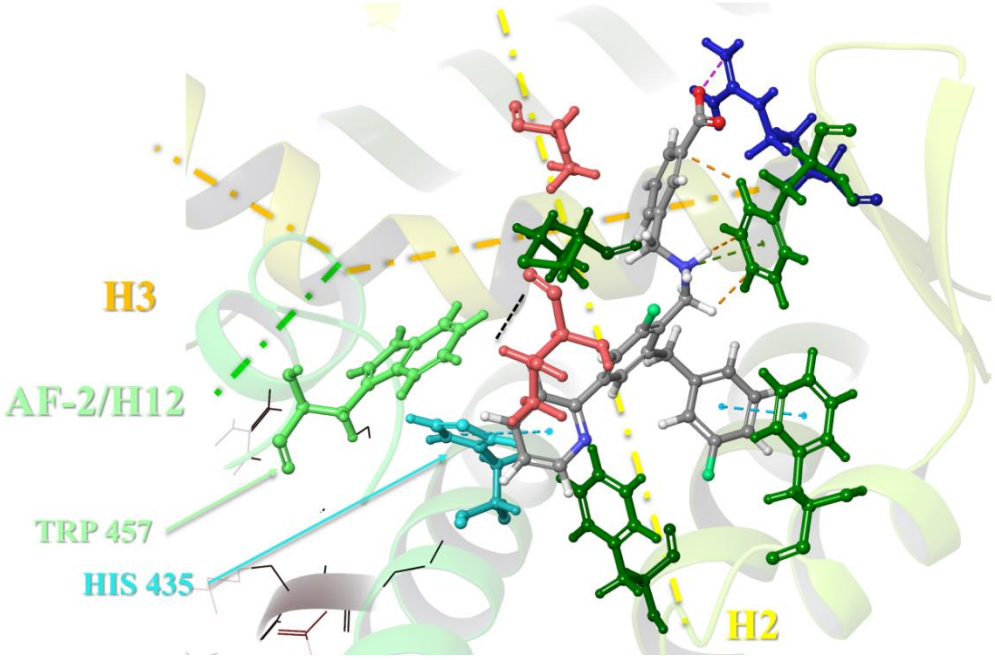

Based on favorable AF-2 interactions with the pi-cation R-group substituents, i.e., furan and pyridine, it was decided to shift the pi-cation aromatic ring to the 1,1-biphenyl 4-position (R1) and the benzyl aromatic substituent was moved to the 2-position (R2). This change in structural features generated favorable binding conformations that allowed the R1 pi-cation aromatic rings to form aromatic interactions with the AF-2 Histidine residue and the R2 benzyl substituent to form aromatic interactions with the Phenylalanine residues and was chosen as the lead scaffold for synthesis.

Figure 19. Compound 7 (AU-403) Derivative LXRβ Selective Leads

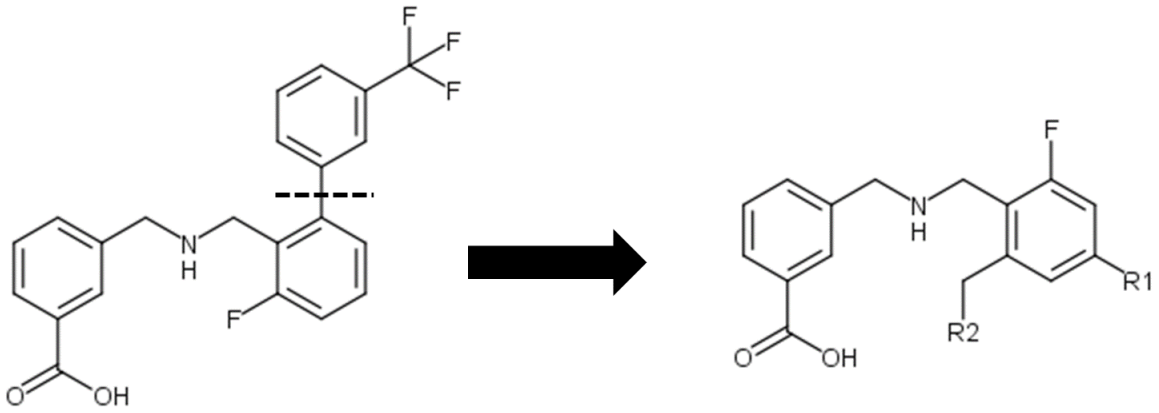

R1 Pi-Cation:
Pi-deficient heteroaromatic substituents (2-, 3-, and 4-pyridine)

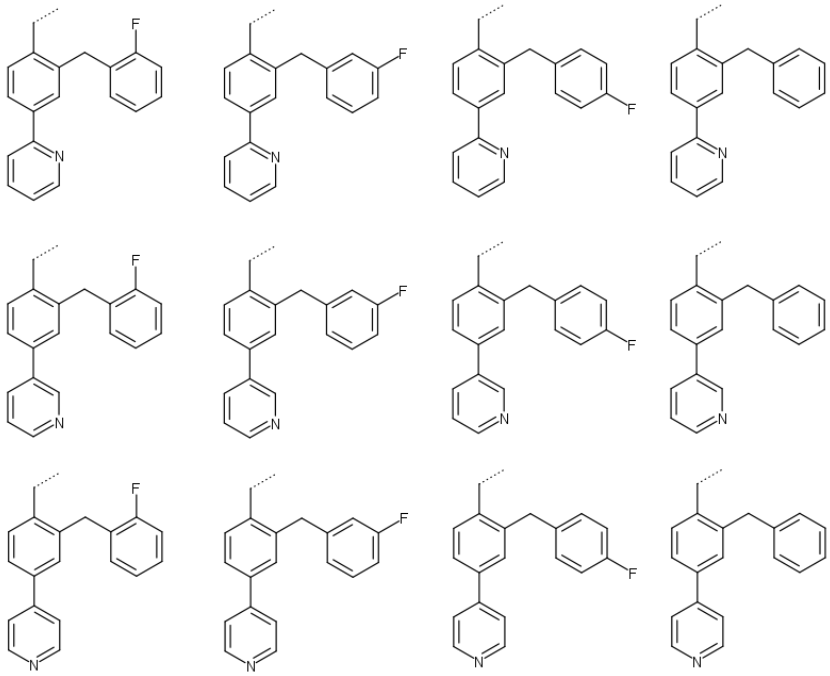

R1 Pi-Cation:
Pi-excessive
heteroaromatic substituents
(3-furan)

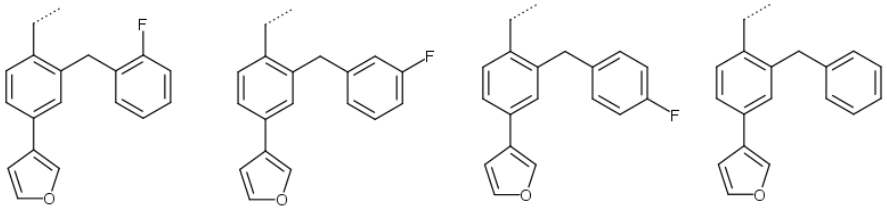

R1 Pi-Cation:
Neutral Control (phenyl)

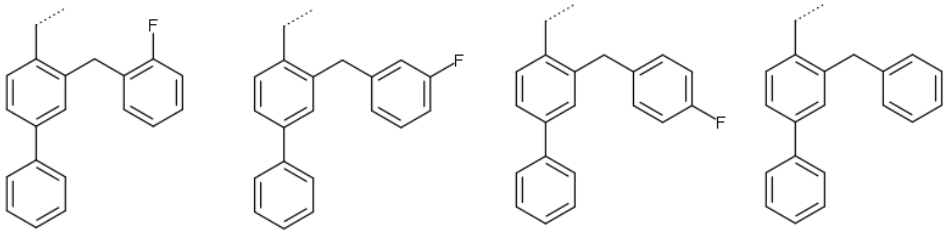

The compound 7 (AU-403) structural derivatives for LXRβ selectivity were chosen based on conformational alignment from the R2 benzyl substituents which position the R1 pi-cation aromatic substituents to form favorable hydrogen and aromatic hydrogen bonds with the AF-2 Tryptophan and Histidine residues. It was hypothesized that ligands activated the AF-2 of LXRs similar to PPARs. Thus, the goal was to maximize the ligand's ability to form stronger interactions that could recruit the AF-2.

2.9 Synthetic Scheme for Compound 7 (AU-403) LXRβ Selective Derivatives

The synthetic sequence described in **Figure 20.** started with an alkylation of **8** in the presence of iodomethane and Cs_2CO_3 in dimethylformamide (DMF) to generate 4-bromo-2-fluoro-5-methyl benzoate intermediate **9**. Tetrakis(triphenylphosphine)palladium (0) ($Pd(PPh_3)_4$) catalyzed Suzuki coupling between intermediate **9** and aryl boronic acids with Cs_2CO_3 in DMF to generate intermediates **10a-d**. Benzylic bromination of intermediates **10a-d** in the presence of N-bromosuccinimide (NBS) and azobisisobutyronitrile (AIBN) in DCE afforded the benzyl bromide intermediates **11a-c**. Suzuki coupling procedure between intermediates **11a** and **11c** with aryl boronic acids yielded the benzyl intermediates **12a-e**. Selective reduction of the intermediates **12a-e** with diisobutylaluminum hydride (DIBAL-H) in hexanes at cryogenic temperature using a dry ice and ethyl acetate cooling bath of -78 °C generated the aldehyde intermediates **13**. A reductive amination procedure with intermediate **13** and **4** afforded the secondary amine intermediates **14**. Basic hydrolysis of intermediates **14** yielded the compound 7 (AU-403) derivative LXRβ selective agonist series **15**. (**Steps D, F, and G reference Figure 10**)

Figure 20. Derivative Syntheses for Compound 7 (AU-403): LXRβ Selective Agonists Containing a 3-benzyl-1,1-biphenyl Scaffold

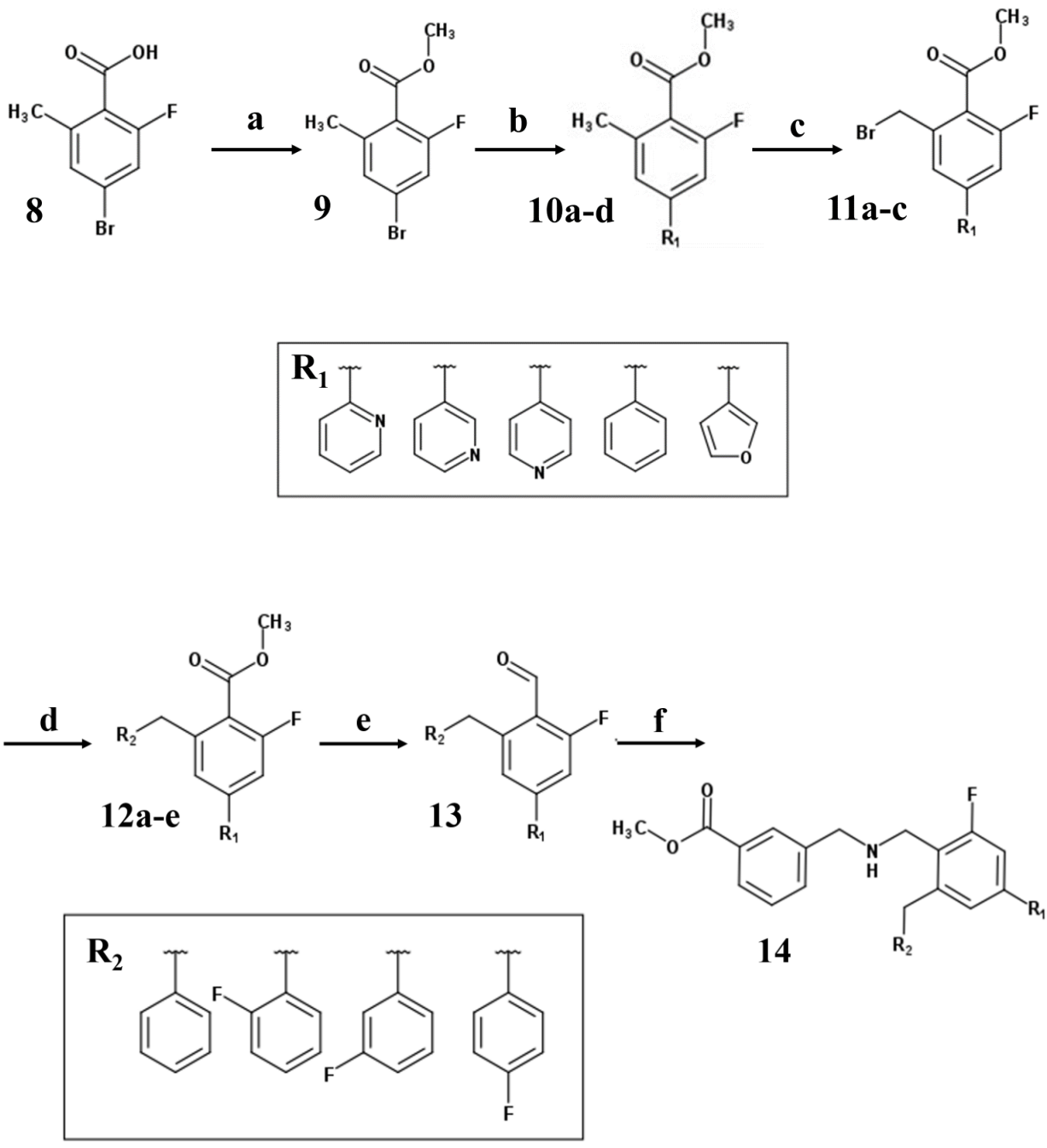

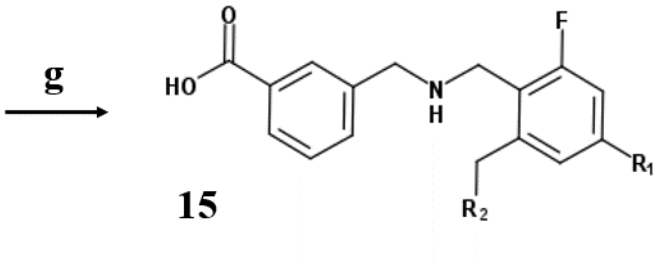

15

Reagents and conditions: (a) iodomethane, Cs_2CO_3, DMF; (b) arylboronic acid, Cs_2CO_3, $Pd(PPh_3)_4$, DMF; (c) NBS, AIBN, DCE (70-75 ˚C); (d) arylboronic acid, $Pd(OAc)_2$, TBAB, K_3PO_4, THF/H_2O (50 ˚C); (e) DIBAL-H, Hexane (-78 ˚C); (f) (i) (aminomethyl)benzoate, DCE; (ii) $NaBH_4$, MeOH (50 ˚C); (g) $NaOH{\cdot}H_2O$, MeOH.

2.10.1 In Silico LXR SAR: Re-Evaluation of LXRβ Selective Leads

The synthetic schemes described in **Figure 20. c,d** presented numerous difficulties in generating pi-deficient and pi-excessive heteroaromatics as they did not survive the benzylic bromination and/or the second Suzuki coupling. Of the lead heteroaromatic ligands, only the 3-pyridinyl derivative was successfully synthesized. The neutral phenyl derivatives were able to be achieved efficiently.

Due to the difficulty synthesizing the heteroaromatic lead ligands, dose-response curves for the derivative fragment compounds **Figure 21.** were compared similarly against GW3965 for LXRα and LXRβ activation before the final synthetic steps to generate the complete derivatives containing the parent active site moiety meta-substituted benzoic acid functionality for compounds **13-15** (**Figure 20.**). It was hypothesized that these fragment pieces would have little activity as the AU-403 parent active site moiety was the major determinant for conformational preference in the LXR LBD. The results have not been reported, as the compounds **12a-e** did not produce a significant change in activation for either LXRα or LXRβ. These results prompted continued evaluation of in silico modeling to better understand the role of ligands at the LXR LBDs and to find alternative structures that would be more synthetically accessible. The initial step towards synthetic accessibility was to reevaluate the neutral control phenyl derivatives compounds **12b-**e as their intended complete derivative compounds **15b-e**.

Figure 21. Successfully Synthesized Compound 7 (AU -403) LXRβ Selective Fragments Containing a 3-benzyl-1,1-biphenyl Scaffold

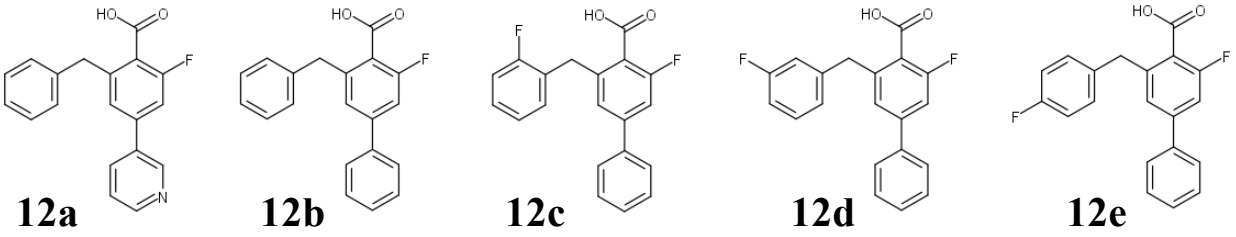

Remaining Synthetic Steps to LXRβ Selective Derivatives

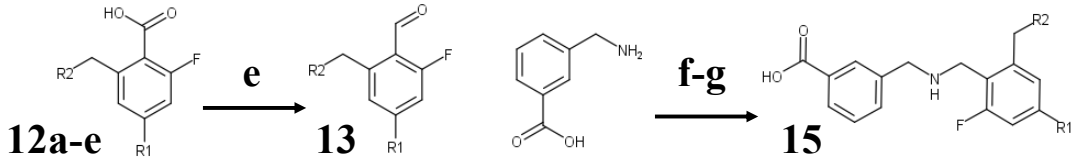

The compound 7 (AU-403) LXRβ selective derivative fragments were tested for transactivation of the LXRα and LXRβ receptors before synthetic steps for selective reduction and subsequent attachment of the AU-403 aminomethyl benzoate active site moiety to generate compounds 13-15, Figure 20.

2.10.2 In Silico LXR SAR: Receptor Site Map Analysis

The analysis of LXRα and LXRβ LBD crystal structures (**Figure 22.**) revealed dramatic differences between every SiteMap descriptor. The LXRα LBD receptor site volume is approximately two-fold larger than the LXRβ LBD receptor site. This result is likely in response to the cognate ligand GW3965, as SiteMap parameters were chosen to evaluate a single ligand binding site. Interestingly, GW3965 is a large lipophilic ligand with a molecular weight of 582 g/mol and EC50 values of 6.3-fold greater at LXRα.

LXRβ has a Balance score that is 2.5-fold greater than LXRα, indicating a stronger preference for hydrophobic ligands and a mechanism of substrate selectivity, much like PPARδ (Figure 4.). LXRα action is primarily regulated by oxysterols, which are oxidized forms of cholesterol, to upregulate cellular bile acid synthesis and efflux mechanisms in the clearance of excess cholesterol. Additionally, these results reflect specific differences observed in LXR isoform-specific physiological function as LXRα tissue expression is localized to glandular epithelium tissues, and LXRβ expression is localized to specialized epithelium tissues.

The LXR LBD AF-2 exhibits less dependency on polar interactions than the PPAR receptors. This means that the activation of LXRs is less reliant on polar interactions within the ligand-binding pocket for its activation than that of the PPARs. Instead, LXRs are more influenced by hydrophobic interactions and structural changes induced by ligand binding. This characteristic of LXRs contributes to their unique ligand-binding properties and may impact the specificity and potency of ligands that interact with the LXR AF-2 domain. Overall, understanding the distinct structural features and ligand-binding mechanisms of LXRs compared to PPARs is essential for designing selective modulators and elucidating their biological effects.

Figure 22. Results from Sitemap Analysis of LXRα and LXRβ

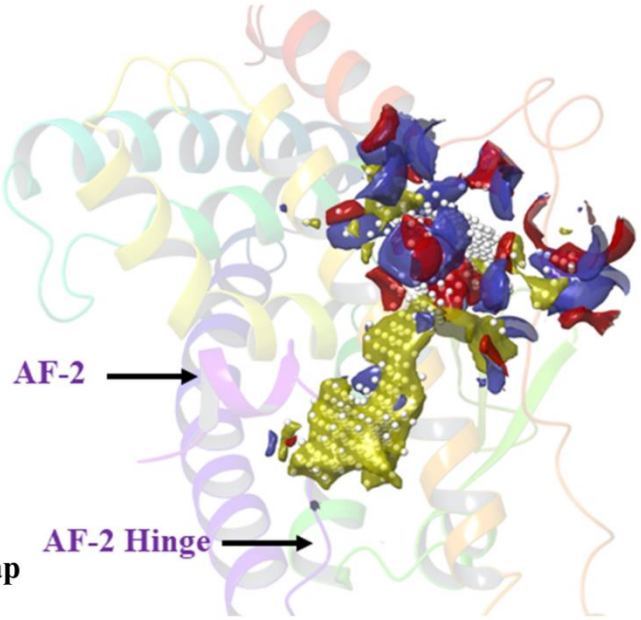

LXRα – LBD SiteMap
(PDB: 3IPQ)

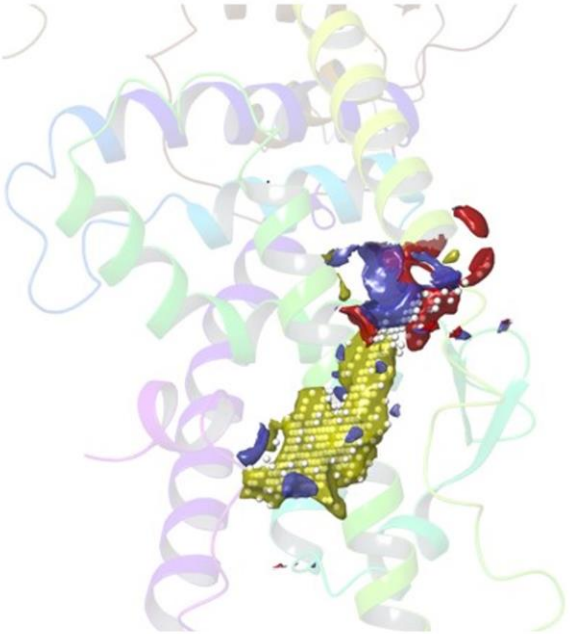

LXRβ – LBD SiteMap
(PDB: 4NQA)

Sitemap Descriptors	LXRα	LXRβ
Volume	830	438
Phobic	1.985	3.846
Philic	0.751	0.556
Balance	2.643	6.922
Dscore	1.151	1.322

LXR sitemap visual analysis: **Hydrogen-bond Acceptor map**, **Hydrogen-bond Donor map**, and **Hydrophobic map**. Phobic—regions that are favorable for occupancy by hydrophobic ligand groups. Philic—regions that are favorable for occupancy by hydrophilic ligand groups. The phobic and philic scores have been calibrated so that the average score for a tight-binding site is 1.0. Balance – phobic/philic. Dscore = 0.094 sqrt(n) + 0.60 e - 0.324 p. *n* – number of site points. *e* – enclosure score. *p*- hydrophilic score. Dscore values greater than 1 represent hydrophobic sites suitable for tight binding.

2.10.3 In Silico LXRα SAR: Protein Energy Minimization

Protein-energy minimization is a computational technique used to optimize the three-dimensional structure of a protein molecule by minimizing its potential energy. Performing protein energy minimization aims to obtain a stable and energetically favorable protein conformation representing its lowest energy state. This optimized structure can provide valuable insights into the protein's stability, dynamics, and interactions with other molecules, such as ligands or other proteins. Minimizing the protein's potential energy allows unfavorable interactions between atoms or residues within the protein molecule to be alleviated, leading to a more realistic representation of its native conformation. Additionally, energy minimization can be used to predict conformational changes induced by ligand binding or mutations, aiding in understanding protein function and dynamics.

Understanding a protein's cognate and native-apo poses is crucial for elucidating its structure-function relationship and drug discovery efforts. The cognate pose represents the protein's conformation when bound to its native ligand or substrate, while the apo pose represents the protein in its ligand-free state. Comparing these two poses can provide insights into how the protein undergoes conformational changes upon ligand binding and how these changes affect its function. This leads to understanding the crucial protein-ligand contacts required to generate an active pose.

Protein-energy minimization was employed to generate the apo pose, which allows for exploring the protein's inherent flexibility and dynamics without a ligand. This information is invaluable for designing ligands that can effectively target the protein by stabilizing its active conformation or modulating its activity. Additionally, understanding the apo pose can aid in virtual

screening studies to identify potential ligands or inhibitors through molecular docking simulations. Therefore, comprehending the differences between the cognate and apo poses provides critical insights into the molecular mechanisms underlying protein-ligand interactions, essential for rational drug design and optimization efforts.

Designing selective LXR agonists poses a significant challenge, as these receptors exhibit distinct conformational dynamics compared to other nuclear receptors like PPARs. To accurately predict the conformational requirements and efficacy of potential LXR agonists, generating an apo state of the LXR LBD utilizing protein structural energy minimization was imperative. The LXRα LBD exhibits unique conformational features in its apo state, essential for ligand binding and receptor activation. The apo-LXRα LBD (**Figure 23A**) undergoes a constriction when protein energy minimization occurs, forming a charge clamp between Glutamate 267 of the H2 helix and Arginine 305. A coordinating hydrogen bond with Glutamine 223 stabilizes this clamp, securing the H2 and H1 helices connected to the DNA Hinge Region. Furthermore, the AF-2 Tryptophan 443 residue is anchored by a bifurcated aromatic hydrogen bond from Histidine 421 and a hydrophobic contact between the Tryptophan indole 6-Hydrogen and the Methionine 298 sulfur atom, which stabilizes the AF-2/H12 helix to the H3 Helix (**Figure 23A**).

In contrast, the cognate-LXRα LBD (**Figure 23B**) displays a different conformation. It shows a disrupted charge clamp interaction, leading to the release of Glutamine 223 and the consequent liberation of the H1 helix from the H2 helix into an active state. This is significant as it shows that the contact between AF-2 Tryptophan 443 and Methionine 298 is lost, leading to the release of the AF-2/H12 helix from the H3 helix.

In the apo state, the constricted LBD signifies a significant conformational change upon ligand binding. The apo state represents the receptor without a ligand, where the LBD undergoes

energy minimization to optimize its conformation. This constricted state is characterized by specific interactions between key residues, such as a charge clamp formed between Glutamate 267 and Arginine 305, stabilizing the H2 helix. Moreover, the AF-2 region is secured by interactions involving Tryptophan 443 and Methionine 298, ensuring the stability of the AF-2/H12 helix. However, upon ligand binding, this constricted apo state transitions to a more open and active conformation, known as the cognate pose. The cognate pose disrupts the charge clamp, releasing the H1 helix and repositioning the AF-2 region for optimal ligand binding. This transition signifies a significant conformational change that enables the receptor to accommodate the ligand and initiate downstream signaling pathways. Understanding the dynamics of this conformational switch is crucial for designing ligands that can effectively modulate LXR activity for therapeutic purposes.

Figure 23. 3IPQ Minimized Apo-LXRα LBD and 3IPQ Cognate-LXRα LBD

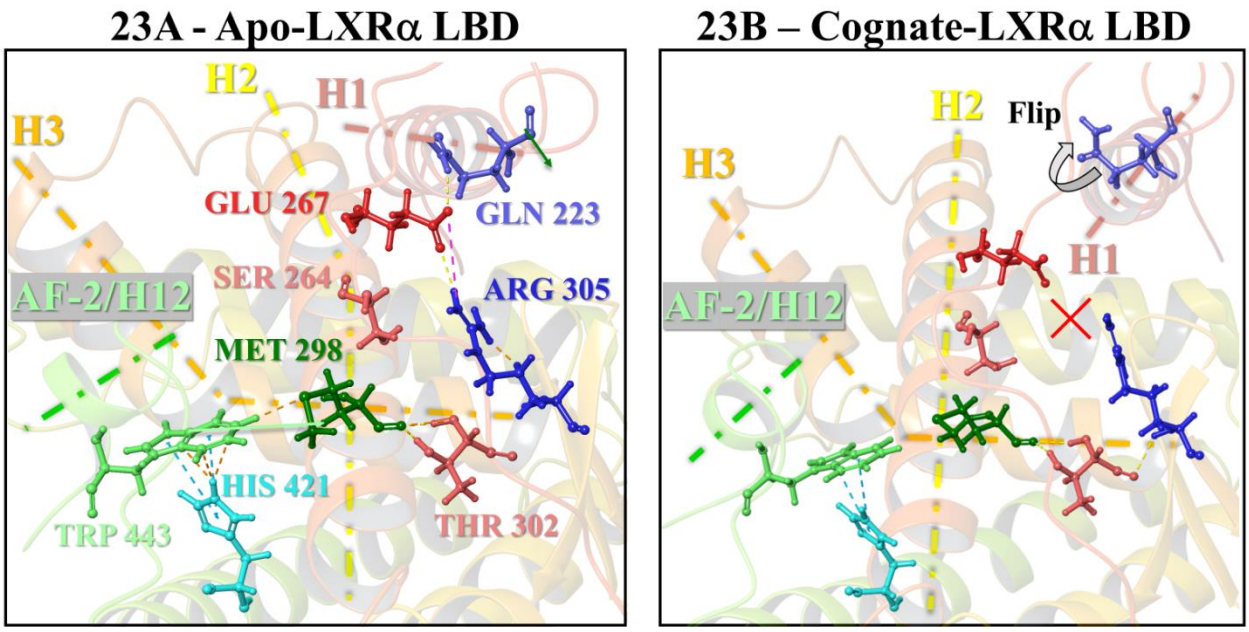

23A - Apo-LXRα LBD: The apo-LXRα LBD is constricted by protein energy minimization, which forms a charge clamp between the Glutamate 267 of the H2 helix and Arginine 305. This clamp is held in place by a coordinating hydrogen bond to Glutamine 223, which secures the H2 and H1 helix connected to the Hinge Region. Additionally, the AF-2 Tryptophan 443 residue is secured by a bifurcated aromatic hydrogen bond from Histidine 421 and a hydrophobic contact between the Tryptophan indole 6-Hydrogen and the Methionine 298 sulfur atom, which secures the AF-2/H12 and H3 Helix.

23B - cognate-LXRα LBD: In the cognate-LXRα LBD the charge clamp is disrupted, resulting in a flip-out of Glutamine 223 and the release of the H1 helix from the H2 helix to an active state. The contact between AF-2 Tryptophan 443 and Methionine 298 is lost, as the AF-2/H12 helix is released from the H3 helix.

2.10.4 In Silico LXRβ SAR: Protein Energy Minimization

In the apo state of the LXRβ LBD, protein-energy minimization causes a charge clamp to form between Glutamate 281 and Arginine 319 in the H2 helix. This clamp is stabilized by a coordinating hydrogen bond to Asparagine 239, ensuring the stability of the H2 and H1 helices connected to the DNA Hinge Region. An aromatic hydrogen bond and a pi-pi interaction from Histidine 421 also secure the AF-2 Tryptophan 457 residue. Unlike in LXRα, vdW interactions position the Methionine 312 sulfur atom between the Tryptophan 457 indole 5-H and 6-H (**Figure 24A**).

On the other hand, in the cognate state of the LXRβ LBD, the charge clamp observed in the apo state is disrupted (**Figure 24B**). However, this disruption is less dramatic than the analogous interaction observed in LXRα (**Figure 23**), as it is accompanied by compensatory ligand contacts that release the H1 helix from the H2 helix by disrupting the coordinated hydrogen bond involving Asparagine 239. Furthermore, the conformation of the AF-2 Tryptophan 457 residue undergoes a retraction, aligning the indole 5-H and Methionine 312 sulfur atom to form an energetically favorable interaction. This interaction is crucial in destabilizing the release of the AF-2/H12 helix from the H3 helix, facilitating the transition to an active conformation conducive to ligand binding and downstream signaling.

Compared to the LXRα LBD, the structural changes observed in the LXRβ LBD during the transition from the apo to the cognate state exhibit similarities and differences. Like LXRα, LXRβ undergoes a conformational change characterized by the disruption of a charge clamp in the apo state, which is replaced by compensatory ligand contacts in the cognate state. However, the specific residues involved in forming the charge clamp and the subsequent ligand interactions

vary between LXRα and LXRβ due to differences in their amino acid sequences and structural characteristics. Additionally, while both LXRα and LXRβ undergo rearrangements in the AF-2 helix and its associated residues, the precise details of these conformational changes may differ between the two isoforms. Despite variations in substrate conformational requirements, the overall mechanism of ligand-induced conformational changes leading to activation of LXR signaling pathways appears to be conserved between LXRα and LXRβ.

Figure 24. 4NQA Minimized Apo-LXRβ LBD and 4NQA Cognate-LXRβ LBD

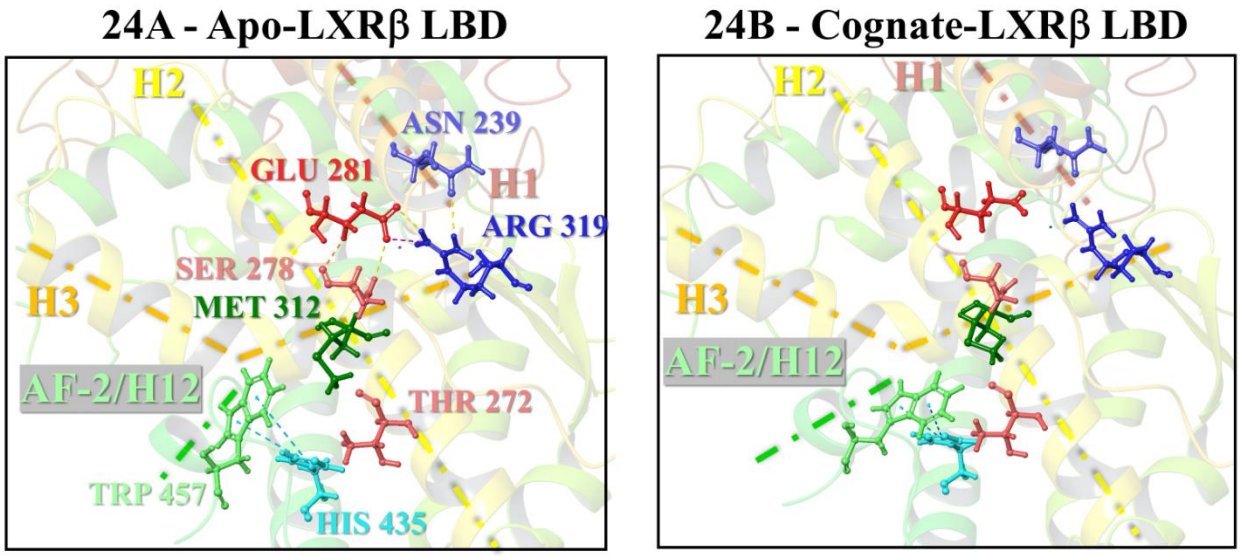

24A - Apo-LXRβ LBD: When protein-energy minimization is applied to the LXRβ LBD, it forms a charge clamp between the H2 helix Glutamate 281 and Arginine 319. This clamp is secured by a coordinating hydrogen bond to Asparagine 239, which secures the H2 and H1 helix connected to the Hinge Region. The AF-2 Tryptophan 457 residue is also secured by an aromatic hydrogen bond and a pi-pi interaction from Histidine 421. Importantly, unlike in LXRα, vdW interactions position the Methionine 312 sulfur atom between the Tryptophan 457 indole 5-H and 6-H.

24B - Cognate-LXRβ LBD: In the cognate-LXRβ LBD, the charge clamp is disrupted and replaced by compensatory ligand contacts, which release the H1 helix from the H2 helix by disrupting the coordinated Asparagine 239 hydrogen bond. Additionally, the AF-2 Tryptophan 457 residue conformationally retracts, aligning the indole 5-H and Methionine 312 sulfur atom to form an energetically favorable interaction that restabilizes the release of the AF-2/H12 helix from the H3 helix.

2.10.5 In Silico LXRα SAR: Minimized AF-2 Visualization

The LXRα LBD's apo state is a complex system that relies on specific residue interactions to maintain stable conformational dynamics. An in-depth visualization of the energy involved reveals that the Methionine 298 sidechain undergoes a precisely calculated rotation at a dihedral angle of 41.1˚. This position aligns the sulfur atom and the indole ring 6-H of Tryptophan 443 to create a pseudo-hydrogen bond, stabilizing the AF-2/H12 and H2 helices with incredible precision. Additionally, the Histidine 421 imidazole sidechain, oriented at a ring angle of 85.9˚, forms a robust N1-H bifurcated hydrogen bond with the pyrrole and benzene rings of Tryptophan 443 (**Figure 25A**).

In contrast, the cognate state of the LXRα LBD sees the Methionine 298 sidechain undergo a more pronounced rotational dihedral angle of 68.6˚. This shift reduces the strength of vdW interactions between the Tryptophan 443 indole ring 6-H and 7-H. The orientation of the Histidine 421 imidazole sidechain at a ring angle of 73˚ allows it to maintain its interaction with the Tryptophan 443 indole ring. This transformation turns the N1-H interaction into an aromatic hydrogen bond with the indole benzene ring (**Figure 25B**). These structural changes highlight the LXRα LBD's dynamic nature and remarkable adaptability to ligand binding - a key factor in the transition from the apo to the cognate state.

Figure 25. 3IPQ Minimized Apo-LXRα LBD and 3IPQ Cognate-LXRα LBD Energy Visualization

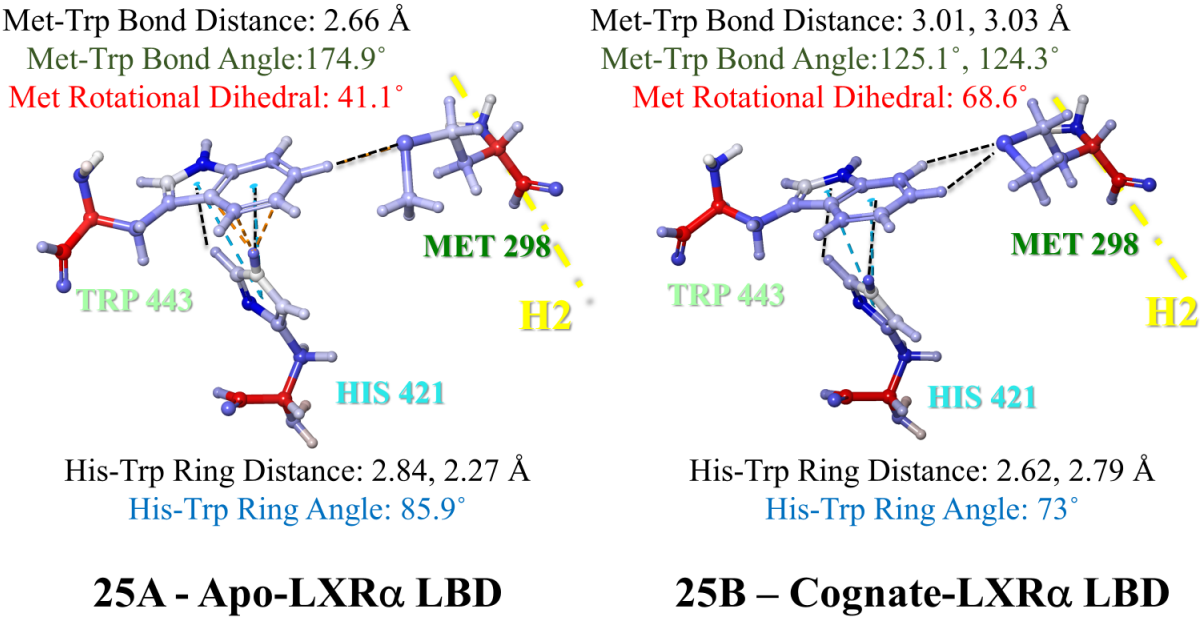

25A - Apo-LXRα LBD **25B – Cognate-LXRα LBD**

25A - Apo-LXRα LBD: Energy visualization of the apo-LXRα LBD shows that the 41.1˚ rotational dihedral angle of the Methionine 298 sidechain positions the sulfur atom and the Tryptophan 443 indole ring 6-H to form a pseudo hydrogen bond that secures the AF-2/H12 and H2 helices. The Histidine 421 imidazole sidechain projects at a ring angle of 85.9˚ perpendicular to the plane of the Tryptophan 443 indole sidechain, forming a strong N1-H bifurcated hydrogen bond between the pyrrole and benzene rings.

25B - Cognate-LXRα LBD: In the cognate-LXRα LBD, the 68.6˚ rotational dihedral angle of the Methionine 298 sidechain positions the sulfur atom to form weaker vdW interactions between the Tryptophan 443 indole ring 6-H and 7-H. The Histidine 421 imidazole sidechain projects at a ring angle of 73˚ to the plane of the Tryptophan 443 indole sidechain, maintaining the C2-H aromatic hydrogen bond to the indole benzene ring and transitioning the N1-H interaction into an aromatic hydrogen bond to the indole benzene ring.

2.10.6 In Silico LXRβ SAR: Minimized AF-2 Visualization

The LXRβ LBD exhibits significant structural differences in its apo state compared to LXRα. Methionine 312's sidechain is positioned at a rotational dihedral angle of 44.8˚, causing its sulfur atom to rest between the Tryptophan 457 indole ring 5-H and 6-H, leading to weak van der Waals packing interactions. Furthermore, the Histidine 435 imidazole sidechain is angled at a ring angle of 87.6˚, forming a C2-H bifurcated aromatic hydrogen bond with the pyrrole and benzene rings of Tryptophan 443 (**Figure 26A**).

Conversely, the cognate state of the LXRβ LBD exhibits structural changes compared to the apo state. Methionine 312's sidechain adopts a rotational dihedral angle of 60.7˚, resulting in its sulfur atom approaching an energetically favored pseudo hydrogen bond with the Tryptophan 443 indole ring 7-H. Additionally, the Histidine 421 imidazole sidechain is angled at a ring angle of 70.6˚ to the plane of the Tryptophan 443 indole sidechain, thus reinforcing the C2-H bifurcated aromatic hydrogen bond to the indole pyrrole and benzene rings (**Figure 26B**). These observations indicate a more dynamic nature of the LXRβ LBD and its ability to undergo conformational changes when ligand binding occurs, similar to LXRα, but with distinct structural characteristics that would suggest a distinction in substrate specificity between the two LXR isoforms.

Figure 26. 4NQA Minimized Apo-LXRβ LBD and 4NQA Cognate-LXRβ LBD Energy Visualization

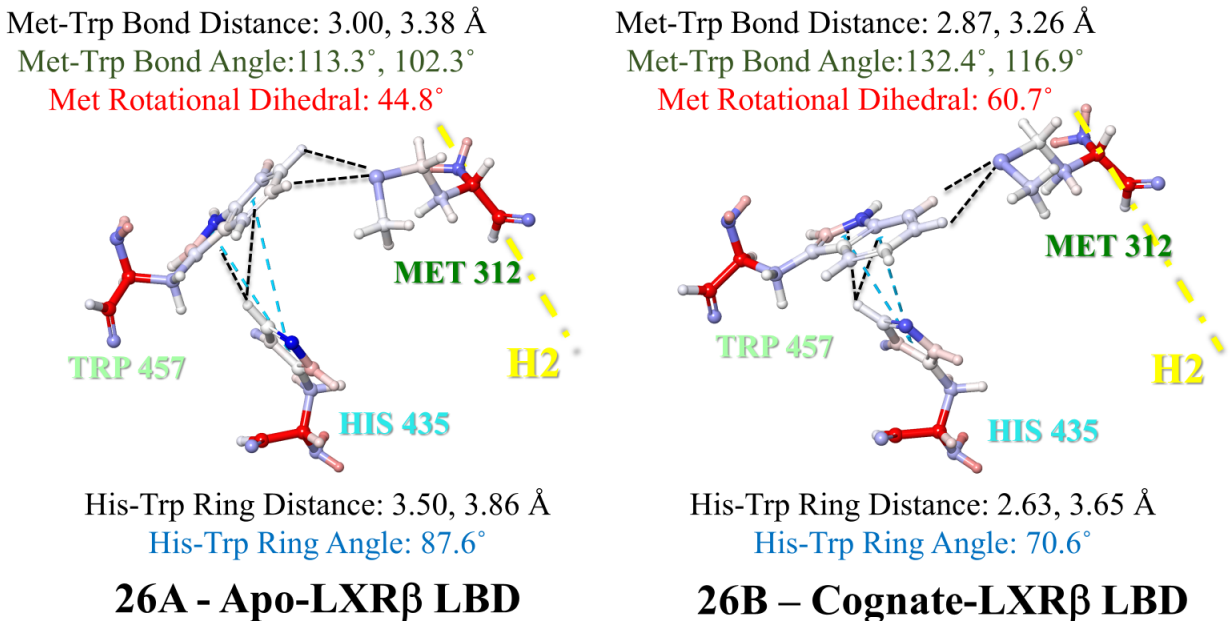

26A - Apo-LXRβ LBD: Energy visualization of the apo-LXRβ LBD shows that the 44.8˚ rotational dihedral angle of the Methionine 312 sidechain positions the sulfur atom between the Tryptophan 457 indole ring 5-H and 6-H to form weak vdW packing interactions. The Histidine 435 imidazole sidechain projects at a ring angle of 87.6˚ perpendicular to the plane of the Tryptophan 443 indole sidechain, forming a C2-H bifurcated aromatic hydrogen bond between the pyrrole and benzene rings.

26B - Cognate-LXRβ LBD: In the cognate-LXRβ LBD, the 60.7˚ rotational dihedral angle of the Methionine 298 sidechain positions the sulfur atom to approach an energetically favored pseudo hydrogen bond with the Tryptophan 443 indole ring 7-H. The Histidine 421 imidazole sidechain projects at a ring angle of 70.6˚ to the plane of the Tryptophan 443 indole sidechain, which strengthens the C2-H bifurcated aromatic hydrogen bond to the indole pyrrole and benzene rings.

2.10.7 In Silico LXRα SAR: Predicted Binding Pose Compound 7 (AU-403) LXRα LBD

The predicted mode of compound 7 (AU-403) with the LXRα LBD is determined by interactions with specific residues crucial in stabilizing the AF-2 region and influencing the conformational bias of coactivators and corepressors. Among these residues, Tryptophan 443 is the most important as it acts as a crucial contact site for the ligand, similar to the AF-2 Tyrosine residue observed in the PPAR LBDs. Methionine 298 and Histidine 421 also significantly secure the AF-2 by coordinating aromatic hydrogen bonding with Tryptophan 443. This leads to significant conformational changes in the LXRα AF-2, primarily driven by compensatory hydrophobic, aromatic, and weakly polar ligand contacts (**Figure 27.**).

In the case of AU-403, its meta-benzoic moiety forms charged contacts with Arginine 305 and accepts a hydrogen bond from Serine 264, guiding the dibenzylamine polar anchor point to donate a hydrogen bond to Threonine 302. Moreover, the benzoic acid aromatic ring creates a steric barrier that favors the shifting of the Methionine 298 sidechain's rotational dihedral angle to 64.2˚, preventing the formation of a pseudo-hydrogen bond with the Tryptophan 443 indole C7-H, which is indicative of a transition to an active state.

However, the 1,1-biphenyl ring system of AU-403 forms aromatic hydrogen bonds with Phenylalanine 257, 315, 326, and 335, thereby preventing extension into the AF-2 region. This interaction strengthens the bifurcated aromatic hydrogen bond between Tryptophan 443 and Histidine 421, which resembles the configuration observed in the apo-state. The ligand docking poses were generated based on the X-ray structure of the GW3965 synthetic agonist bound to LXR-alpha (PDB: 3IPQ).

Figure 27. Predicted Binding Mode of Compound 7 (AU-403) in LXRα LBD

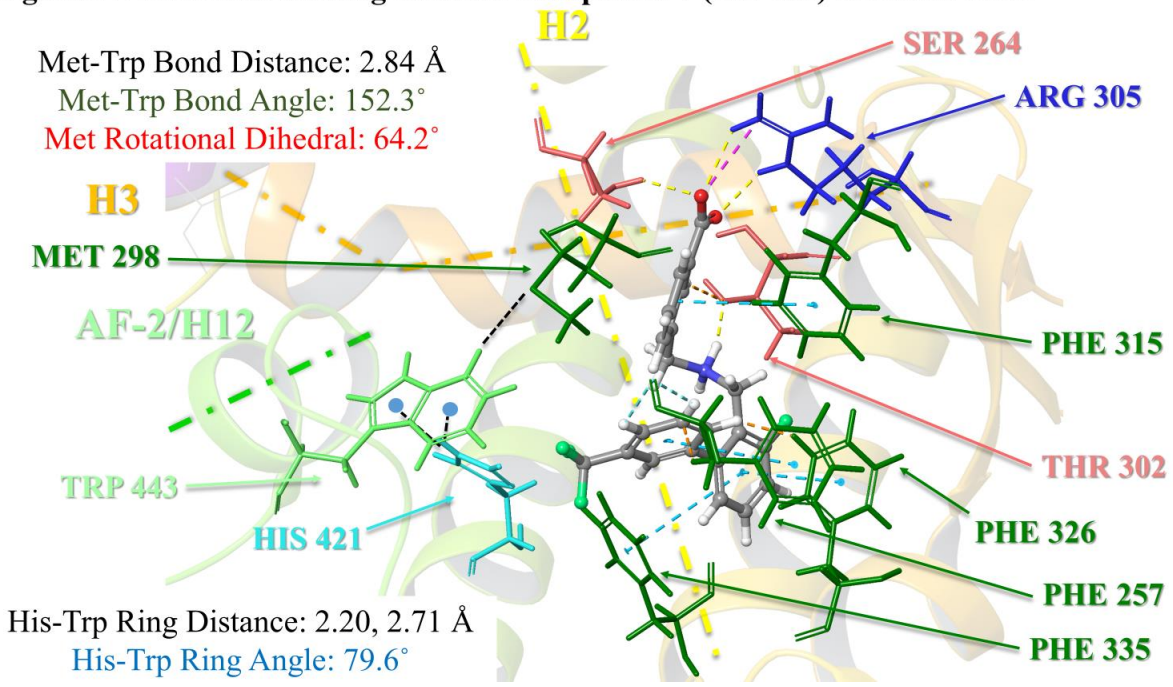

Predicted Binding Mode LXRα. The aromatic Tryptophan 443 residue is the critical ligand contact site that regulates LXRα AF-2 stability and coregulator conformational bias. The Methionine 298 and Histidine 421 residues secure the AF-2 through coordinated aromatic hydrogen bonding with Tryptophan 443. Consequently, the LXRα AF-2 undergoes major conformational changes as favorable ligand contacts are predominantly hydrophobic or aromatic. The meta-benzoic on compound 7 (AU-403) forms charged contacts to Arginine 305 and accepts a hydrogen bond from Serine 264, which directs the dibenzylamine polar anchor point to donate a hydrogen bond to Threonine 302. Additionally, the benzoic acid aromatic ring provides a steric barrier that favorably shifts the Methionine 298 sidechain rotational dihedral to 64.2˚ so that the sulfur atom can not form a pseudo hydrogen bond with the Tryptophan 443 indole C7-H, representing a transition to an active state. However, the AU-403 1,1-biphenyl ring system forms aromatic hydrogen bonds to Phenylalanine 257, 315, 326, and 335, preventing extension into the AF-2, which strengthens the Tryptophan 443 and Histidine 421 bifurcated aromatic hydrogen bond, as observed in the apo-state. Ligand docking poses were generated using the PDB: 3IPQ – X-ray structure of GW3965 synthetic agonist bound to LXR-alpha.

2.10.8 In Silico LXRβ SAR: Predicted Binding Pose of Compound 7 (AU-403) LXRβ LBD

The selectivity for LXRβ observed with compound 7 (AU-403) has been attributed to the specific molecular interactions between the ligand and critical residues within the LXRβ LBD that promote a selective conformational bias, similar to the predicted binding poses generated with PPARα and PPARδ. By targeting key residues unique to LXRβ, AU-403 demonstrates a preference for this isoform, offering potential therapeutic advantages in modulating LXRβ-mediated cholesterol efflux pathways while minimizing off-target effects on LXRα (**Figure 28.**).

LXRβ and LXRα exhibit distinct binding characteristics due to differences in residue composition and conformational preferences. AU-403 interacts with residues unique to the LXRβ AF-2 region in the predicted binding mode. The meta-benzoic acid moiety of AU-403 forms a hydrogen bond with Serine 278 in LXRβ, a residue contact absent in LXRα. This interaction positions AU-403 to adopt an active conformation within the LXRβ LBD by limiting potential charged contacts with Arginine 319 and enabling the ligand's hydrophobic tail extension into the AF-2 pocket.

Moreover, the specific arrangement of the 1,1-biphenyl ring system in AU-403 is equally crucial in enhancing selectivity for LXRβ. This ring system forms unique aromatic hydrogen bonds with residues Threonine 272 and Phenylalanine 271, differing from the corresponding interactions observed in LXRα. The induced steric strain caused by the 1,1-biphenyl ring system strengthens interactions with residues like Histidine 435, promoting a conformational shift in the AF-2 region towards the active state.

The observed selectivity for LXRβ with AU-403 highlights the importance of understanding the molecular interactions that govern ligand-receptor binding, as these interactions

are critical in determining selectivity for this isoform. Specific modulation of LXR-mediated pathways by AU-403 offers a novel therapeutic approach for treating AD and associated metabolic disorders such as atherosclerosis and diabetes in the paradigm of APOE4-associated deficits.

In conclusion, the selectivity for LXRβ with AU-403 is a significant advancement in drug discovery. The molecular insights gained from this study will aid in developing more selective LXRβ agonists, which could have far-reaching clinical implications. This research underscores the importance of a detailed understanding of the molecular interactions that govern ligand-receptor binding in drug design.

Figure 28. Predicted Binding Mode of Compound 7 (AU-403) in LXRβ LBD

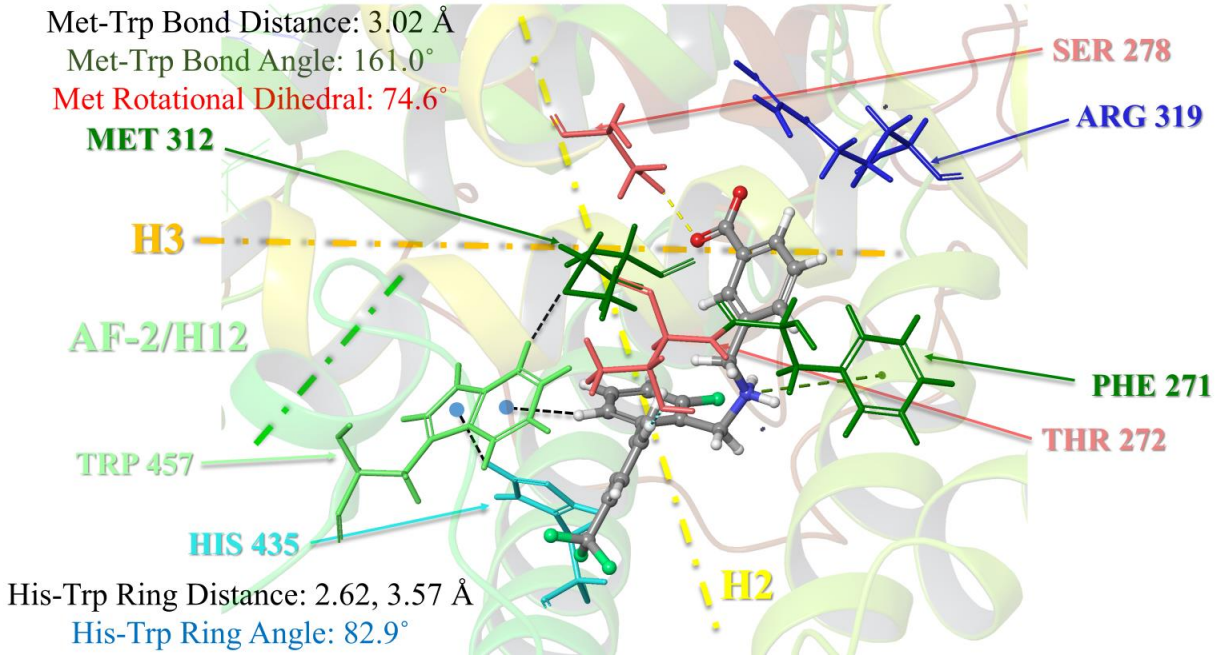

Predicted Binding Mode LXRβ. The Tryptophan 457 residue is an important contact site that regulates LXRβ AF-2 stability, just like LXRα. The meta-benzoic acid on compound 7 (AU-403) accepts a hydrogen bond from Serine 278, which limits a potential charged contact to Arginine 319, and allows further extension of the hydrophobic tail into the AF-2. The 1,1-biphenyl ring system on AU-403 forms an aromatic hydrogen bond with Threonine 272, in place of the LXRα preferred Phenylalanine contacts as the dibenzylamine polar anchor point is aligned to form an aromatic hydrogen bond with Phenylalanine 271. This alignment causes the 1,1-biphenyl ring system to provide steric strain that strengthens the Histidine 435 imidazole C2-H aromatic hydrogen bond with the Tryptophan 457 pyrrole ring, as a 4-fluoro-1,1-biphenyl 6-H aromatic hydrogen bond contact to the Tryptophan 457 benzene ring takes the place of the apo state Histidine-Tryptophan bifurcated aromatic hydrogen bond. This shift repositions the aromatic hydrogens in the plane of the Tryptophan indole ring to approximate a pseudo-hydrogen bond with the Methionine 312 sulfur atom, thus shifting the AF-2 conformation to resemble the cognate active state. Ligand docking poses were generated using the PDB: 4NQA – Crystal structure of liganded hRXR-alpha/hLXR-beta heterodimer on DNA.

2.10.9 In Silico LXRα SAR: Predicted Binding Pose of Compound 15d in the LXRα LBD

The specific modulation of LXR isoforms has emerged as a promising area for drug discovery. This would allow drug designs to specifically target individual biological pathways associated with each isoform. In particular, a ligand that acts as an agonist for LXRβ but an inverse agonist for LXRα could offer several advantages.

Firstly, it enables selective targeting to avoid potential off-target effects and improve therapeutic outcomes by activating or inhibiting desired pathways. Secondly, such selectivity may help to reduce side effects associated with systemic LXR activation, especially undesirable effects linked to hepatic LXRα activation, like hepatic lipogenesis and hypertriglyceridemia. Thirdly, differential modulation of LXR isoforms allows for versatile therapeutic applications, making it possible to address conditions associated with impairments in lipid transport observed in AD, atherosclerosis, and related metabolic disorders where LXRβ activation specifically regulates cholesterol efflux, thus minimizing adverse effects while stimulating an immune response to clear pathogenic material. Moreover, this rational drug design aligns with the principles of precision medicine. This emerging field focuses on developing personalized treatments tailored to individual patients based on their specific disease subtype or genetic makeup. This approach also promises to develop safer and more effective therapies across various metabolic diseases.

Compound 7 (AU-403) was subjected to manual iterative ligand structural optimization to increase extension into the LXRβ AF-2 region by adding a benzyl aromatic ring moiety to enhance binding energy through aromatic hydrogen bonds and pi-pi stacking interactions. The unique conformational selectivity observed with the AU-403 3-(aminomethyl)benzoic acid moiety, which

conferred a distinct PPAR activation profile, was subsequently observed in LXR; thus, this feature was maintained.

In the predicted binding mode for LXRα, the meta-benzoic acid moiety of the lead derivative forms a single charged contact with Arginine 305. This interaction strategically positions the aromatic hydrogens to sterically hinder the charge clamp formed between Glutamate 267 and Arginine 305, stabilizing the ligand-receptor complex. Moreover, the 1,1-biphenyl ring system of the lead derivative engages in pi-pi stacking interactions with Phenylalanine 326. At the same time, the polar anchor point dibenzylamine forms a hydrogen bond with the sulfur atom of Methionine 298 (**Figure 29.**).

Significantly, the ligand's hydrogen bonding interaction with Methionine 298 induces a conformational change in the sidechain methyl group, orienting it in a flipped-up position above the plane of the Tryptophan 443 indole ring. This repositioning of Methionine creates a steric barrier that prevents the Tryptophan AF-2 region from transitioning to an active conformation. Furthermore, the 3-fluorophenyl aromatic ring of the lead compound aligns perpendicular to the plane of the Histidine 421 imidazole ring, facilitating favorable vdW packing interactions.

Figure 29. Predicted Binding Pose of Compound 15d in the LXRα LBD

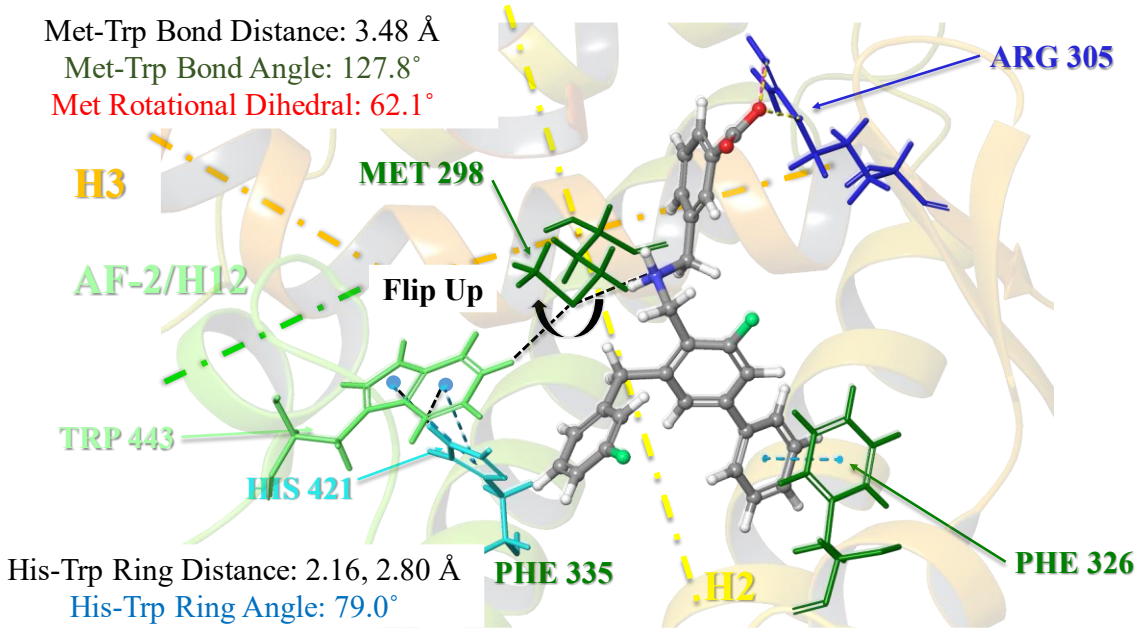

Predicted Binding Mode LXRα. The compound 15d meta-benzoic acid forms a single charged contact to Arginine 305 which positions the aromatic hydrogens to sterically hinder the Glutamate 267-Arginine 305 charge clamp. The lead compound's 1,1-biphenyl ring system preferentially forms a pi-pi stacking interaction with Phenylalanine 326 as benzylamine's polar anchor point forms a hydrogen bond to the Methionine 298 sulfur atom. The ligand hydrogen bond to Methionine 298 conformationally positions the residue sidechain methyl group in a flipped-up position above the plane of the Tryptophan 443 indole ring, thus providing a steric barrier to an active conformation. Additionally, the lead compound's 3-fluorophenyl aromatic ring positions perpendicular to the plane of the Histidine 421 imidazole ring to form favorable vdW packing interactions that strengthen the intramolecular AF-2 Tryptophan bifurcated hydrogen bonds. Ligand docking poses were generated using the PDB: 3IPQ – X-ray structure of GW3965 synthetic agonist bound to LXR-alpha.

2.10.10 In Silico LXRβ SAR: Predicted Binding Pose of Compound 15d in the LXRβ LBD

In the LXRβ LBD, the full lead derivative from compound 12d forms coordinated interactions, including ionic, ion-dipole, and hydrogen bond interactions between Serine 278 and Arginine 319 (**Figure 30.**). This leads to a unique conformational change in the charge clamp, pulling it towards the interior of the receptor site. As a result, the hydrogen bond between the H1 Asparagine 239 and Arginine 319 is lost.

On the other hand, in the LXRα LBD, a similar charge clamp disruption was observed, but it was predominantly caused by the ligand's interaction with Glutamate 267 and Arginine 305. The ligand's polar anchor point, dibenzylamine, adopts a distinct conformational inversion in the LXRβ LBD, as it positions the alpha benzyl hydrogens to sterically hinder the Methionine 312 sulfur atom contact, instead favoring a hydrogen bond donation to Threonine 302. This differs from the LXRα LBD, where the polar anchor point of the dibenzylamine formed a hydrogen bond with Glutamine 223 (**Figure 29.**).

Additionally, in the LXRβ LBD, the ligand's 3-fluorophenyl-1,1-biphenyl ring system forms several pi-pi and aromatic hydrogen bond interactions with the Phenylalanine 329, 340, and 349 residues in an inverse binding position compared to what was predicted in the LXRα LBD. In contrast, the LXRα LBD's ligand biphenyl ring system primarily interacted with Phenylalanine 257, 315, 326, and 335.

The inverse binding mode observed in the LXRβ LBD enables the ligand's 1,1-biphenyl benzene ring to be positioned perpendicular to the Histidine 435 imidazole ring, facilitating an active conformation of the His-Trp ring angle. This differs from the LXRα LBD, where the ligand's biphenyl benzene ring formed a pi-pi stacking interaction with Phenylalanine 326.

Figure 30. Predicted Binding Pose of Compound 15d in the LXRβ LBD

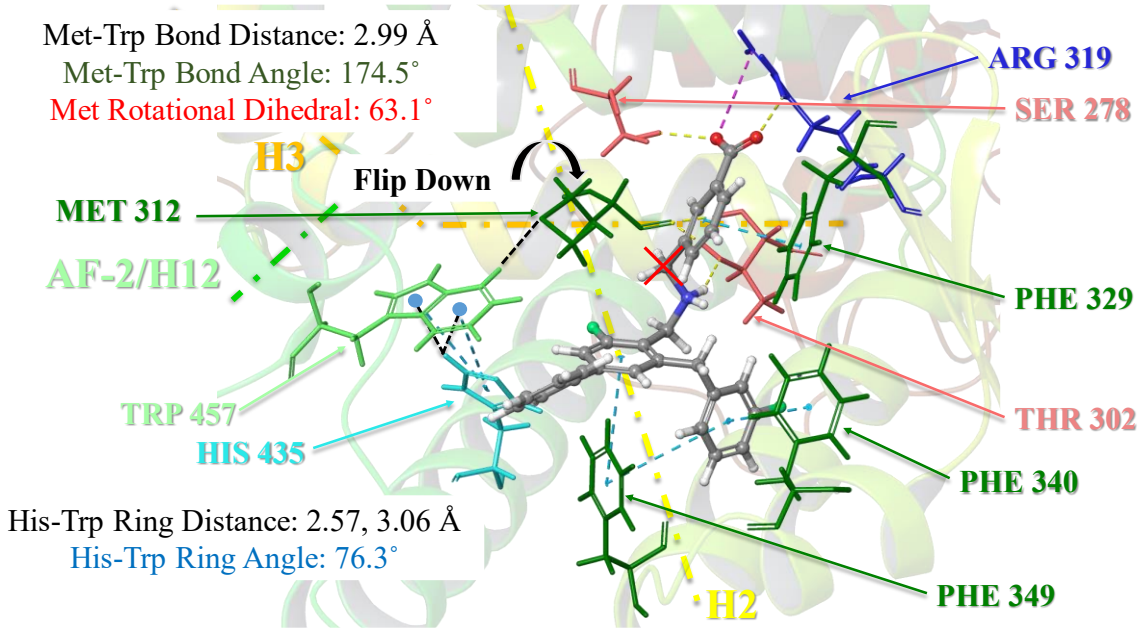

Predicted Binding Mode LXRβ. The compound 15d meta-benzoic acid forms multiple coordinated interactions, including ionic, ion-dipole, and hydrogen bond interactions between Serine 278 and Arginine 319. This results in the charge clamp being pulled towards the interior of the receptor site, as the hydrogen bond between the H1 Asparagine 239 and Arginine 319 is lost. The ligand's polar anchor point, benzylamine, is aligned so that the benzyl hydrogens can block potential contacts with the Methionine 312 sulfur atom, instead preferring to donate a hydrogen bond to Threonine 302. This positioning helps the 3-fluorophenyl-1,1-biphenyl ring system to form several pi-pi and aromatic hydrogen bond interactions with the Phenylalanine 329, 340, and 349 residues in an inverse binding position compared to what was predicted in the LXRα LBD. This inverse binding mode also enables the ligand's 1,1-biphenyl benzene ring to be positioned perpendicular to the Histidine 435 imidazole ring, allowing the His-Trp ring angle to adopt an active conformation. Ligand docking poses were generated using the PDB: 4NQA – Crystal structure of liganded hRXR-alpha/hLXR-beta heterodimer on DNA.

Chapter 3: Conclusions and Future Directions

In summary, this research project has described the results obtained from a CADD-assisted rational drug design of AU-403, a novel PPAR α/δ agonist for clinical application in AD patients. Throughout the course of this study, a panel of representative PPAR and LXR agonists were used to provide experimental feedback that guided in silico predictions and interpretation. These representative agonists were chosen based on factors of target selectivity and the consequence of physiochemical properties associated with known toxicities. This study revealed that nuclear receptor selectivity based on strong binding and low EC_{50} values presented inherent problems with ADME-associated toxicities. The hydrophobic nature of the PPARδ LBD demonstrates this problem effectively as this class of drug has failed to reach clinical testing as they commonly display excessively lipophilic chemical structures prone to be poorly bioavailable with limited therapeutic efficacy. Similarly, LXR nuclear receptor agonists display the same tendencies due to strong binding interactions to hydrophobic receptor sites, which are representative of the endogenous oxysterol substrates.

Uniquely, the AU-403 chemical structure revealed a distinct conformational bias as a means of PPARα/δ selectivity and, most importantly, a novel meta-substituted aminomethyl benzoic acid binding moiety that displays ideal ADME physiochemical properties for greater drug tolerability and therapeutic application. Interestingly, AU-403 exhibited a similar conformational bias that conferred LXRβ selectivity. The initial derivatization of the LXRβ selective leads was based on previous observations with the PPAR receptors, where it was hypothesized that ligand contacts to the AF-2 were dependent on strong interactions for activation. However, on in silico re-evaluation of AU-403 and subsequent LXRβ selective leads, it would appear that this initial

hypothesis was incorrect. Intriguingly, aspects of AU-403 PPARδ conformational selectivity appear to overlap with the same observations for LXRβ conformational selectivity, conferring potential substrate overlap.

The concept of lock and key is used as a simple analogy to explain the importance of stereochemistry in the molecular recognition process. This analogy illustrates how specific molecules, like enzymes and receptors, bind to particular ligands or substrates by recognizing their complementary shapes and chemical features. For successful binding to occur, the ligand or substrate must have a compatible shape, stereochemistry, and chemical functional groups with those of the binding site. This ensures that only specific molecules with the correct "key" can interact with and bind to the receptor or enzyme, much like only the correct key can open a particular lock.

Stereochemistry also plays a significant role in drug pharmacokinetics and pharmacodynamics, affecting bioavailability, metabolic stability, and therapeutic activity. Furthermore, understanding stereochemistry is essential for predicting and managing adverse effects, as enantiomers may have distinct pharmacological and safety profiles. Regulatory agencies usually require the characterization and evaluation of stereoisomers in drug development to ensure safety and efficacy.

Endogenous substrates that activate PPARs include various molecules derived from lipids, such as fatty acids, oxidized lipids, and eicosanoids. These molecules often have multiple stereocenters, resulting in different stereoisomers with distinct biological activities and interactions with PPARs. Stereochemistry plays a critical role in the spatial arrangement of functional groups within these molecules, affecting their binding affinity, selectivity, and biological effects on PPARs.

For instance, the stereochemistry of fatty acids, particularly at the alpha carbon, which is adjacent to the carboxylic acid moiety, impacts their ability to activate PPARs. Saturated and unsaturated fatty acids with specific stereochemical configurations have been shown to selectively activate different PPAR isoforms, which leads to varying effects on metabolic pathways and gene expression.

Moreover, endogenous lipid mediators, such as prostaglandins, leukotrienes, and various metabolites of polyunsaturated fatty acids, exhibit stereospecific interactions with PPARs to regulate intracellular signaling in response to lipid metabolism and energy homeostasis. Certain stereoisomers of these lipid mediators have been reported to modulate PPAR activity and downstream signaling pathways involved in inflammation, immune response, and lipid metabolism.

Similarly, LXRs are essential in lipid metabolism related to cholesterol homeostasis, lipid metabolism, and inflammation. Oxysterols, oxidized cholesterol derivatives, serve as endogenous ligands for LXRs. The oxidation state and stereochemistry of the oxysterol molecule determine its ability to bind to LXRs with specificity and selectivity. Certain oxysterol stereoisomers are reported to exhibit higher LXR isoform affinity and selectivity for LXRs compared to others, influencing their ability to activate LXR signaling pathways.

Activation of LXRs by their endogenous ligands results in pronounced transcriptional changes in gene expression. These changes profoundly impact various cellular functions, including metabolism, lipid balance, and immune response. One of the primary benefits of LXR activation is the transportation of cholesterol in the opposite direction, reducing cholesterol absorption, lowering the production of fats, and increasing insulin sensitivity. Moreover, LXRs play a crucial role in regulating the response to inflammation in the immune

system.

The study of lipid mediators and oxysterols is immensely significant in various biological pathways. However, identifying, isolating, and characterizing these molecules is challenging due to their structural diversity and complexity. The transient nature of lipid mediator signaling and the low abundance of oxysterols in biological systems further complicate their study. The multifaceted roles played by these molecules in cellular signaling, inflammation, metabolism, and immune regulation require interdisciplinary approaches and advanced analytical techniques for comprehensive investigation. Furthermore, the dynamic interplay between lipid mediators, oxysterols, and other signaling molecules adds another layer of complexity to unraveling their biological functions. Despite these challenges, ongoing research efforts increasingly recognize the importance of lipid mediators and oxysterols in health and disease, highlighting the need for further exploration to elucidate their roles in physiological and pathological processes.

Evaluating hormones solely based on blood levels is a complex task. Several factors make it challenging. Hormone secretion follows diurnal rhythms, varying levels throughout the day. Feedback mechanisms further complicate hormone regulation, as changes in hormone levels trigger feedback loops that modulate further hormone production. Hormones can also circulate and be bound to carrier proteins, with only the free fraction having biological activity. Metabolism and clearance processes, along with individual variability influenced by genetics, age, sex, and health status, also affect hormone levels. Therefore, interpreting hormone blood tests requires careful consideration of clinical context, symptoms, and additional diagnostic tests for a comprehensive assessment of endocrine function.

Hormones have numerous and diverse effects on AD. Insulin dysregulation and resistance impact glucose metabolism and contribute to the buildup of Aβ plaques and NFTs, central to AD

pathology. Sex hormones like estrogen and testosterone play a neuroprotective role, with decreasing levels correlating with increased AD risk. Thyroid hormone dysfunction may affect Aβ production and tau phosphorylation, while stress hormones like the well-known oxysterol metabolite cortisol aggravate neuroinflammation and oxidative stress in AD.

Recent research has suggested that chronic stress and dysregulation of the hypothalamic-pituitary-adrenal (HPA) axis are major contributors to AD pathogenesis. The HPA axis regulates cortisol secretion, and when cortisol levels are elevated, they can promote the accumulation of Aβ plaques and NFTs. Moreover, recent studies have indicated that cortisol can trigger the excessive phosphorylation of tau proteins, negatively impacting synaptic plasticity and increasing neuronal apoptosis. These biological effects of cortisol have been identified as potential contributors to the cognitive impairment and neurodegenerative processes associated with AD. Additionally, stress-related factors, such as glucocorticoid receptor dysregulation, oxidative stress, and neuroinflammation, can also exacerbate AD pathology and accelerate disease progression.

These findings suggest that chronic stress and HPA axis dysfunction could be pivotal in the development and progression of AD. They paint a clearer picture of the disease's pathophysiology by promoting the accumulation of Aβ plaques and tau tangles, disrupting synaptic plasticity, and increasing neuronal apoptosis. This understanding is a crucial step towards developing innovative therapeutic applications like LXRβ selective agonists, offering a glimmer of hope in the fight against AD. Intriguingly, LXRβ activation plays a crucial role in the innate immune response through the regulation of APOE.

In addition to its metabolic function, APOE helps clear waste products such as cellular debris, aggregated proteins, and lipids from the brain by phagocytosis through microglia and other immune cells. The efficiency of this process varies with the APOE isoform—the APOE2 and

APOE3 isoforms are more efficient than the APOE4 isoform. In individuals carrying the APOE4 allele, the impaired clearance of Aβ fibrils and other pathological aggregates by microglia may contribute to the progression of AD pathology.

Therefore, the conformational bias observed in the AU-403 predictive poses suggests a unique stereochemical requirement to access the PPAR and LXR isoforms that has major clinical implications for furthering our understanding of the complex dynamics associated with hormone signaling and AD. The AU-403 chemical structure and subsequent derivatives were designed according to in silico predictive ADME toxicity filters that follow the "Rule of Five," also known as Lipinski's Rule of Five, a set of guidelines used in drug discovery and development to assess the potential for a compound to be orally bioavailable and to have favorable pharmacokinetic properties. The results obtained from physiochemical experimental determination of the AU-403 chemical structure and reference structures were in good agreement with in silico predicted ADME toxicity assessments.

In conjunction with experimental functional activity, a remarkable amount of information was gathered to evaluate the synergistic effects associated with a mixed panel of PPAR and LXR agonists, which was carried out to assess the accuracy of in silico predictions. Therapeutic options for patients and families suffering from the debilitating effects of AD and associated dementias remain limited. However, effective CADD-assisted drug discovery strategies are being developed in response to the information gathered from the AU-403 study. Future work will explore the association of the various forms of oxysterols and their association with gene regulation, as well as cross-correlating lipidomic and transcriptomic studies, to understand the impact of LXRβ selective modulation on hormone signaling and AD.

Chapter 4: Experimental Section

4.1 Compound 7 (AU-403) Synthetic Scheme 1.

General Methods 3-fluoro-3'-(trifluoromethyl)-[1,1'-biphenyl]-2-carbaldehyde (3).

K_3PO_4 (21.0 g, 99 mmol; 2 eq.) and TBAB (15.9 g, 49.3 mmol; 1 eq.) were combined into a round bottom flask (RBF) and mixed with purified water (24 mL) under sonication. 2-bromo-6-fluorobenzaldehyde (**1**) (10.0 g, 49.3 mmol; 1 eq.) and 2-trifluoromethyl)phenylboronic acid (**2**) (9.4 g, 49.3 mmol; 1eq.) were dissolved separately in THF (48 mL). The THF mixture was combined with the aqueous suspension and stirred vigorously at 60˚ C. Pd(OAc)2 (0.1 g, 0.5 mmol; 0.01 eq.) was added to the reaction solution and stirred for twelve hours. The THF layer was decanted from the aqueous suspension. The aqueous suspension was diluted with petroleum ether (150 mL) and filtered with a Buchner funnel. The petroleum ether and THF layers were combined and then filtered through a silica plug, dried over sodium sulfate, and concentrated under reduced pressure to give 12.7 g of the expected product (**3)** as a light-yellow viscous liquid at room temperature (yield = 96%). $C_{14}H_8F_4O$. MS(EI) m/z: 268.1. ^{1}H NMR (399 MHz, cdcl$_3$) δ 7.18 (d, *J* = 1.1, 7.7 Hz, 1H), 7.20 – 7.25 (d, 1H), 7.50 (d, *J* = 1.6, 7.7 Hz, 1H), 7.54 – 7.59 (t, 1H), 7.59 – 7.61 (m, 1H), 7.61 – 7.64 (t, 1H), 7.68 (d, *J* = 0.9, 7.7 Hz, 1H), 10.06 (s, 1H).

Methyl 3-(aminomethyl)benzoate (5).

3-(Aminomethyl)benzoic acid hydrochloride (2.0 g, 10.6 mmol; 1 eq.) was dissolved in anhydrous MeOH and cooled in an ice bath. Thionyl chloride (1.6 g, 13.3 mmol; 1.2 eq.) was added dropwise to the cooled reaction solution and stirred for twelve hours. The solvent was then

removed under reduced pressure to yield the amine hydrochloride salt as a white powder. Before the reductive amination reaction in **Figure 10.c**, the amine hydrochloride salt was neutralized in a minimal volume of aqueous 1.0 M NaOH. The neutral amine was extracted from the alkaline aqueous solution using chloroform or DCM and concentrated under reduced pressure.

Methyl 3-[{{[3-fluoro-3'(trifluoromethyl)-[1.1'-biphenyl]-2-yl]methyl}amino}methyl]benzoate (6).

(i) Compounds 5 (6.3 g, 37.7 mmol; 1 eq.) and **3** (10.1 g, 37.7 mmol; 1 eq.) were added to an RBF and dissolved in DCE (30 mL) with constant stirring for three hours. The solvent was removed under reduced pressure to yield the imine intermediate.

(ii) The imine intermediate was redissolved in anhydrous MeOH (30 mL) at 50°C followed by incremental addition of $NaBH_4$ (0.3 g, 9.4 mmol; 0.25 eq.). The solvent was removed under reduced pressure, and the residue was taken up with ethyl acetate (50 mL). The organic phase was washed with a saturated bicarbonate solution (25 mL), dried on sodium sulfate, and filtered. The solvent was removed under reduced pressure to yield a translucent viscous liquid. The liquid obtained was purified on silica gel using a hexane/ethyl acetate (80:20; v/v) mixture as the eluent to give 14.1 g of the expected product **6** as a clear, viscous liquid (yield = 90%). $C_{23}H_{19}F_4NO_2$. MS(EI) m/z: 416.2. ^{1}H NMR (399 MHz, dmso) δ 2.46 (s, 1H), 3.51 (s, 2H), 3.69 (s, 2H), 3.83 (s, 3H), 7.15 (d, *J* = 7.7 Hz, 1H), 7.25 (t, *J* = 8.3, 9.7 Hz, 1H), 7.36 (d, *J* = 14.6 Hz, 1H) 7.34 – 7.43 (m, 2H), 7.45 (d, 1H), 7.60 (t, *J* = 7.6 Hz, 1H), 7.71 (d, *J* = 7.1 Hz, 1H), 7.76 (d, *J* = 7.1 Hz, 1H), 7.86 (s, 1H), 7.92 (s, 1H). ^{13}C NMR (100 MHz, dmso) δ 43.7, 52.4, 52.5, 52.8, 65.3, 115.2, 124.6, 125.3, 125.5, 125.9, 127.9, 129.0, 129.3, 129.6, 129.9, 133.1, 133.5, 140.8, 141.5, 143.0, 160.7, 163.1, 166.7.

{{[3-fluoro-3'-(trifluoromethyl)-[1,1'-biphenyl]-2-yl]methyl}amino}methyl]benzoic acid (7).

Compound **6** (1.0 g, 2.4 mmol) was dissolved in methanol (10 ml) and mixed with a NaOH solution (50% w/v, 1 mL), followed by stirring for twelve hours at room temperature. The solvent was removed under reduced pressure to yield an off-white residue. The residue was washed with petroleum ether (25 mL) and dried under nitrogen gas to yield a white solid. The solid was neutralized with 1.0 M HCl (5 mL) and extracted thrice with ethyl acetate (25 mL). Organic phases were combined and dried over sodium sulfate, and the solvent was removed under reduced pressure to yield 700 mg of compound **7** as a white powder. (yield = 80%). $C_{22}H_{17}F_4NO_2$. MS m/z: 404.1266 $[M+H]^+$. ^1H NMR (399 MHz, dmso) δ 2.04 (s, 1H), 3.6 (s, 2H), 3.76 (s, 2H), 7.13 (d, *J* = 7.7 Hz, 1H), 7.26 (t, *J* = 8.3, 9.7 Hz, 1H), 7.14 – 7.20 (m, 1H), 7.32 (t, *J* = 7.7 Hz, 1H), 7.36 (t, *J* = 7.7 Hz, 1H), 7.37 – 7.48 (m, 2H), 7.56 (t, *J* = 7.8 Hz, 1H), 7.68 - 7.72 (m, 2H), 7.76 (d, *J* = 7.7 Hz, 1H), 7.81 (d, *J* = 7.7 Hz, 1H).

4.2 AU-403 LXRβ Selective Derivatives Synthetic Scheme 2.

Methyl 4-bromo-2-fluoro-6-methylbenzoate (9).

4-Bromo-2-fluoro-6-methylbenzoic acid (**8**) (9.3 g, 42.9 mmol; 1 eq.) and Cs_2CO_3 (28.0 g, 85.8 mmol; 2 eq.) were dissolved in DMF (30 mL) with subsequent dropwise addition of iodomethane (7.1 g, 3.1 mL, 47.2 mmol; 1.1 eq.). The reaction was stirred for three hours and then filtered. The filtrate was diluted in petroleum ether (85 mL), washed five times with brine, and then dried over sodium sulfate. It was then filtered through a silica plug, and the solvent was removed under reduced pressure to yield 9.3 g of compound **9** as a pale-clear viscous liquid. (yield = 87%). $C_8H_6BrFO_2$. MS(EI) m/z: 246.0, 248.0. ^{1}H NMR (399 MHz, cdcl$_3$) δ 2.38 (s, 3H), 3.92 (s, 3H), 7.13-7.15 (m, 1H), 7.19 (s, 1H).

Methyl 2-fluoro-6-methyl-4-(pyridine-3-yl)benzoate (10a).

3-Pyridylboronic acid (2.5 g, 20.2 mmol; 1 eq.), **9** (5 g, 20.2 mmol; 1 eq.), and Cs_2CO_3 (19.7 g, 60.5 mmol; 3 eq.) were mixed in alumina-filtered DMF (40 mL) heated to 80°C. Nitrogen gas was delivered via a cannula needle and stirred vigorously for thirty minutes. Tetrakis(triphenylphosphine)palladium (0.2 g, 0.2 mmol; 0.01 eq.) was added, and vigorous stirring was continued for an additional eight hours. The reaction was allowed to cool, filtered, and diluted with ethyl acetate (200 mL) five times. The mixture was washed four times with a brine solution (50 mL), dried on sodium sulfate, and filtered through a silica plug. This was concentrated under reduced pressure to yield the desired product as a yellow crude solid. The crude solid was purified on silica gel using a petroleum ether/ethyl acetate (50:50; v/v) mixture to afford 1.9 g of product **10a** as a pale-yellow powder. (yield = 62%). $C_{14}H_{12}FNO_2$. MS(EI) m/z: 245.1. ^{1}H NMR

(399 MHz, cdcl$_3$) δ 2.49 (s, 3H), 3.96 (s, 3H), 7.17 (m, *J* = 1.7, 10.5 Hz, 1H), 7.23 (s, 1H), 7.38 (dd, *J* = 4.8, 7.9 Hz, 1H), 7.85 (dt, *J* = 2.1, 2.1, 7.9 Hz, 1H), 8.64 (dd, *J* = 1.7, 4.8 Hz, 1H), 8.83 (m, *J* = 1.5 Hz, 1H).

Compounds **6b-d** were synthesized similarly.

Methyl 2-fluoro-6-methyl-4-(pyridine-4-yl)benzoate (10b).

As described for **10a, 5** (1.8 g, 7.3 mmol; 1 eq.) and 4-pyridylboronic acid (1.1 g, 9.1 mmol; 1.25 eq.) were transformed to 1.8 g of the expected product **10b** as a pale-yellow powder. (yield = 72%). $C_{14}H_{12}FNO_2$. MS(EI) m/z: 245.1.

Methyl 2-fluoro-4-furan-3-yl)-6-methylbenzoate (10c).

As described for **10a**, **5** (4.3 g, 17.4 mmol; 1 eq.) and (furan-3-yl)boronic acid (1.95 g, 17.4 mmol; 1 eq.) were transformed to 3.2 g of the expected product **10c** as a white powder. Compound **10c** was purified on silica gel using a petroleum ether/ethyl acetate (70:30, v,v) mixture as the eluent. (yield = 79%). $C_{13}H_{11}FO_3$. MS(EI) m/z: 234.1. ^{1}H NMR (399 MHz, cdcl$_3$) δ 2.44 (s, 3H), 3.94 (s, 3H), 6.67 (dd, *J* = 0.9, 1.9 Hz, 1H), 7.05 (m, *J* = 0.6, 1.6, 10.8 Hz, 1H), 7.13 (m, *J* = 1.6 Hz, 1H), 7.49 (m, *J* = 1.7 Hz, 1H), 7.76 (dd, *J* = 0.9, 1.6 Hz, 1H).

Methyl 3-fluoro-5-methyl-[1,1'-biphenyl]-4-carboxylate (10d).

As described in **10a**, **5** (5.0 g, 20.2 mmol; 1 eq.) and phenylboronic acid (2.7 g, 22.3 mmol; 1.1 eq.) were transformed to 4.2 g of the expected product **10d** as white powder. Compound **10d** was purified on silica gel using a petroleum ether/ethyl acetate (90:10, v/v) mixture as the eluent.

(yield = 85%). $C_{15}H_{13}FO_2$. MS(EI) m/z = 244.1**.** ^{1}H NMR (399 MHz, cdcl$_3$) δ 2.49 (s, 3H), 3.96 (s, 3H), 7.18 (ddd, *J* = 0.6, 1.7, 10.9 Hz, 1H), 7.20 – 7.28 (m, 1H), 7.31 – 7.50 (m, 3H), 7.52 – 7.64 (m, 2H).

Methyl 2-(bromomethyl)-6-fluoro-4-(pyridine-3-yl)benzoate (11a).

NBS (1.5 g, 8.4 mmol) and **10a** (1.4 g, 5.6 mmol) were combined into dry DCE (10 mL). The reaction was heated to 75°C, and AIBN (0.4 g, 2.2 mmol) was added, then stirred for five hours. The reaction was allowed to reach room temperature and diluted five times with a petroleum ether/ethyl acetate (50:50, v/v) solvent mixture. The diluent was filtered through an alumina plug and concentrated under reduced pressure to yield 0.5 g of the expected product **11a** as a yellow solid. (yield = 30%). $C_{14}H_{11}BrFNO_2$. GC-MS(EI) m/z: 323.0, 325.0. ^{1}H NMR (399 MHz, cdcl$_3$) δ 2.54 (s, 2H), 4.01 (s, 3H), 7.21 (m, *J* = 10.2 Hz, 2H), 7.26 (s, 1H), 8.05 (t, *J* = 2.1, 2.1 Hz, 1H), 8.71 (dd, *J* = 2.1, 10.9 Hz, 2H).

Methyl 2-(bromomethyl)-6-fluoro-4-(furan-3-yl)benzoate (11b).

As described for **10a**, compound **10c** (1.1 g, 4.7 mmol; 1 eq.) was transformed to 0.95 g of the expected product **11b** as a dark-orange solid. (yield = 65%). $C_{13}H_{10}BrFO_3$. MS(EI) m/z: 312.1, 314.1. ^{1}H NMR (399 MHz, cdcl$_3$) δ 2.45 (s, 2H), 3.95 (s, 3H), 6.62 (d, *J* = 2.1 Hz, 1H), 7.14 – 7.26 (m, 1H), 7.45 – 7.56 (m, 1H), 8.10 (ddd, *J* = 1.3, 8.3, 11.1 Hz, 2H).

Methyl 3-(bromomethyl)-5-fluoro-[1,1'-biphenyl]-4-carboxylate (11c).

As described for **10a,** compound **10d** (3.2 g, 13.2 mmol; 1 eq.) was transformed to 3 g of the expected product **11c** as a white solid. (yield = 72%). $C_{15}H_{12}BrFO_2$. MS(EI) m/z = 322.0,

324.0. ^{1}H NMR (399 MHz, cdcl$_3$) δ 4.01 (s, 3H), 4.74 (s, 2H), 7.27 – 7.39 (m, 2H), 7.40 – 7.71 (m, 3H), 8.05 – 8.13 (m, 2H).

Methyl 2-benzyl-6-fluoro-4-pyridin-3-yl)benzoate (12a).

As described in **Figure 1. Scheme a**, compound **11a** (0.17 g, 0,5 mmol; 1 eq.) and phenylboronic acid (0.06 g, 0.5 mmol; 1 eq.) were transformed to 0.1 g of the expected product **12a** as an off-white powder. (yield = 68%). $C_{20}H_{16}FNO_2$. MS(EI) m/z: 321.2. ^{1}H NMR (399 MHz, cdcl$_3$) δ 2.47 (s, 2H), 3.95 (s, 3H), 7.19 (m, *J* = 1.6, 10.0 Hz, 1H), 7.23 (s, 1H), 7.26 (s, 1H), 7.36 – 7.53 (m, 3H), 7.58 – 7.63 (m, 2H), 8.02 (t, *J* = 2.2, 2.2 Hz, 1H), 8.82 (d, *J* = 2.2 Hz, 1H), 8.89 (d, *J* = 2.2 Hz, 1H).

Methyl 3-benzyl-5-fluoro-[1,1'-biphenyl]-4-carboxylate (12b).

As described in **Figure 1. Scheme a**, compound **11c** (0.5 g, 1.5 mmol; 1 eq.) and phenylboronic acid (0.2 g, 1.7 mmol; 1.1 eq) were transformed to 0.2 g of the expected product **12b** a white powder. (yield = 39%). $C_{21}H_{17}FO_2$. MS(EI) m/z: 320.1. ^{1}H NMR (399 MHz, cdcl$_3$) δ 3.87 (s, 2H), 4.00 (s, 3H), 7.24 (s, 1H), 7.27 (s, 1H), 7.29 – 7.62 (m, 6H), 8.03 (d, *J* = 1.4 Hz, 2H), 8.05 (dd, *J* = 0.7, 1.5 Hz, 2H).

Methyl 3-fluoro-5-[(2-fluorophenyl)methyl]-[1,1'-biphenyl]-4-carboxylate (12c).

As described in **Figure 1. Scheme a**, compound **11c** (0.5 g, 1.5 mmol; 1 eq.) and 2-fluorophenyl boronic acid (0.24 g, 1.7 mmol; 1.1 eq.) were transformed to 0.18 g of the expected product **12c** as a white powder. (yield = 35%). $C_{21}H_{16}F_2O_2$. MS(EI) m/z: 338.2. ^{1}H NMR (399

MHz, cdcl$_3$) δ 3.86 (s, 2H), 3.99 (s, 3H), 7.10 (ddd, *J* = 1.6, 7.6, 10.2 Hz, 1H), 7.14 – 7.40 (m, 6H), 7.41 – 7.48 (m, 2H), 7.56 – 7.61 (m, 2H).

Methyl 3-fluoro-5-[(3-fluorophenyl)methyl]-[1,1'-biphenyl]-4-carboxylate (12d).

As described in **Figure 1. Scheme a**, compound **11c** (0.5 g, 1.5 mmol; 1 eq.) and 3-fluorophenyl boronic acid (0.24 g, 1.7 mmol; 1.1 eq.) were transformed to 0.2 g of the expected product **12d** as a white powder. (yield = 40%). $C_{21}H_{16}F_2O_2$. MS(EI) m/z: 338.2. ^{1}H NMR (399 MHz, cdcl$_3$) δ 3.86 (s, 3H), 4.23 (s, 2H), 6.90 – 7.03 (m, 2H), 7.07 (ddq, *J* = 1.0, 1.0, 1.0, 2.1, 7.5 Hz, 1H), 7.17 (dd, *J* = 2.2, 12.1 Hz, 1H), 7.25 – 7.34 (m, 2H), 7.37 (ddt, *J* = 1.4, 1.4, 6.4, 8.1 Hz, 1H), 7.41 – 7.48 (m, 2H), 7.55 – 7.61 (m, 2H).

Methyl 3-fluoro-5-[(4-fluorophenyl)methyl]-[1,1'-biphenyl]-4-carboxylate (12e).

As described in **Figure 1. Scheme a**, compound **11c** (0.5 g, 1.5 mmol; 1 eq.) and 4-fluorophenyl boronic acid (0.24 g, 1.7 mmol; 1.1 eq.) were transformed to 0.3 g of the expected product **12e** as a white powder. (yield = 59%). $C_{21}H_{16}F_2O_2$. MS(EI) m/z: 338.2. ^{1}H NMR (399 MHz, cdcl$_3$) δ 3.86 (s, 3H), 4.19 (s, 2H), 7.04 (ddt, *J* = 1.4, 1.4, 8.1, 9.6 Hz, 2H), 7.17 (dd, *J* = 2.2, 12.1 Hz, 1H), 7.26 (ddt, *J* = 0.9, 0.9, 3.5, 8.1 Hz, 3H), 7.37 (ddt, *J* = 1.5, 1.5, 6.6, 8.2 Hz, 1H), 7.41 – 7.48 (m, 2H), 7.56 – 7.61 (m, 2H).

4.3 Chemical Spectroscopic Analyses

UV-VIS.

LogP and LogD assay samples were measured on a Thermo Scientific UV-Vis NanoDrop Spectrophotometer. Sample PAMPA assay well plates were measured using a Biotek Synergy HT Multi Plate Reader with Abs UV-Vis.

NMR.

^{1}H and ^{13}C NMR spectra were recorded on a Varian MR400. All ^{1}H chemical shifts are reported in δ relative to the residual solvent reference peak. ^{13}C chemical shifts are reported in δ relative to CDCl3 (center of triplet, δ 77.23) or relative to DMSO-d6 (center of septet, δ 39.51). The spin multiplicities are indicated by the symbols s (singlet), d (doublet), t (triplet), q (quartet), and m (multiplet).

GC-MS.

GC-MS was performed with an HP-5890 GC coupled with an HP-5970 mass selective detector (Hewlett Packard, Palo Alto, CA) using Helium (grade 5.0) as carrier gas. The mass spectrometer was operated on the electron impact (EI) mode using ionization voltage of 70 eV and a source temperature of 230°C. Samples were dissolved in HPLC grade acetonitrile (Fisher Scientific, NJ, USA) and manually introduced (1μL) individually.

Elemental Analysis.

Atlantic Microlabs, Norcross, Georgia, performed elemental analyses.

MestReNova (Mnova).

NMR and LC/GC/MS data processing, visualization, simulation, prediction, presentation, and analysis were carried out using an academic trial version of the MestReNova software package.

4.4 Molecular Modeling: PPARs and LXRs LBD.

All molecular modeling for the PPAR and LXR nuclear receptors was conducted using the methods described below, which can be referenced. Molecular modeling was performed using Schrodinger Software: Maestro version 13.9.132, MMshare Version 6.5.132, Release 2024-1, Platform Windows-x64. Descriptions of the molecular modeling were based on methods described in Schrodinger user manuals. All protein structures were obtained from the Protein Data Bank (PDB).

General Modeling.

The Schrodinger software suite was used to perform computational analysis of the interactions of AU9, GW0742, AMPH13 (PPARα) and Pio with their respective PPAR ligand binding domains. PDB cognate crystal structures were used to confirm ligand-receptor interactions. Ligand docking studies were performed to determine the most stable docking poses determined by the ligand docking scores, representing the free energy upon binding of the ligand to the proteins' active site. Using the lowest energy conformation, a model system was built to explore the molecular dynamics of this interaction using a simulated annealing technique. For comparison, a full PPARδ agonist, GW0742, was used to illustrate key differences in our compound's ability to achieve similar transcriptional activity in vitro.

Protein Preparation.

Molecular models for PPARδ, α, and γ were built using the cognate ligand conformation obtained from X-ray crystallographic structures of GW-0742 bound to the PPARδ LBD (PDB: 3TKM), AMPH13 bound to the PPARα LBD (PDB: 3VI8), and rosiglitazone bound to the PPARγ

LBD (PDB:5Y2O). Protein crystal structures were imported and prepared using the Maestro modeling software protein preparation workflow. In preprocessing of the protein structures, termini were capped and any missing chains were filled in using Prime. H-bond optimization was performed using PROPKA at a pH of 7.4. Lastly, restrained minimization was performed with convergence of heavy atoms to RMSD of 0.30 Å and deletion of all water molecules within 5 Å of the ligand utilizing the force field OPLS4.

Induced Fit Docking.

All ligands were prepared using LigPrep with the OPLS4 force field. Ligands were ionized at a pH of 7.4 ± 0.2 using Epik. Prepared ligands were then subjected to induced fit docking by selecting the centroid of the workspace ligand in each protein complex. Residues were refined within 5.0 Å of ligand poses. Glide re-docking was performed using standard precision. Each ligand's lowest energy docking score was evaluated and used for further molecular modeling experiments.

Model System Generation for Molecular Dynamics.

Model systems were built from the best induced fit docking poses using a predefined simple point-charge (SPC) water solvent model. An orthorhombic box shape was chosen with a salt concentration of 0.15 M. The model system was built with the force field OPLS4. Simulated annealing and/or molecular dynamics were used to evaluate conformational stability. Simulated annealing: Simulation parameters were set to have a schedule of seventeen temperature changes over the course of 1.2 ns using an NVT ensemble class at 1.01325 bar. Model systems were relaxed

before the simulation. Molecular Dynamics: Simulation parameters were set at a temperature of 310 K for 100 ns at 1.01325 bar.

SiteMap Analysis.

SiteMap calculations were performed using the Schrodinger Maestro Suite. The Task setting was selected to evaluate a single binding site region plus a 6 Å buffer. The centroid of the cognate ligand was used as the reference point. Settings were selected to require at least 15 site points per reported site and report up to 5 sites. The more restrictive definition of hydrophobicity and a standard grid cropped 4 Å from the nearest site point.

Refine Protein-Ligand Complex.

Refinement of the LXR LBDs was performed using the Schrodinger Biologics Suite. Ligands were docked into the respective LXR crystal structures using previously described methods. The Variable Solvent Model with Generalized Born (VSGB) was chosen as the solvation model. Protein atoms were refined within 10.0 Å of the docked ligand centroid using the Hierarchical optimization sampling algorithm.

4.5 Physiochemical Properties

Reference standards were purchased from Caymen Chemical. EC50 values were reported according to the listed values on the Caymen Chemical website.

Passive Diffusion PAMPA.

Permeability assays were performed according to the manufacturer's protocol. BioAssay Systems Parallel Artificial Membrane Permeability Assay Kit (PAMPA-096). 4% lecithin in dodecane was used as the lipid bilayer. 10 mM stocks of AU403 and reference compounds were prepared in DMSO. All samples were diluted in PBS (pH=7.4) to a final concentration of 500 uM. 300 uL of PBS were added to acceptor plates (B), and 200 uL of test sample were added to donor plates (A). The assay was run on the benchtop and incubated at RT for 18 hours. Final concentrations were determined by UV-Vis.

LogP and LogD.

LogP studies were performed by making 10 mM stocks of the test compound in octanol. Standard calibrations were determined using a 2-fold serial dilution of the stock solutions and then measured on a Nanodrop UV-Vis. Working standard calibration range 5 – 0.3125 mM. 200 uL of a 5 mM test compound in octanol was combined with 400 uL of an appropriate aqueous phase. Samples were vortexed for 1 minute and allowed to equilibrate on a Belly Dancer for 2 hrs. Final concentrations were then determined by assessing the amount remaining in the octanol layer based on pre-determined sample standard calibration curves. Samples were run in triplicate, and the average value was reported. The pH of buffered aqueous phases was made to assess solubility

across a range of physiologically relevant settings. PBS and Citrate Buffer were made according to general buffer protocols for the given pH.

References

1. Hendriks S, Peetoom K, Bakker C, van der Flier WM, Papma JM, Koopmans R, Verhey FRJ, de Vugt M, Köhler S, Withall A, Parlevliet JL, Uysal-Bozkir Ö, Gibson RC, Neita SM, Nielsen TR, Salem LC, Nyberg J, Lopes MA, Dominguez JC, De Guzman MF, Egeberg A, Radford K, Broe T, Subramaniam M, Abdin E, Bruni AC, Di Lorenzo R, Smith K, Flicker L, Mol MO, Basta M, Yu D, Masika G, Petersen MS, Ruano L. Global Prevalence of Young-Onset Dementia: A Systematic Review and Meta-analysis. JAMA Neurol. 2021;78(9):1080-90. doi: 10.1001/jamaneurol.2021.2161. PubMed PMID: 34279544; PMCID: PMC8290331.
2. Alzheimer A. Über eigenartige Krankheitsfälle des späteren Alters:(On certain peculiar diseases of old age. History of Psychiatry. 1991;2(5):74-101. doi: 10.1177/0957154x9100200506.
3. Möller HJ, Graeber MB. The case described by Alois Alzheimer in 1911. European Archives of Psychiatry and Clinical Neuroscience. 1998;248(3):111-22. doi: 10.1007/s004060050027.
4. SOLOMON C. FULLER. A STUDY OF THE MILIARY PLAQUES FOUND IN BRAINS OF THE AGED. American Journal of Psychiatry. 1911;68(2):147-220-16. doi: 10.1176/ajp.68.2.147.
5. Kraeplin E. Lectures in Clinical Psychology. 3rd English ed. edited by ThomasJohnstone. New York: William Wood and Company. 1912.
6. Glenner GG, Wong CW. Alzheimer's disease: Initial report of the purification and characterization of a novel cerebrovascular amyloid protein. Biochemical and Biophysical Research Communications. 1984;120(3):885-90. doi: https://doi.org/10.1016/S0006-291X(84)80190-4.
7. Ksiezak-Reding H, Dickson DW, Davies P, Yen SH. Recognition of tau epitopes by anti-neurofilament antibodies that bind to Alzheimer neurofibrillary tangles. Proceedings of the National Academy of Sciences. 1987;84(10):3410-4. doi: doi:10.1073/pnas.84.10.3410.
8. Sunderland T, Linker G, Mirza N, Putnam KT, Friedman DL, Kimmel LH, Bergeson J, Manetti GJ, Zimmermann M, Tang B, Bartko JJ, Cohen RM. Decreased β-Amyloid1-42 and Increased Tau Levels in Cerebrospinal Fluid of Patients With Alzheimer Disease. JAMA. 2003;289(16):2094-103. doi: 10.1001/jama.289.16.2094.
9. Jonsson T, Atwal JK, Steinberg S, Snaedal J, Jonsson PV, Bjornsson S, Stefansson H, Sulem P, Gudbjartsson D, Maloney J, Hoyte K, Gustafson A, Liu Y, Lu Y, Bhangale T, Graham RR, Huttenlocher J, Bjornsdottir G, Andreassen OA, Jönsson EG, Palotie A, Behrens TW, Magnusson OT, Kong A, Thorsteinsdottir U, Watts RJ, Stefansson K. A mutation in APP protects against Alzheimer's disease and age-related cognitive decline. Nature. 2012;488(7409):96-9. doi: 10.1038/nature11283.
10. Honarnejad K, Jung CKE, Lammich S, Arzberger T, Kretzschmar H, Herms J. Involvement of presenilin holoprotein upregulation in calcium dyshomeostasis of Alzheimer's disease. Journal of Cellular and Molecular Medicine. 2013;17(2):293-302. doi: https://doi.org/10.1111/jcmm.12008.
11. Zalocusky KA, Nelson MR, Huang Y. An Alzheimer's-disease-protective APOE mutation. Nature Medicine. 2019;25(11):1648-9. doi: 10.1038/s41591-019-0634-9.
12. Chung Y, Lee H, Weiner MW, Aisen P, Petersen R, Jack CR, Jagust W, Trojanowki JQ, Toga AW, Beckett L, Green R, Saykin AJ, Morris J, Shaw LM, Khachaturian Z, Sorensen G,

Carrillo M, Kuller L, Raichle M, Paul S, Davies P, Fillit H, Hefti F, Holtzman D, Mesulam MM, Potter W, Snyder P, Montine T, Thomas RG, Donohue M, Walter S, Sather T, Jiminez G, Balasubramanian AB, Mason J, Sim I, Harvey D, Bernstein M, Fox N, Thompson P, Schuf N, DeCarli C, Borowski B, Gunter J, Senjem M, Vemuri P, Jones D, Kantarci K, Ward C, Koeppe RA, Foster N, Reiman EM, Chen K, Mathis C, Landau S, Cairns NJ, Householder E, Taylor-Reinwald L, Lee V, Korecka M, Figurski M, Crawford K, Neu S, Foroud TM, Potkin S, Shen L, Faber K, Kim S, Tha L, Frank R, Hsiao J, Kaye J, Quinn J, Silbert L, Lind B, Carter R, Dolen S, Ances B, Carroll M, Creech ML, Franklin E, Mintun MA, Schneider S, Oliver A, Schneider LS, Pawluczyk S, Beccera M, Teodoro L, Spann BM, Brewer J, Vanderswag H, Fleisher A, Marson D, Grifth R, Clark D, Geldmacher D, Brockington J, Roberson E, Love MN, Heidebrink JL, Lord JL, Mason SS, Albers CS, Knopman D, Johnson K, Grossman H, Mitsis E, Shah RC, deToledo-Morrell L, Doody RS, Villanueva-Meyer J, Chowdhury M, Rountree S, Dang M, Duara R, Varon D, Greig MT, Roberts P, Stern Y, Honig LS, Bell KL, Albert M, Onyike C, D'Agostino D, Kielb S, Galvin JE, Cerbone B, Michel CA, Pogorelec DM, Rusinek H, de Leon MJ, Glodzik L, De Santi S, Womack K, Mathews D, Quiceno M, Doraiswamy PM, Petrella JR, Borges-Neto S, Wong TZ, Coleman E, Levey AI, Lah JJ, Cella JS, Burns JM, Swerdlow RH, Brooks WM, Arnold SE, Karlawish JH, Wolk D, Clark CM, Apostolova L, Tingus K, Woo E, Silverman DHS, Lu PH, Bartzokis G, Smith CD, Jicha G, Hardy P, Sinha P, Oates E, Conrad G, Graf-Radford NR, Parftt F, Kendall T, Johnson H, Lopez OL, Oakley M, Simpson DM, Farlow MR, Hake AM, Matthews BR, Brosch JR, Herring S, Hunt C, Porsteinsson AP, Goldstein BS, Martin K, Makino KM, Ismail MS, Brand C, Mulnard RA, Thai G, Mc-Adams-Ortiz C, van Dyck CH, Carson RE, MacAvoy MG, Varma P, Chertkow H, Bergman H, Hosein C, Black S, Stefanovic B, Caldwell C, Hsiung G-YR, Feldman H, Mudge B, Assaly M, Finger E, Pasternack S, Rachisky I, Trost D, Kertesz A, Bernick C, Munic D, Lipowski K, Weintraub M, Bonakdarpour B, Kerwin D, Wu C-K, Johnson N, Sadowsky C, Villena T, Turner RS, Johnson K, Reynolds B, Sperling RA, Johnson KA, Marshall G, Yesavage J, Taylor JL, Lane B, Rosen A, Tinklenberg J, Sabbagh MN, Belden CM, Jacobson SA, Sirrel SA, Kowall N, Killiany R, Budson AE, Norbash A, Johnson PL, Obisesan TO, Wolday S, Allard J, Lerner A, Ogrocki P, Tatsuoka C, Fatica P, Fletcher E, Maillard P, Olichney J, Carmichael O, Kittur S, Borrie M, Lee TY, Bartha R, Johnson S, Asthana S, Carlsson CM, Preda A, Nguyen D, Tariot P, Burke A, Trncic N, Fleisher A, Reeder S, Bates V, Capote H, Rainka M, Scharre DW, Kataki M, Adeli A, Zimmerman EA, Celmins D, Brown AD, Pearlson GD, Blank K, Anderson K, Flashman LA, Seltzer M, Hynes ML, Santulli RB, Sink KM, Gordineer L, Williamson JD, Garg P, Watkins F, Ott BR, Querfurth H, Tremont G, Salloway S, Malloy P, Correia S, Rosen HJ, Miller BL, Perry D, Mintzer J, Spicer K, Bachman D, Finger E, Pasternak S, Rachinsky I, Rogers J, Drost D, Pomara N, Hernando R, the Alzheimer's Disease Neuroimaging I. Correlation between Alzheimer's disease and type 2 diabetes using non-negative matrix factorization. Scientific Reports. 2021;11(1):15265. doi: 10.1038/s41598-021-94048-0.

13. Williams AC, Ramsden DB. Nicotinamide homeostasis: A xenobiotic pathway that is key to development and degenerative diseases. Medical Hypotheses. 2005;65(2):353-62. doi: https://doi.org/10.1016/j.mehy.2005.01.042.

14. Nagu P, Parashar A, Behl T, Mehta V. Gut Microbiota Composition and Epigenetic Molecular Changes Connected to the Pathogenesis of Alzheimer's Disease. Journal of Molecular Neuroscience. 2021;71(7):1436-55. doi: 10.1007/s12031-021-01829-3.

15. Armstrong MJ, Jin Y, Vattathil SM, Huang Y, Schroeder JP, Bennet DA, Qin ZS, Wingo TS, Jin P. Role of TET1-mediated epigenetic modulation in Alzheimer's disease. Neurobiology of Disease. 2023;185:106257. doi: https://doi.org/10.1016/j.nbd.2023.106257.
16. Lin-Lee YC, Kao FT, Cheung P, Chan L. Apolipoprotein E gene mapping and expression: localization of the structural gene to human chromosome 19 and expression of ApoE mRNA in lipoprotein-and non-lipoprotein-producing tissues. Biochemistry. 1985;24(14):3751-6.
17. Tsukamoto K, Smith P, Glick JM, Rader DJ. Liver-directed gene transfer and prolonged expression of three major human ApoE isoforms in ApoE-deficient mice. The Journal of Clinical Investigation. 1997;100(1):107-14. doi: 10.1172/JCI119501.
18. Zhang Y, Vasudevan S, Sojitrawala R, Zhao W, Cui C, Xu C, Fan D, Newhouse Y, Balestra R, Jerome WG, Weisgraber K, Li Q, Wang J. A Monomeric, Biologically Active, Full-Length Human Apolipoprotein E. Biochemistry. 2007;46(37):10722-32. doi: 10.1021/bi700672v.
19. Vitek MP, Brown CM, Colton CA. APOE genotype-specific differences in the innate immune response. Neurobiology of Aging. 2009;30(9):1350-60. doi: https://doi.org/10.1016/j.neurobiolaging.2007.11.014.
20. Laskowitz DT, Lee DM, Schmechel D, Staats HF. Altered immune responses in apolipoprotein E-deficient mice. Journal of Lipid Research. 2000;41(4):613-20. doi: https://doi.org/10.1016/S0022-2275(20)32409-3.
21. Utermann G, Kindermann I, Kaffarnik H, Steinmetz A. Apolipoprotein E phenotypes and hyperlipidemia. Human Genetics. 1984;65(3):232-6. doi: 10.1007/BF00286508.
22. Kim YS, Paeng JR, Woo JT, Kim SW, Yang IM, Kim JW, Kim KW, Choi YK. Apolipoprotein E genotypes of normal and hyperlipidemic subjects. jkms. 2009;8(4):262-6. doi: 10.3346/jkms.1993.8.4.262.
23. Wingo TS, Lah JJ, Levey AI, Cutler DJ. Autosomal recessive causes likely in early-onset Alzheimer disease. Arch Neurol. 2012;69(1):59-64. Epub 20110912. doi: 10.1001/archneurol.2011.221. PubMed PMID: 21911656; PMCID: PMC3332307.
24. Ghebranious N, Ivacic L, Mallum J, Dokken C. Detection of ApoE E2, E3 and E4 alleles using MALDI-TOF mass spectrometry and the homogeneous mass-extend technology. Nucleic Acids Res. 2005;33(17):e149. Epub 20051004. doi: 10.1093/nar/gni155. PubMed PMID: 16204452; PMCID: PMC1243648.
25. Riddell DR, Zhou H, Atchison K, Warwick HK, Atkinson PJ, Jefferson J, Xu L, Aschmies S, Kirksey Y, Hu Y, Wagner E, Parratt A, Xu J, Li Z, Zaleska MM, Jacobsen JS, Pangalos MN, Reinhart PH. Impact of apolipoprotein E (ApoE) polymorphism on brain ApoE levels. J Neurosci. 2008;28(45):11445-53. doi: 10.1523/jneurosci.1972-08.2008. PubMed PMID: 18987181; PMCID: PMC6671315.
26. Skottova N, Savonen R, Lookene A, Hultin M, Olivecrona G. Lipoprotein lipase enhances removal of chylomicrons and chylomicron remnants by the perfused rat liver. Journal of Lipid Research. 1995;36(6):1334-44. doi: https://doi.org/10.1016/S0022-2275(20)41141-1.
27. Huebbe P, Rimbach G. Evolution of human apolipoprotein E (APOE) isoforms: Gene structure, protein function and interaction with dietary factors. Ageing Research Reviews. 2017;37:146-61. doi: https://doi.org/10.1016/j.arr.2017.06.002.
28. Brookhouser N, Raman S, Frisch C, Srinivasan G, Brafman DA. APOE2 mitigates disease-related phenotypes in an isogenic hiPSC-based model of Alzheimer’s disease. Molecular Psychiatry. 2021;26(10):5715-32. doi: 10.1038/s41380-021-01076-3.

29. Halliday MR, Pomara N, Sagare AP, Mack WJ, Frangione B, Zlokovic BV. Relationship between cyclophilin a levels and matrix metalloproteinase 9 activity in cerebrospinal fluid of cognitively normal apolipoprotein e4 carriers and blood-brain barrier breakdown. JAMA Neurol. 2013;70(9):1198-200. doi: 10.1001/jamaneurol.2013.3841. PubMed PMID: 24030206; PMCID: PMC4047029.
30. Bekris LM, Galloway NM, Montine TJ, Schellenberg GD, Yu CE. APOE mRNA and protein expression in postmortem brain are modulated by an extended haplotype structure. Am J Med Genet B Neuropsychiatr Genet. 2010;153b(2):409-17. doi: 10.1002/ajmg.b.30993. PubMed PMID: 19554612; PMCID: PMC2829359.
31. Farmer BC, Kluemper J, Johnson LA. Apolipoprotein E4 Alters Astrocyte Fatty Acid Metabolism and Lipid Droplet Formation. Cells. 2019;8(2). Epub 20190220. doi: 10.3390/cells8020182. PubMed PMID: 30791549; PMCID: PMC6406677.
32. Abbott NJ, Rönnbäck L, Hansson E. Astrocyte–endothelial interactions at the blood–brain barrier. Nature Reviews Neuroscience. 2006;7(1):41-53. doi: 10.1038/nrn1824.
33. Jairani PS, Aswathy PM, Krishnan D, Menon RN, Verghese J, Mathuranath PS, Gopala S. Apolipoprotein E Polymorphism and Oxidative Stress in Peripheral Blood-Derived Macrophage-Mediated Amyloid-Beta Phagocytosis in Alzheimer's Disease Patients. Cellular and Molecular Neurobiology. 2019;39(3):355-69. doi: 10.1007/s10571-019-00651-1.
34. Abildayeva K, Jansen PJ, Hirsch-Reinshagen V, Bloks VW, Bakker AHF, Ramaekers FCS, de Vente J, Groen AK, Wellington CL, Kuipers F, Mulder M. 24(S)-Hydroxycholesterol Participates in a Liver X Receptor-controlled Pathway in Astrocytes That Regulates Apolipoprotein E-mediated Cholesterol Efflux*. Journal of Biological Chemistry. 2006;281(18):12799-808. doi: https://doi.org/10.1074/jbc.M601019200.
35. Nelson TJ, Sen A. Apolipoprotein E particle size is increased in Alzheimer's disease. Alzheimers Dement (Amst). 2019;11:10-8. Epub 20181113. doi: 10.1016/j.dadm.2018.10.005. PubMed PMID: 30581971; PMCID: PMC6293020.
36. Castellano JM, Kim J, Stewart FR, Jiang H, DeMattos RB, Patterson BW, Fagan AM, Morris JC, Mawuenyega KG, Cruchaga C, Goate AM, Bales KR, Paul SM, Bateman RJ, Holtzman DM. Human apoE Isoforms Differentially Regulate Brain Amyloid-β Peptide Clearance. Science Translational Medicine. 2011;3(89):89ra57-89ra57. doi: doi:10.1126/scitranslmed.3002156.
37. Pires M, Rego AC. Apoe4 and Alzheimer's Disease Pathogenesis-Mitochondrial Deregulation and Targeted Therapeutic Strategies. Int J Mol Sci. 2023;24(1). Epub 20230101. doi: 10.3390/ijms24010778. PubMed PMID: 36614219; PMCID: PMC9821307.
38. A Unified Nomenclature System for the Nuclear Receptor Superfamily. Cell. 1999;97(2):161-3. doi: https://doi.org/10.1016/S0092-8674(00)80726-6.
39. Styles JA, Kelly M, Pritchard NR, Ekcombe CR. A species comparison of acute hyperplasia induced by the peroxisome proliferator methylclofenapate: involvement of the binucleated hepatocyte. Carcinogenesis. 1988;9(9):1647-55. doi: 10.1093/carcin/9.9.1647.
40. Göttlicher M, Widmark E, Li Q, Gustafsson JA. Fatty acids activate a chimera of the clofibric acid-activated receptor and the glucocorticoid receptor. Proc Natl Acad Sci U S A. 1992;89(10):4653-7. doi: 10.1073/pnas.89.10.4653. PubMed PMID: 1316614; PMCID: PMC49141.
41. Issemann I, Green S. Activation of a member of the steroid hormone receptor superfamily by peroxisome proliferators. Nature. 1990;347(6294):645-50. doi: 10.1038/347645a0.

42. Krey G, Braissant O, L'Horset F, Kalkhoven E, Perroud M, Parker MG, Wahli W. Fatty Acids, Eicosanoids, and Hypolipidemic Agents Identified as Ligands of Peroxisome Proliferator-Activated Receptors by Coactivator-Dependent Receptor Ligand Assay. Molecular Endocrinology. 1997;11(6):779-91. doi: 10.1210/mend.11.6.0007.
43. Murakami K, Tobe K, Ide T, Mochizuki T, Ohashi M, Akanuma Y, Yazaki Y, Kadowaki T. A novel insulin sensitizer acts as a coligand for peroxisome proliferator-activated receptor-alpha (PPAR-alpha) and PPAR-gamma: effect of PPAR-alpha activation on abnormal lipid metabolism in liver of Zucker fatty rats. Diabetes. 1998;47(12):1841-7. doi: 10.2337/diabetes.47.12.1841.
44. KEHRER JP, BISWAL SS, LA E, THUILLIER P, DATTA K, FISCHER SM, VANDEN HEUVEL JP. Inhibition of peroxisome-proliferator-activated receptor (PPAR)α by MK886. Biochemical Journal. 2001;356(3):899-906. doi: 10.1042/bj3560899.
45. Lemberger T, Staels B, Saladin R, Desvergne B, Auwerx J, Wahli W. Regulation of the peroxisome proliferator-activated receptor alpha gene by glucocorticoids. Journal of Biological Chemistry. 1994;269(40):24527-30. doi: https://doi.org/10.1016/S0021-9258(17)31420-5.
46. Vidal-Puig A, Jimenez-Liñan M, Lowell BB, Hamann A, Hu E, Spiegelman B, Flier JS, Moller DE. Regulation of PPAR gamma gene expression by nutrition and obesity in rodents. The Journal of Clinical Investigation. 1996;97(11):2553-61. doi: 10.1172/JCI118703.
47. Chawla A, Schwarz EJ, Dimaculangan DD, Lazar MA. Peroxisome proliferator-activated receptor (PPAR) gamma: adipose-predominant expression and induction early in adipocyte differentiation. Endocrinology. 1994;135(2):798-800. doi: 10.1210/en.135.2.798.
48. Higashiyama H, Billin AN, Okamoto Y, Kinoshita M, Asano S. Expression profiling of Peroxisome proliferator-activated receptor-delta (PPAR-delta) in mouse tissues using tissue microarray. Histochemistry and Cell Biology. 2007;127(5):485-94. doi: 10.1007/s00418-007-0279-5.
49. Skogsberg J, Kannisto K, Roshani L, Gagne E, Hamsten A, Larsson C, Ehrenborg E. Characterization of the human peroxisome proliferator activated receptor delta gene and its expression. Int J Mol Med. 2000;6(1):73-154. doi: 10.3892/ijmm.6.1.73.
50. Risérus U, Sprecher D, Johnson T, Olson E, Hirschberg S, Liu A, Fang Z, Hegde P, Richards D, Sarov-Blat L, Strum JC, Basu S, Cheeseman J, Fielding BA, Humphreys SM, Danoff T, Moore NR, Murgatroyd P, O'Rahilly S, Sutton P, Willson T, Hassall D, Frayn KN, Karpe F. Activation of Peroxisome Proliferator–Activated Receptor (PPAR)δ Promotes Reversal of Multiple Metabolic Abnormalities, Reduces Oxidative Stress, and Increases Fatty Acid Oxidation in Moderately Obese Men. Diabetes. 2008;57(2):332-9. doi: 10.2337/db07-1318.
51. Warden A, Truitt J, Merriman M, Ponomareva O, Jameson K, Ferguson LB, Mayfield RD, Harris RA. Localization of PPAR isotypes in the adult mouse and human brain. Scientific Reports. 2016;6(1):27618. doi: 10.1038/srep27618.
52. Neurological Recovery-Promoting, Anti-Inflammatory, and Anti-Oxidative Effects Afforded by Fenofibrate, a PPAR Alpha Agonist, in Traumatic Brain Injury. Journal of Neurotrauma. 2007;24(7):1119-31. doi: 10.1089/neu.2006.0216. PubMed PMID: 17610352.
53. Ramanan S, Kooshki M, Zhao W, Hsu F-C, Riddle DR, Robbins ME. The PPARα Agonist Fenofibrate Preserves Hippocampal Neurogenesis and Inhibits Microglial Activation After Whole-Brain Irradiation. International Journal of Radiation Oncology*Biology*Physics. 2009;75(3):870-7. doi: https://doi.org/10.1016/j.ijrobp.2009.06.059.
54. More VR, Campos CR, Evans RA, Oliver KD, Chan GNY, Miller DS, Cannon RE. PPAR-α, a lipid-sensing transcription factor, regulates blood–brain barrier efflux transporter

expression. Journal of Cerebral Blood Flow & Metabolism. 2016;37(4):1199-212. doi: 10.1177/0271678X16650216.
55. Steinke I, Govindarajulu M, Pinky PD, Bloemer J, Yoo S, Ward T, Schaedig T, Young T, Wibowo FS, Suppiramaniam V. Selective PPAR-Delta/PPAR-Gamma Activation Improves Cognition in a Model of Alzheimer's Disease. Cells. 2023;12(8):1116.
56. Reich D, Gallucci G, Tong M, de la Monte SM. Therapeutic Advantages of Dual Targeting of PPAR-δ and PPAR-γ in an Experimental Model of Sporadic Alzheimer's Disease. J Parkinsons Dis Alzheimers Dis. 2018;5(1). Epub 20180521. doi: 10.13188/2376-922x.1000025. PubMed PMID: 30705969; PMCID: PMC6350901.
57. Song J, Choi S-M, Kim BC. Adiponectin Regulates the Polarization and Function of Microglia via PPAR-γ Signaling Under Amyloid β Toxicity. Frontiers in Cellular Neuroscience. 2017;11. doi: 10.3389/fncel.2017.00064.
58. Mohamed EA, Ahmed HI, Zaky HS, Badr AM. Sesame oil mitigates memory impairment, oxidative stress, and neurodegeneration in a rat model of Alzheimer's disease. A pivotal role of NF-κB/p38MAPK/BDNF/PPAR-γ pathways. Journal of Ethnopharmacology. 2021;267:113468. doi: https://doi.org/10.1016/j.jep.2020.113468.
59. Benedetti E, D'Angelo B, Cristiano L, Di Giacomo E, Fanelli F, Moreno S, Cecconi F, Fidoamore A, Antonosante A, Falcone R, Ippoliti R, Giordano A, Cimini A. Involvement of peroxisome proliferator-activated receptor β/δ (PPAR β/δ) in BDNF signaling during aging and in Alzheimer disease: Possible role of 4-hydroxynonenal (4-HNE). Cell Cycle. 2014;13(8):1335-44. doi: 10.4161/cc.28295.
60. Chamberlain S, Gabriel H, Strittmatter W, Didsbury J. An Exploratory Phase IIa Study of the PPAR delta/gamma Agonist T3D-959 Assessing Metabolic and Cognitive Function in Subjects with Mild to Moderate Alzheimer's Disease. Journal of Alzheimer's Disease. 2020;73:1085-103. doi: 10.3233/JAD-190864.
61. Apfel R, Benbrook D, Lernhardt E, Ortiz MA, Salbert G, Pfahl M. A novel orphan receptor specific for a subset of thyroid hormone-responsive elements and its interaction with the retinoid/thyroid hormone receptor subfamily. Mol Cell Biol. 1994;14(10):7025-35. doi: 10.1128/mcb.14.10.7025-7035.1994. PubMed PMID: 7935418; PMCID: PMC359232.
62. Willy PJ, Umesono K, Ong ES, Evans RM, Heyman RA, Mangelsdorf DJ. LXR, a nuclear receptor that defines a distinct retinoid response pathway. Genes Dev. 1995;9(9):1033-45. doi: 10.1101/gad.9.9.1033. PubMed PMID: 7744246.
63. Teboul M, Enmark E, Li Q, Wikström AC, Pelto-Huikko M, Gustafsson JA. OR-1, a member of the nuclear receptor superfamily that interacts with the 9-cis-retinoic acid receptor. Proc Natl Acad Sci U S A. 1995;92(6):2096-100. doi: 10.1073/pnas.92.6.2096. PubMed PMID: 7892230; PMCID: PMC42430.
64. Wong J, Quinn CM, Brown AJ. Synthesis of the oxysterol, 24(S), 25-epoxycholesterol, parallels cholesterol production and may protect against cellular accumulation of newly-synthesized cholesterol. Lipids in Health and Disease. 2007;6(1):10. doi: 10.1186/1476-511X-6-10.
65. Nelson JA, Steckbeck SR, Spencer TA. Biosynthesis of 24,25-epoxycholesterol from squalene 2,3;22,23-dioxide. Journal of Biological Chemistry. 1981;256(3):1067-8. doi: https://doi.org/10.1016/S0021-9258(19)69921-7.
66. Forman BM, Ruan B, Chen J, Schroepfer GJ, Jr., Evans RM. The orphan nuclear receptor LXRalpha is positively and negatively regulated by distinct products of mevalonate metabolism.

Proc Natl Acad Sci U S A. 1997;94(20):10588-93. doi: 10.1073/pnas.94.20.10588. PubMed PMID: 9380679; PMCID: PMC23411.
67. Janowski BA, Grogan MJ, Jones SA, Wisely GB, Kliewer SA, Corey EJ, Mangelsdorf DJ. Structural requirements of ligands for the oxysterol liver X receptors LXRα and LXRβ. Proceedings of the National Academy of Sciences. 1999;96(1):266-71.
68. Joseph SB, McKilligin E, Pei L, Watson MA, Collins AR, Laffitte BA, Chen M, Noh G, Goodman J, Hagger GN. Synthetic LXR ligand inhibits the development of atherosclerosis in mice. Proceedings of the National Academy of Sciences. 2002;99(11):7604-9.
69. Peet DJ, Turley SD, Ma W, Janowski BA, Lobaccaro J-MA, Hammer RE, Mangelsdorf DJ. Cholesterol and bile acid metabolism are impaired in mice lacking the nuclear oxysterol receptor LXRα. Cell. 1998;93(5):693-704.
70. Quinet EM, Savio DA, Halpern AR, Chen L, Schuster GU, Gustafsson J-Å, Basso MD, Nambi P. Liver X receptor (LXR)-β regulation in LXRα-deficient mice: implications for therapeutic targeting. Molecular pharmacology. 2006;70(4):1340-9.
71. Bretillon L, Diczfalusy U, Björkhem I, Maire MA, Martine L, Joffre C, Acar N, Bron A, Creuzot-Garcher C. Cholesterol-24S-hydroxylase (CYP46A1) Is Specifically Expressed in Neurons of the Neural Retina. Current Eye Research. 2007;32(4):361-6. doi: 10.1080/02713680701231857.
72. Jahn T, Clark C, Kerksiek A, Lewczuk P, Lütjohann D, Popp J. Cholesterol metabolites and plant sterols in cerebrospinal fluid are associated with Alzheimer's cerebral pathology and clinical disease progression. The Journal of Steroid Biochemistry and Molecular Biology. 2021;205:105785. doi: https://doi.org/10.1016/j.jsbmb.2020.105785.
73. Wang Y, An Y, Zhang D, Yu H, Zhang X, Wang Y, Tao L, Xiao R. 27-Hydroxycholesterol Alters Synaptic Structural and Functional Plasticity in Hippocampal Neuronal Cultures. J Neuropathol Exp Neurol. 2019;78(3):238-47. doi: 10.1093/jnen/nlz002. PubMed PMID: 30753597; PMCID: PMC7967841.
74. Food U, Drug Administration J. Drugs@ FDA glossary of terms. Silver Spring, MD: US Food and Drug Administration. 2017.
75. Office. CB. The Budget and Economic Outlook: 2021 to 2031. 2021. Available from: https://www.cbo.gov/publication/57126#_idTextAnchor020.
76. Wouters OJ, McKee M, Luyten J. Estimated Research and Development Investment Needed to Bring a New Medicine to Market, 2009-2018. Jama. 2020;323(9):844-53. doi: 10.1001/jama.2020.1166. PubMed PMID: 32125404; PMCID: PMC7054832.
77. Yu W, MacKerell AD, Jr. Computer-Aided Drug Design Methods. Methods Mol Biol. 2017;1520:85-106. doi: 10.1007/978-1-4939-6634-9_5. PubMed PMID: 27873247; PMCID: PMC5248982.
78. Gathiaka S, Nanayakkara G, Boncher T, Acevedo O, Wyble J, Patel S, Patel A, Shane ME, Bonkowski B, Wieczorek J, Rong Y, Huggins K, Smith F, Amin RH. Design, development and evaluation of novel dual PPARδ/PPARγ agonists. Bioorg Med Chem Lett. 2013;23(3):873-9. Epub 20121203. doi: 10.1016/j.bmcl.2012.11.060. PubMed PMID: 23273519.
79. Steinke I, Govindarajulu M, Pinky PD, Bloemer J, Yoo S, Ward T, Schaedig T, Young T, Wibowo FS, Suppiramaniam V, Amin RH. Selective PPAR-Delta/PPAR-Gamma Activation Improves Cognition in a Model of Alzheimer's Disease. Cells. 2023;12(8). Epub 20230408. doi: 10.3390/cells12081116. PubMed PMID: 37190025; PMCID: PMC10136457.